# Electronic transport properties of vertical and lateral graphene-based heterostructures

THÈSE N$^{O}$ 7419 (2016)

PRÉSENTÉE LE 20 DÉCEMBRE 2016
À LA FACULTÉ DES SCIENCES DE BASE
LABORATOIRE DE SCIENCE À L'ÉCHELLE NANOMÉTRIQUE
PROGRAMME DOCTORAL EN SCIENCE ET GÉNIE DES MATÉRIAUX

ÉCOLE POLYTECHNIQUE FÉDÉRALE DE LAUSANNE

POUR L'OBTENTION DU GRADE DE DOCTEUR ÈS SCIENCES

PAR

Roberto URCUYO SOLORZANO

acceptée sur proposition du jury:

Prof. H. Frauenrath, président du jury
Prof. K. Kern, directeur de thèse
Prof. A. Mews, rapporteur
Prof. C. Gomez-Navarro, rapporteuse
Dr A. Fontcuberta i Morral, rapporteuse

ÉCOLE POLYTECHNIQUE
FÉDÉRALE DE LAUSANNE

Suisse
2016

# Acknowledgements

Firstly, I would like to dedicate this thesis to my wife, Milena Jiménez Gutiérrez and acknowledge my parents, Libia Solórzano Guillén and Mario Urcuyo Acuña, and my entire family for the support.

I am also very grateful to my thesis advisor Prof. Klaus Kern who gave me the opportunity to work at the Max Planck Institute for Solid State Research in Stuttgart and who has supported me throughout my PhD studies. I am especially thankful to my group leader Marko Burghard for his scientific support throughout the years and, in general, for good times we have shared.

I would also like to thank the people of the quantum materials group for giving me their excellent scientific input and support over these years.

Finally, I thank the University of Costa Rica, CELEQ and Escuela de Química for economic support; I am especially thankful to prof. Dr. Carlos Léon Rojas, prof. Dr. Cristian Campos Fernández and prof. Dr. Mavis Montero Villalobos for their advice.

# Abstract

Owing to its unique electrical and mechanical properties, the 2D quantum material graphene has attracted enormous interest for both, fundamental research and technological applications. However, graphene has some drawbacks, like the absence of an electronic band gap which leads to only small gate switching ratios, and its fast carrier recombination that limits its use in optoelectronics. In order to overcome these issues, the aim of this thesis was to tune the properties of graphene by two different modification approaches. The first approach involved chemical functionalization to create lateral graphene heterostructures, whereas the second approach was directed toward vertical heterostructures that combine graphene with another 2D material or an ultrathin metal layer.

For the lateral heterostructure fabrication, two novel chemical functionalization methods were investigated. The first method relied upon hyperthermal molecular ion collisions with 4,4´-azobis(pyridine). This one-step protocol enabled the covalent functionalization of CVD graphene with a functionalization degree of up to 3%, as demonstrated by Raman spectroscopy in combination with XPS. AFM studies revealed that even the heavily functionalized sheets retain their topographic integrity. Thus obtained stripe-like patterns of covalently graphene within extended graphene sheets enabled enhanced on/off ratios upon gate switching. In the second functionalization scheme, the strong oxidizer $OsO_4$ was used to selectively introduce hydroxyl groups to graphene. Best results were obtained when the reaction was performed under UV light activation, which yielded graphene of high covalent functionalization degree, as concluded from its optical transparency and gate-induced on/off switching ratios of up to 500 at low temperature. Temperature dependent electrical measurements revealed 2D hopping as the dominant transport mechanism in the functionalized sheets.

As the first type of vertical heterostructure, graphene-$TiO_x$-Ti diodes were fabricated and their electrical properties in the dark and under visible light illumination studied in detail. In contrast to conventional metal-insulator-metal (MIM) diodes, the performance of the graphene-based diodes was found to increase with decreasing thickness of the oxide insulator. Bias-induced modulation of the work function of graphene was identified as the key to the operation mechanism of the graphene diodes, enabling them to reach a very high asymmetry and nonlinearity of up to 9000 and 8, respectively. Combined with their ability to maintain a large on-current of 0.1 $A/cm^2$ at 1 V, the diodes compete well with state-of-the-art MIM diodes. Furthermore, the graphene-$TiO_x$-Ti diodes could be operated as photovoltaic cell, with a maximum open-circuit voltage of 0.3 V and a short-circuit photocurrent of 14 nA under global illumination by a green light.

This finding constitutes the first proof-of-principle of hot carrier extraction from graphene, based on the photovoltaic effect.

The second type of vertical heterostructures was based on black phosphorus, a 2D material exhibiting p-type doping character. As a first step, thin black phosphorous sheets were combined with n-GaAs into novel pn heterojunction devices. They displayed pronounced rectification behavior that, in the low bias regime, approaches that of ideal diodes. Moreover, when operated as photodiodes they reached external quantum efficiencies (EQE) of up to 10% under zero bias, and above 30% under higher reverse bias. On this basis, the black phosphorous was then combined with graphene into a p+/p heterojunction. Thus obtained devices achieved a maximum internal quantum efficiency (IQE) and responsivity of 13% and 10.7 mA/W, respectively. This IQE is the highest thus far reported for diodes comprising black phosphorous and another 2D material. Moreover, with the aid of a top gate it was possible to modulate both, the photo-conversion efficiency and photocurrent generation mechanism of the black phosphorous-graphene diodes. Together with the possibility to tune the photocurrent response by the thickness of the black phosphorous, these diodes emerge as promising photodetectors.

In summary, the findings of this thesis work testify that chemical functionalization and the formation of van der Waals heterostructures are viable routes to tailor the electronic properties of graphene, and thereby to expand the application range of graphene-based electronic or optoelectronic devices.

Keywords: Graphene, Electrospray Ionization, Black Phosphorus, 2D materials, Photovoltaic Cells, Field Effect Transistors.

# Zusammenfassung

Graphene hat aufgrund seiner einzigartigen elektrischen und mechanischen Eigenschaften enormes Interesse geweckt sowohl für die Grundlagenforschung als auch für praktische Anwendungen. Aber auch Graphen besitzt Nachteile, zum Beispiel die Abwesenheit einer elektronischen Bandlücke, wodurch die elektrische Leitfähigkeit des Graphens nur schwach schaltbar ist, sowie die sehr schnelle Ladungsträgerrekombination, welche seine Anwendung in der (Opto)elektronik einschränkt. Zur Überwindung dieser Einschränkung setzte sich die vorliegende Arbeit zum Ziel, die Eigenschaften von Graphen mittles zweier unterschiedlicher Modifikationsstrategien kontrolliert einzustellen. Der erste Ansatz beinhaltet chemische Funktionalisierung zur Gewinnung lateraler Graphen-basierter Heterostrukturen, während der zweite Ansatz die Herstellung von vertikalen Heterostrukturen umfasst, in welchen Graphen mit einem anderen 2D Material oder einer ultradünnen Metallschicht kombiniert ist.

Für die Herstellung der lateralen Heterostrukturen wurde zwei neuartige chemische Funktionalisierungsmethoden entwickelt. Die erste Methode nutzte die Kollision hyperthermaler Ionen aus dem Molekül 4,4‘-Azobis(pyridin). Sie gestattete die kovalente Funktionalisierung von CVD Graphen in einem Schritt mit einem hohen Funktionalisierungsgrad von bis zu 3%, wie mittels Raman Spektroskopie und Photoelektronenspektroskopie nachgewiesen werden konnte. Rasterkraftmikroskopie Untersuchungen ergaben, dass selbst das am stärksten funktionalisierte Graphen seine strukturelle Integrität bewahrte. Auf diese Weise erzeugte Streifenmuster von kovalent funktionalisiertem Graphen innerhalb eines Graphenblatts zeigten eine verstärkte elektrische Schaltbarkeit unter Gate-Kontrolle. Die zweite Funktionalisierungsmethode verwendete das starke Oxidationsmittel $OsO_4$ verwendet, um das Graphen selektiv mit Hydroxylgruppen auszustatten. Beste Ergebnisse wurden erzielt, wenn die Reaktion unter Aktivierung mit UV-Licht erfolgte. Die optische Transparenz und die Gate-gesteuerte elektrische Schaltbarkeit mit einem Ein/Aus-Verhältnis von bis zu 500 belegen einen hohen Funktionalisierungsgrad. Aus temperaturabhängigen elektrischen Messungen konnte geschlossen werden, dass der Ladungstransport in den funktionalisierten Monolagen bevorzugt über einen zweidimensionalen Hüpfmechanismus erfolgt.

Als erste Art von vertikalen Heterostrukturen wurden Graphen-$TiO_x$-Ti Dioden hergestellt, deren elektrische Eigenschaften im Dunkeln und unter Beleuchtung mit sichtbarem Licht im Detail studiert wurden. Im Gegensatz zu konventionellen Metall-Isolator-Metall (MIM) Dioden, stieg die Leistungsfähigkeit der Graphen-basierten Dioden mit Verringerung der Dicke der Oxidschicht. Der Operationsmechanimus der Graphendioden konnte auf die Modulierung der Austrittsarbeit des Graphens durch die angelegte Biasspannung zurückgeführt werden. Somit erreichen die Bauelemente eine sehr große Asymmetrie von bis zu 9000, sowie eine sehr hohe Nichtlinearität von 8. Kombiniert mit der Tatsache, dass sie einen sehr hohen Ein-Strom von 0,1 A/cm$^2$ bei 1 V erreichen, sind die Dioden konkurrenzfähig zu aktuellen MIM Dioden. Darüber hinaus konnten die Graphen-$TiO_x$-Ti Dioden als photovoltaische Bauelemente betrieben werden, die eine Leerlaufspannung von 0,3 V und einen Kurzschlussstrom von 14 nA unter globaler Beleuchtung erreichen. Diese Beobachtung liefert den ersten Beleg für die Extraktion heisser Ladungsträger aus Graphen auf Basis des photovoltaischen Effekts.

Die zweite Art von vertikalen Heterostrukturen basierte auf schwarzem Phosphor, ein 2D Material das p-dotiert ist. Als erster Schritt wurden dünne Schichten aus schwarzem Phosphor mit n-GaAs zu einer neuartigen pn Heterostruktur vereint Diese Bauelemente zeigten eine ausgeprägte Gleichrichtung,  welche für kleine Spannnungen einem idealen Diodenverhalten nahe kommt. Als Photodioden betrieben erreichten sie zudem eine externe Quanteneffizienz von bis zu 10% ohne Biasspannung, und mehr als 30% unter größerer Sperrspannung. Darauf aufbauend wurde der schwarze Phosphor mit Graphen zu einer p/p+ Heterostruktur kombiniert. Die erhaltenen Bauelemente erreichten eine maximale interne Quanteneffizienz von 13% sowie eine maximale Responsivität von 10,7 mA/W. Diese Effizienz ist die höchste, die bisher für Dioden bestehend aus schwarzem Phosphor und einem anderen 2D Material dokumentiert wurde. Zudem gelang es mithilfe eines Topgates sowohl die Effizienz der photoinduzierten Ladungstrennung als auch den zugrundeliegenden Mechanismus der Photostromerzeugung der schwarzer Phosphor-Graphen-Dioden zu beeinflussen. Durch die zusätzliche Möglichkeit, den Photostrom durch die Dicke der schwarzen Phosphor Schicht zu kontrollieren, sind die Dioden viel versprechend als neuartige Photodetektoren.

Die Ergebnisser der vorliegenden Arbeit belegen eindrücklich, dass die chemische Funktionalisierung von Graphen und der Aufbau von van der Waals Heterostrukturen es gestatten, die elektronischen Eigenschaften von Graphen einstellen zu können, und somit den Anwendungsbereich von Graphen-basierten elektrischen oder optolelektronischen Bauelementen zu erweitern.

Stichworte: Graphen, Elektrospray-Ionisation, schwarzer Phosphor, 2D-Materialien, Solarzellen, Feldeffekttransistoren

# Contents

# List of Acronyms

**2D materials** Two dimensional materials

**AFM** Atomic force microscopy

**AZP** 4,4´-azobis(pyridine)

**BP** Black phosphorous

**CVD** Chemical vapor deposition

**EQE** External quantum efficiency

**ESI** Electrospray ionization

**ES-IBD** Electrospray ion beam deposition

**F4-TCNQ** 2,3,5,6-Tetrafluoro-tetracyanoquinodimethane

**FET** Field effect transistor

**FF** Fill factor

**GrIM** Graphene insulator metal

**GLH** Graphene lateral heterostructures

**GNR´s** Graphene nanoribbons

**GO** Graphene oxide

**GVH** Graphene vertical heterostructures

**hBN** Hexagonal boron nitride

**IQE** Internal quantum efficiency

**Isc** Short circuit current

**MLG** Multi-layer graphene

**MIM** Metal insulator metal

**NEP** n-ethyl-pyrrolidone

**PMMA** Polymethyl methacrylate

**SET** Single electron transistor

**SLG** Single-layer graphene

**SPCM** Scanning photocurrent microscopy

**TMDC** Transition metal dichalcogenides

**TOF-MS** Time of-flight mass spectrometry

**UV** Ultraviolet

**Voc** Open circuit voltage

**XPS** X-ray photoelectron spectroscopy

# List of Figures

# Chapter 1 Introduction

The use of electronic and optoelectronic devices such as smartphones, tablets, video imaging, optical communications, biomedical imaging, night-vision, and many more, is an essential part of our daily lives. Moreover, in the near future a whole plethora of "smart" electronic devices and technologies like autonomous cars, holographic TV, and lab-on-a-chip will join this scenario. This trend stimulates an increasing interest in high performance energy converting and saving electronic devices. At the current rate of expansion, we are already facing fundamental limitations for both electronic and optoelectronic devices. For instance, the further development of electronic transistors is facing the limit of Moore's law, (stating that the number of transistors in a dense integrated circuit doubles approximately every two years) due to thermodynamic, thermal, and other fundamental limitations.[1] Another example, in the area of photovoltaics, is the so called Shockley-Queisser limit (the maximum solar conversion efficiency is approximately 33.7% due to spectrum losses, blackbody radiation and recombination).[2] In the past few years, two-dimensional (2D) quantum materials and their heterostructures have emerged as particularly promising components of novel devices that are ultimately small and offer improved speed and stability.

In this context, graphene, an atomically thick sheet made exclusively of carbon atoms, has attracted enormous interest due to its unique electrical and mechanical properties[3] since its first experimental isolation almost a decade ago. The range of both fundamental and practical applications envisioned for this outstanding 2D material is still further expanding.[4] Graphene is not only an excellent electrical and thermal conductor, but also represents the world's thinnest, strongest and stiffest material.[5] Its great technological potential has already been demonstrated in touch screens, capacitors, spintronic devices, fuel cells, batteries, sensors, transparent conductive films, high-frequency circuits, toxic material removal, molecular electronics, energy storage and conversion, as well as flexible electronics.[5–7]

Graphene displays an ultrahigh electron mobility of up to 500000 $cm^2\ v^{-1}\ s^{-1}$, as has been documented for suspended sheets at low temperature.[8] It also possesses a large specific surface area of 2630 $m^2\ g^{-1}$, a remarkable Young's modulus of 1.0 TPa,[9] and an impressive thermal conductivity of 5000 $Wm^{-1}\ K^{-1}$. Graphene also shows remarkable optical properties. For example, when deposited on an appropriate substrate, it can easily be discerned under an optical microscope, despite being only a single atom thick.[10,11] Furthermore, it exhibits linear optical absorption (scales with the number of layers).[12] Of special relevance for optoelectronic applications, graphene shows a broadband photon absorption as well as a phonon bottleneck for electrons with low energies (<200 meV).[13–15] This endows graphene with excited or hot carriers with longer lifetimes than in normal metals,[16] which facilitates their extraction before they relax to the Fermi level.

There are several established approaches to obtain well-defined graphene sheets, including the micromechanical or chemical exfoliation of graphite, chemical vapor deposition (CVD) growth, ultrasonic exfoliation, unzipping of carbon nanotubes, or the chemical, electrochemical, thermal, or photocatalytic reduction of graphene oxide.[17,18] Graphene is chemically inert and robust, allowing it to maintain its structural integrity even at higher temperatures in air (defects emerge above approximately 500°C)[19], and at low and high pH values in aqueous solution.[20]

Among the numerous exciting features of graphene, it's band structure the most remarkable (Fig. 1.1). Graphene is a semi-metal or zero-gap semiconductor, with a linear band dispersion at low energies, resulting in massless carriers that behave like relativistic particles described by the Dirac equation. The conduction and valence bands meet at the six Dirac points (charge neutrality points).[21] The zero band gap of graphene enables efficient tuning of the carriers from electrons to holes by electrostatic gating. However, this property at the same time constitutes the biggest drawback of graphene for optoelectronic device applications. In fact, graphene transistors exhibit only low on/off ratios of ≈5,[22] which prevents switching the devices into an off-state of minimal drain current leakage, leading to excessive power dissipation. According to the International 2012 (upgrade) Technology Roadmap for Semiconductors (ITRS), the off-current in graphene transistors needs to be reduced by at least four orders of magnitude to make them suitable for logic operations.[23] This limitation has stimulated an enormous amount of research into opening a band gap in graphene, for instance by chemical functionalization, in order to make it useful for integrated electronic circuits.[24,25]

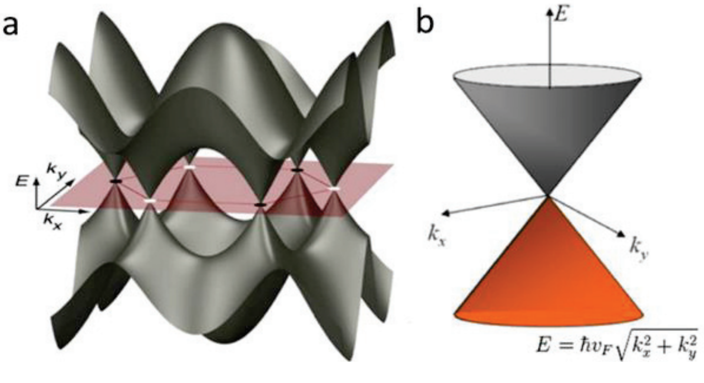

Figure 1.1. a) Band dispersion of graphene, with six Dirac points at the K points of the Brillouin zone. b) The linear energy dispersion centered around a single Dirac point. Figure adapted from ref. 25.

Introducing a sizable band gap in graphene by chemical modification requires covalent bond formation to remove π-bonded electronics states. To this end, different types of atoms or molecules have been used, ranging from hydrogen atoms to large organic polymers. The stoichiometric modification of graphene with hydrogen (graphane) and fluorine (fluorographene) is expected to result in insulating behavior with theoretical band gaps exceeding 3 eV. [26,27] However, thus far realized graphane samples proved to be quite disordered, such that the major effect observed was merely a reduction of carrier mobility. In general, a reproducible and scalable functionalization approach to induce a sizeable band gap and correspondingly high on/off ratio has not yet been experimentally demonstrated for graphene.[28] In order to avoid excessive conductivity or mobility degradation, attempts have been made to locally restrict the covalent functionalization.[5,17]

An alternative option to open a band gap is to pattern graphene into graphene nanoribbons (GNRs), whereby band gaps of up to 0.5 eV[26,29] have been obtained. In addition, substrate interactions like, for instance, those between epitaxial graphene and silicon carbide, have been reported to introduce a band gap (in this case, up to 0.26 eV).[30] Another strategy to tune the electronic properties of graphene without compromising the carrier mobility involves vertical heterostructures, made layer-by-layer in a precisely chosen sequence. Such van der Waals heterostructures[31] have attracted increasing attention in the past few years, encouraged by the discovery of more than a dozen different 2D crystals with a wide range of properties[31]. An important milestone was the achievement of high mobility on the order of $10^5$ $cm^2$ $V^{-1}s^{-1}$ in graphene encapsulated between two hexagonal boron nitride (hBN) sheets.[27]

The non-covalent attachment of 2D crystals to graphene via van der Waals bonds is a versatile approach to modulate the electronic and opto-electronic properties of graphene, as testified by the significant progress that has recently been made in this direction.[31] Suitable 2D crystals span a wide range of electronic materials with intriguing properties like topological insulator behavior,[32] superconductivity,[27] catalytic properties,[33] thermoelectricity[34] and ferromagnetism.[35] In this manner, the application scope of graphene can be strongly expanded in the form of novel materials with specifically tailored properties. Paraphrasing Geim and Grigorieva: “this atomic scale Lego works exceptionally well, better than one could have imagined”.[31]

The use of graphene-based heterostructures in photovoltaic devices has attracted particularly strong attention.[36,37] Along this line, efforts have been directed to exploiting hot carriers in graphene.[38–43] However, in most of the devices the photo-thermoelectric effect dominates over the photovoltaic effect,[38,39] such that due to the small Seebeck coefficient of graphene yields only very small photo-voltages on the order of few hundreds of microvolt.[39] For instance, photo-signals generated at graphene-metal junctions show predominantly thermoelectric contributions with only a small photovoltaic contribution.[40,43–45]

The goal of the present thesis has been to controllably tune the electronic properties of graphene through its implementation into two different types of heterostructures, in particular (i) lateral heterostructures obtained by chemical functionalization of graphene, and (ii) vertical heterostructures wherein graphene is combined with another 2D material or a thin metal layer for hot carrier extraction. The lateral graphene-based heterostructures are fabricated by two novel functionalization schemes, specifically a special type of oxidation reaction and the use of hyperthermal reactions. In the vertical graphene-based heterostructures, graphene is combined with a sheet of black phosphorous in order to create a photodetector. As another type of heterostructure, graphene-titanium oxide-titanium diodes have been realized, enabling the extraction of hot carriers from graphene.

# Chapter 2 Electrical and chemical properties of graphene and its heterostructures

## 2.1 Structural and electrical properties of graphene

Carbon is the fourth most abundant element on earth and the basis of all organic and organometallic chemistry. Due to its ability of forming different kinds of carbon-carbon bonds it exists as different allotropes, whose physical and chemical properties strongly depend on their dimensionality.[46] Among these systems, graphene, the 2D allotrope, has often been called the "mother" of all the other allotropes, as they can be obtained by wrapping, rolling or simple stacking of graphene.[46,47]

Graphene is a one-atom-thick planar sheet of carbons arranged into a honeycomb lattice, as depicted in Fig. 2.1a. The carbon atoms form a $sp^2$ hybridized network with three nearest neighbors, each at a distance of 1.42 Å, leaving one un-hybridized half-filled p-orbital perpendicular to the graphene plane for every carbon.[48] The finite termination of graphene results in two possible edge geometries, namely zigzag and armchair, as shown in Fig. 2.1b. The two types of endings show quite different electronic properties. Zigzag edges display a sharp density of states peak at the Fermi energy rendering them always a metallic behavior while armchair edges also can present semiconductor behavior. From the chemical point of view zigzag edges are more reactive than armchair.[49,50]

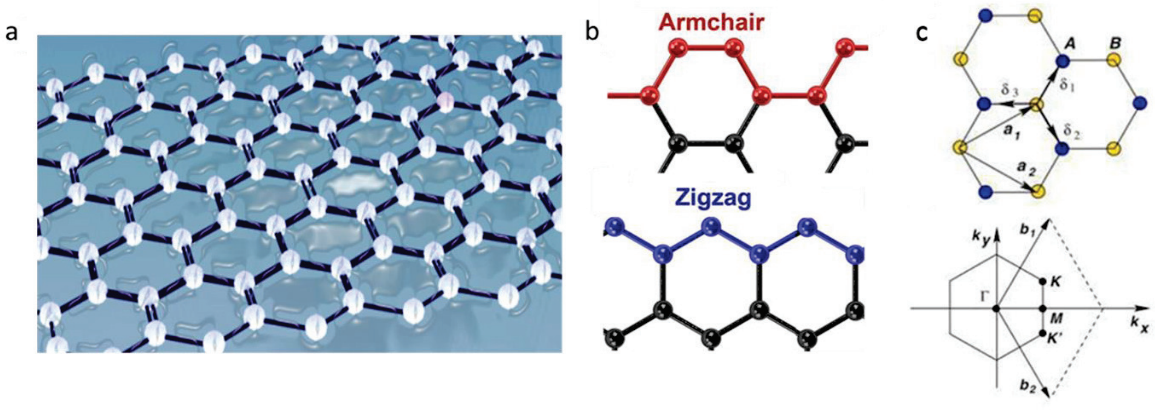

Figure 2.1. a) Schematic representation of the honeycomb lattice of graphene. b) Two different graphene endings, armchair (upper image) and zigzag (lower image). c) Real and reciprocal lattice structure of graphene. The first Brillouin zone comprises the high symmetry points Γ, M, K and K′.

The unit cell of graphene is a rhombus with a basis of two non-equivalent carbon atoms denoted as A and B (Fig. 2.1c). The real space ($a_1$, $a_2$) and reciprocal space ($b_1$, $b_2$) lattice vectors are given by:

$$\mathrm{a}_1 = \frac{a}{2}(3, \sqrt{3}), \qquad \mathrm{a}_2 = \frac{a}{2}(3, -\sqrt{3})$$

$$b_1 = \frac{2\pi}{3a}(1, \sqrt{3}), \qquad b_2 = \frac{2\pi}{3a}(1, -\sqrt{3})$$

where $a$ is the distance between neighboring carbon atoms (1.42 Å).[46] The density of carbon atoms is 39 $\mathrm{nm}^{-2}$ (equivalent to $3.9 \cdot 10^{15}$ $\mathrm{cm}^{-2}$). Of particular importance for the physics and especially for the electronic properties of graphene are the two reciprocal lattice points K and K´ (also known as the Dirac points), as will be explained in the following section.

### 2.1.1 Electronic properties

As a consequence of graphene's hexagonal lattice structure (Fig. 2.1c), its first Brillouin zone has two inequivalent points, the so-called Dirac points, which touch each other at a single point (Fig. 1.1). Their name derives from the linear band structure described by the Dirac equation for massless Fermions.[51] Using the tight-binding Hamiltonian[52], which considers only the first nearest neighbor interaction, to calculate the dispersion relation of the electrons near the two Dirac points (K, K´), yields the following band dispersion:

$$E_{\pm}(\vec{k}) = \pm\tau\sqrt{1 + 4\cos\frac{\sqrt{3}k_x a_i}{2}\cos\frac{k_y a_i}{2} + 4\cos^2\frac{k_{yx} a_i}{2}} \qquad (2.1)$$

where $a_i = \sqrt{3}a$ and $\tau$ is the transfer integral (hopping energy between nearest neighbors, with a typical value of 2.9 - 3.1 eV)[36]. Expanding equation (2.1) near the Dirac points leads to the following dispersion for low energies:

$$E_{\pm}(\vec{q}) \approx \pm\hbar v_F|\vec{q}| \qquad (2.2)$$

where $\vec{q}$ is the momentum relative to the Dirac point, ħ is Planck´s constant h divided by 2π, and $v_F$ is the Fermi velocity ($\approx 1 \cdot 10^6$ $\mathrm{ms}^{-1}$). This makes graphene a zero band gap semiconductor with massless Dirac quasiparticles. The electronic band structure and Dirac electrons impart outstanding properties on graphene, including an ambipolar electric field effect,[51] tunable carriers[9], high carrier mobilities,[8] as well as ballistic charge transport on the sub-micrometer scale.[53] Its exceptional properties have led to the hope that graphene might in the future replace silicon in electronics, for instance as component of field-effect transistors, as will be explained in section 2.3.

### 2.1.2 Optical properties

Based upon its zero band gap graphene is expected to absorb photons of all frequencies from the visible to the infrared, rendering it of interest for light-electricity conversion. Experimentally, absorption of photons with energies smaller than 0.2 eV has been detected.[54] The absorbance can be tuned by the carrier concentration in graphene and the temperature.[55]

Furthermore, due to its massless fermions, a freestanding graphene monolayer possess a universal value of optical conductance[56] in the visible frequency range equal to:

$$\sigma_0 = \frac{e^2}{4\hbar} \approx 6.08\ x\ 10^{-5}\Omega^{-1} \qquad (2.3)$$

Applying the Fresnel equation in the thin-film yields:

$$T = (1 + 0.5\pi\alpha)^{-2} \qquad (2.4)$$

where $\alpha = \frac{\sigma_0}{(\pi\varepsilon_0 c)}$. Combining the two equations above gives an optical transmittance of ≈97.7% of the incident light. As graphene reflects less than 0.1% in the visible range, the optical absorption of a graphene monolayer is obtained to 2.3%, a significant value for a material that is only one atom thick. The absorption strength increases linearly with the number of layers, such that the graphene thickness (number of monolayers in a sheet) can easily be determined using an optical microscope.[57] As briefly mentioned before, the optical transmission of graphene can be tuned by doping. This is enabled by the low density of states near the Dirac point, due to which a Fermi level shift causes a significant change of the charge density, which in turn modulates the transmission of the material.[9]

In contrast to conventional semiconductors, phonon scattering is expected to play an important role in graphene due to the lack of a band gap. Correspondingly, the excited carrier lifetimes in graphene are very short, and depend on its structural quality and carrier concentration.[13,58] Two major relaxation processes have been identified by time-resolved measurements. The faster one, associated with electron-electron intra-band collisions and phonon emission, occurs on the order of hundreds of femtoseconds, while the slower (hundreds of picoseconds) one is related to electronic inter-band relaxation and cooling of hot phonons.[15,59,60]

## 2.2 Chemical functionalization of graphene

The chemical functionalization of graphene has received enormous interest in the scientific community due to the possibility to control its electronic properties, as well as enabling its use in chemical sensors or molecular electronics.[61] The covalent attachment of atoms or molecules causes re-hybridization of the carbon atoms from the planar sp$^2$ to the non-planar sp$^3$ hybridization. In principle, the attachment can occur at both faces of the sheet, as well as at the sheet edges, the latter of which are usually more reactive than the basal plane. The chemical reactivity of the edges has been predicted to depend on their structure. For instance, according to theory zigzag edges are more reactive than armchair ones.[62] With respect to the basal plane, site-dependent of reactivity has been revealed on the basis of the ionization energy (Fig. 2.2).[63] In Fig. 2.2, it is illustrated for a smaller graphene model system, how defects increase the chemical reactivity with respect to the corresponding intact structure.

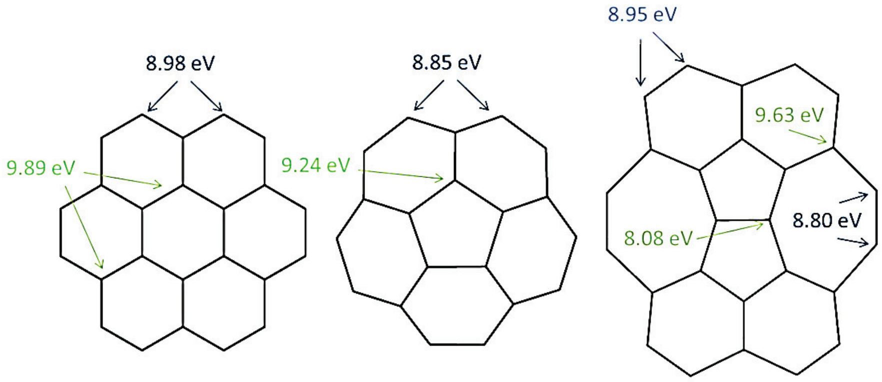

Framework of coronene ($C_{24}H_{12}$)

Framework of corannulene ($C_{20}H_{10}$)

Framework of $C_{26}H_{12}$

Figure 2.2. Theoretical local ionization energies in dependence of the carbon bonding configuration. Figure adapted from ref. 63.

In the following sections, the major types of covalently functionalized graphene are described.

## 2.2.1 Hydrogenated and fluorinated graphene

Covalent linkage of hydrogen atoms to graphene results in a new material called graphane (for full coverage).[64] Graphane is predicted to have a band gap of about 3.5 eV. In the first experimental report of hydrogenated graphene,[65] electrically behavior was observed at low temperatures. At room temperature, the charge neutrality point was observed to shift to a gate voltage of +50 V, indicative of hole doping with a concentration on the order of $3 \cdot 10^{12}$ cm$^{-2}$.

Experimental studies on graphene with a controlled amount of attached hydrogen[66] have shown mobility decrease proportional to the coverage of modified atoms on the graphene plane (Fig. 2.3). Specific type of hydrogenated graphene has been predicted by theory to behave as ferromagnetic semiconductor with a small indirect gap. In the special case of half-hydrogenation, breaking of the delocalized π-bonding network of graphene leaves the electrons unpaired and localized in the non-hydrogenated carbon atoms.[67]

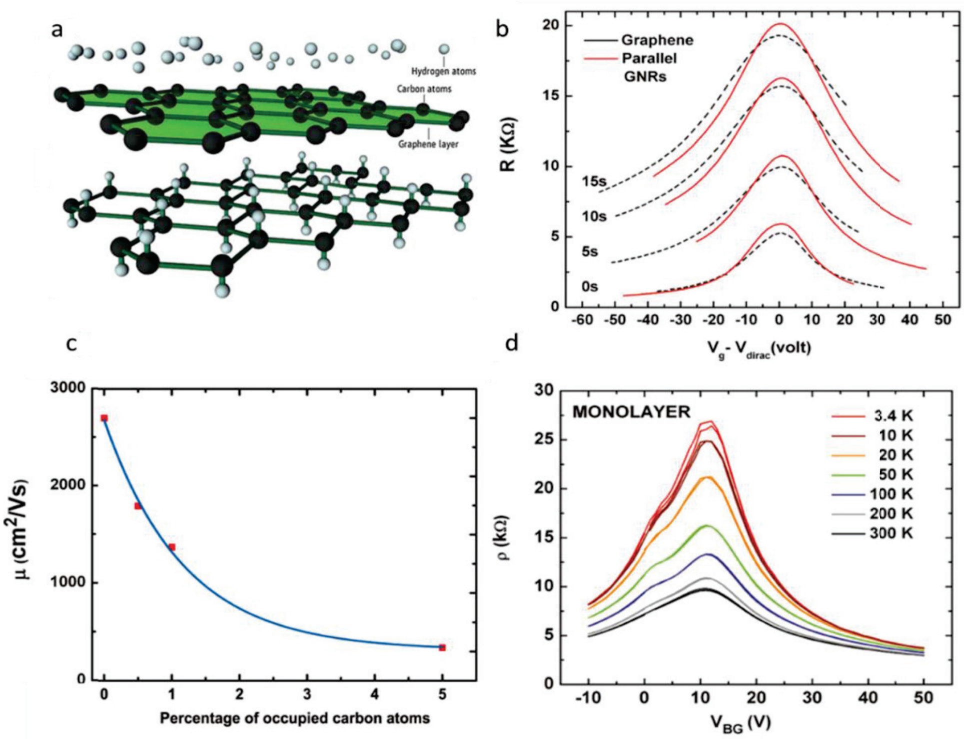

Figure 2.3. a) Sketch of the chemical structure of graphane. b) Electrical resistance vs. ($V_g$-$V_{Dirac}$) with increasing hydrogenation time (0, 5, 10, and 15 s) for a graphene sheet (dashed black lines) and GNRs (red lines). c) Carrier mobility vs. percentage of hydrogenated sites. d) Resistivity (R) vs. $V_{BG}$ for partially hydrogenated graphene as a function of temperature. Figure adapted from refs. 64, 66.

Another chemical derivative of graphene is the so-called fluorographene, whose synthesis was first reported in 2010.[68] Since then, several studies have shown that the electrical character of fluorographene ranges from semi-metallic to insulating, depending on the stoichiometry. Theoretical calculations predict that partial fluorination allows tuning of the band gap from 0.8 to 2.9 eV, and that the resistivity can reach values as high as $10^{12}$ Ω·m. [68,69]

A recent study of fully fluorinated graphene reported a band gap of 3.8 eV, the highest value so far reported for any functionalized graphene.[70] Fluorine chemisorption also dramatically changes the optical properties of graphene (rendering it transparent).[70] However, the high reactivity of fluorine against silicon and its toxicity pose major obstacles in the implementation of fluorographene for electronic devices.

## 2.2.2 Graphene oxide

Graphene oxide (GO) consists of a single-layer of graphite oxide and is usually produced either by oxidation of graphene monolayers, or oxidation of graphite using strong acidic media or ozone[5], followed by dispersion and exfoliation in water or organic solvents. The resulting GO comprises randomly distributed intact graphitic regions, interspersed with oxygenated regions. The oxygenated functional groups have been identified to be mostly hydroxyl and epoxy groups on the basal plane, with smaller amounts of carboxyl, carbonyl, phenol, lactone, and quinone motifs at the sheet edges.[71–73]

Theory suggests the possibility of creating and tuning the electronic band gap of GO by varying the oxidation level.[5,17,74] However, owing to its ill-defined structure and composition, GO is less suitable for electronic applications, since the density of oxygenated groups can strongly affects its electronic, mechanical, and electrochemical properties, and it is very difficult to precisely control the specific stoichiometry.

It is noteworthy that GO exhibits several intriguing properties,[17,75] such as photoluminescence, ultrafast optical dynamics, nonlinear optical properties and electrocatalytic activity. GO can furthermore serve as a precursor to graphene or as starting basis for more elaborate graphene derivatives through the covalent attachment of organic groups to its surface. Chemical reduction of GO by various means removes the oxygen groups and restores most of the $sp^2$ carbons.[76,77] However, the reductive treatment is not able to completely remove all oxygen groups and defects still remain.

## 2.2.3 Graphene with covalently organic groups

Much work has also been devoted to the covalent attachment of organic molecules to the carbon framework of graphene. This may open a wide range applications, including the detection of biomolecules, pH sensors, and waste management, for example.[5,17,77] Two major approaches are commonly used for this purpose, specifically (i) covalent bond formation with free radicals or dienophiles, and (ii) the formation of covalent bonds between organic molecules and the oxygen groups of GO. In free radical reactions, peroxides[78] or diazonium salts[79] are often used (Fig. 2.4a,b). Another option is the addition of nitrenes generated from azides (Fig. 2.4c).[80]

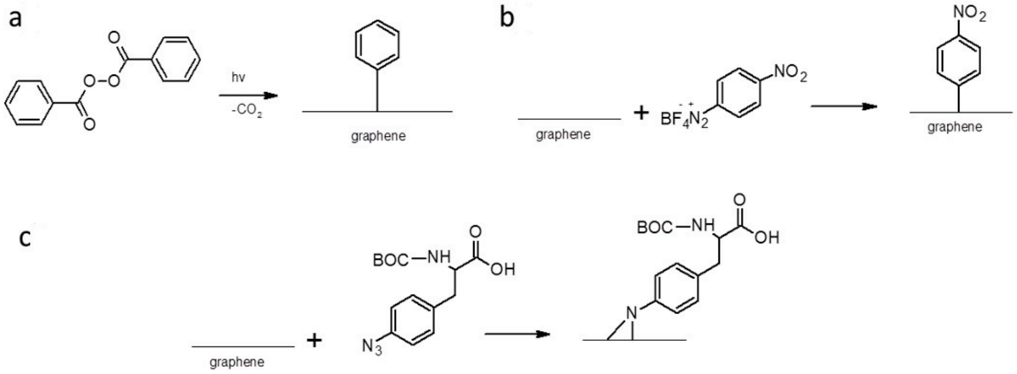

Figure 2.4. Examples of covalent functionalization of graphene via radical/nitrene addition, making use of a) a peroxide, b) a diazonium salt, and c) an azide compound. Figure adapted from refs.78–80.

## 2.3 Raman spectroscopy of graphene

Raman spectroscopy is one of the most widely used and powerful characterization methods for graphene.[81] It gives valuable information about the quality and quantity of layers, as well as the stacking order, electron-phonon coupling, doping levels, the presence of mechanical strain and, in the case of graphene nanoribbons, edge chirality.[82–84] Three major peaks (D, G and 2D), whose underlying scattering mechanism is illustrated in Fig. 2.5, emerge in the Raman spectrum of single layer graphene (SLG), multilayer graphene (MLG) and graphite.

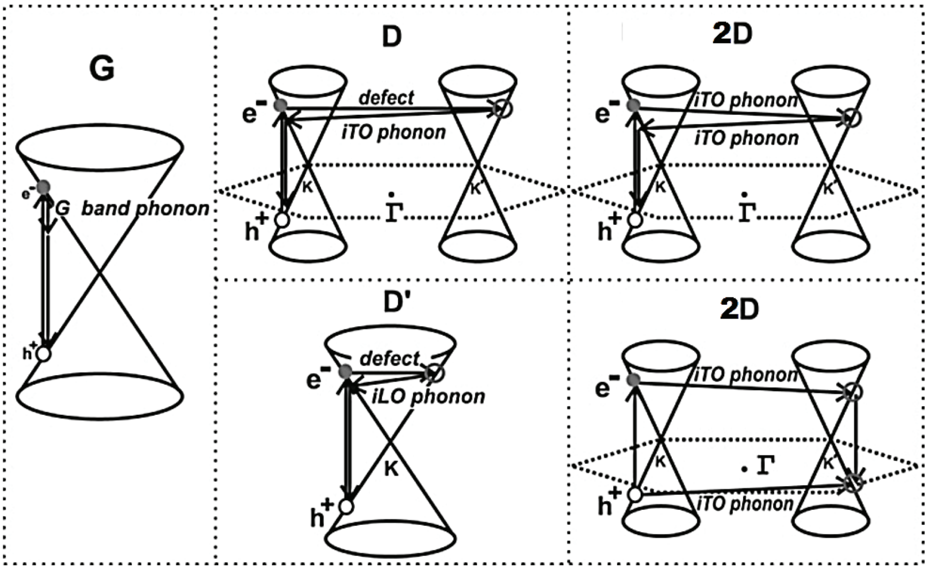

Figure 2.5. The characteristic Raman peaks of graphene and their underlying scattering mechanisms including (from left to right) the G-band, the D- and D’-band, and the 2D band. The latter can arise from a double- or triple-resonance, two photon process. Figure adapted from reference 83.

The G peak at ≈1582 $cm^{-1}$ is associated with the doubly degenerate in-plane transverse and longitudinal optical phonon modes ($E_{2g}$) at the Γ-point in the Brillouin zone.[82,83] This peak is independent of the number of layers, although it is sensitive to doping and strain.[81,85] The 2D peak (at ≈2700 $cm^{-1}$) is the D peak overtone, originating from a second-order process involving two in-plane vibrations near the K point. The 2D peak is especially relevant because it enables determining the manner of stacking, as well as the number of layers (mostly based on the number of Lorentzians needed to deconvoluted the peak; SLG exhibits only one peak with a full-width half maximum -FWHM- of ≈25 $cm^{-1}$).[81,82] The D peak, located at ≈1350 $cm^{-1}$, appears only in graphene with defects and originates from first-order boundary phonons.[9] This peak is important because it allows calculating the density of defects or attached groups in graphene.[82]

# 2.4 Schottky and pn junctions

## 2.4.1 Schottky junctions

When a metal (or semimetal) gets in contact with a semiconductor two different kinds of junctions, from an electrical point of view, can be formed. The first type, termed "Schottky junction, acts like a current rectifier. The second type, called "Ohmic" junction, follows the law $V = I \cdot R$. Ohmic junctions are usually obtained when the metal is combined with a close-to metallic system (i.e., highly doped semiconductors). In contrast, Schottky junctions are usually formed when the semiconductor is only little doped. The ideal Schottky junction ideally acts as a perfect diode with high current and very low resistance in the forward direction (''on'' state) and no current in the opposite direction (reverse direction or ''off'' state).[86]

In a typical Schottky junction (Fig. 2.6) a metal with work function $\Phi_M$ and a Fermi level ($E_{FM}$) is in intimate contact with a semiconductor with Fermi level $E_{FS}$ and an electron affinity $\chi$. In order to reach equilibrium, charge transfer occurs until the two Fermi levels are aligned. In the course of this equilibration process, electrons are transferred from the n-type semiconductor (or holes from the p-type semiconductor) to the metal. This leads to a region within the semiconductor that is depleted of free charge carriers, called the depletion layer, of width w. The excess carriers in the depletion layer are compensated by a thin layer of opposite-sign charges on the metal surface. Depending on the type of doping, there is an upward or downward band bending within the semiconductor's depletion layer. The interface region with charges of opposite sign behaves like a capacitor and restricts further charge transfer, thereby imparting the rectifying behavior. In the close proximity of the interface a difference in the potential due to the charge is created, which is named the "built-in potential". At equilibrium, this potential barrier generates a discontinuity of the allowed energy states, which results in the formation of an energy barrier at the metal-semiconductor interface, known as the Schottky barrier. This magnitude of this barrier is determined by the metal work function and the semiconductor electron affinity, but not by the voltage bias.[86–88]

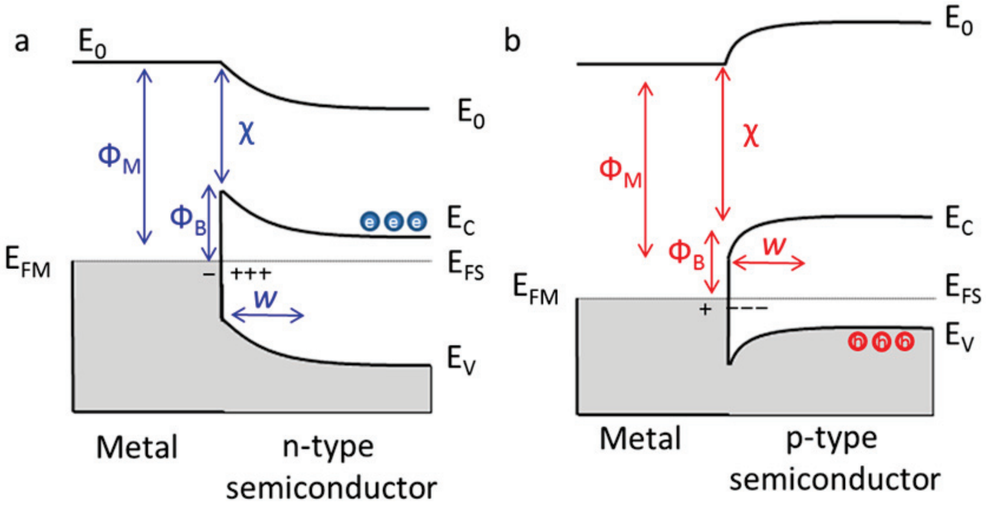

Figure 2.6. Band diagram of the Schottky junction between a metal and a) an n-type semiconductor and b) a p-type semiconductor. $\Phi_M$ is the metal work function, $E_{FS}$ is the Fermi level of the semiconductor, $\Phi_B$ is the Schottky barrier height, $\chi$ is the semiconductor electron affinity, and *w* the width of the depletion layer.

Current transport through Schottky junctions is mainly due to electrons from the n-type semiconductors or holes from the p-type semiconductor. If the carrier concentration is low (like in graphene), the current is usually carried by thermally excited electrons. An alternative mechanism is (thermionic) field emission which may include tunneling through the barrier.[87]

Schottky diodes are ubiquitous in numerous types of electronic devices such as solar cells, photodetectors, transistors, microwave mixers and integrated circuits.[89,90]

## 2.4.2 pn junctions

The formation of a pn junction has similarities to that of a Schottky junction. When the electrons from the n-type semiconductor or holes from the p-type semiconductors move to the other side of the junction in order to establish equilibrium, they leave behind excess charges. The accumulated charges on the n-type side (holes) and on the p-type side (electrons) create a depletion region. This leads to an electric field (built in potential $\Phi_i$) across the interface (see Fig. 2.7). The region outside the depletion width, on both sides of the junction, is called the quasi-neutral region.[91]

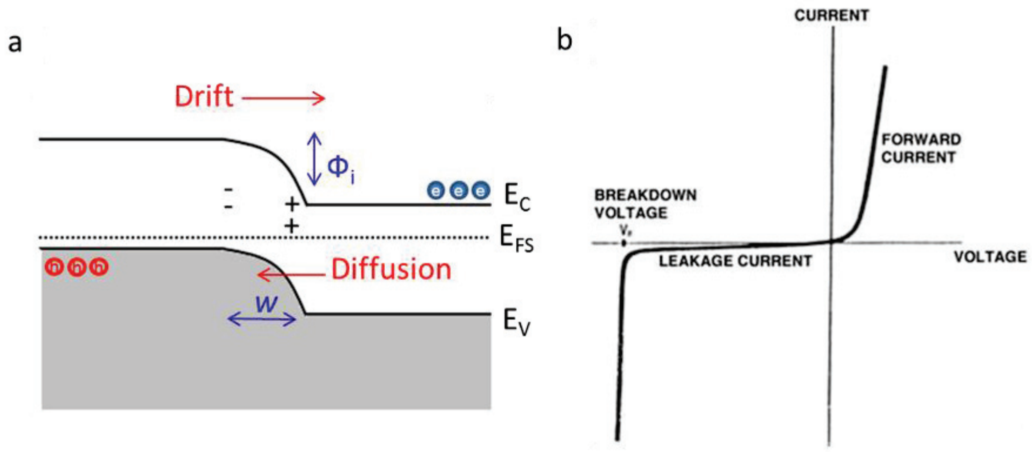

Figure 2.7. a) Band diagram of the pn junction between an n-type semiconductor and a p-type semiconductor. b) Rectifying I-V curve of an ideal pn junction.

In contrast to Schottky diodes, pn junctions are formed by joining n- and p-type semiconductor materials. However, like Schottky barriers, ideal pn junctions permit current in one direction and block it in the opposite one. When the p-side is biased positively with respect to the n-side, the junction is under forward bias, giving rise to a current that increases rapidly as the voltage increases. Conversely, when the p-side is negatively biased, the junction is under reverse bias and the current flow is blocked. Upon increasing the reverse bias, a point is reached when the current suddenly increases. This critical voltage is called the junction breakdown voltage. The I-V characteristic of an ideal pn diode is presented in Fig. 2.7b. In contrast to a Schottky barrier, the current through a pn junction occurs mainly via the drift of carriers, which is caused by the presence of an electric field, combined with carrier diffusion, which is driven by the carrier concentration gradient in the semiconductor.[91,92]

Semiconductor pn junctions are an important ingredient of optoelectronic devices including solar cells and light-emitting devices. One of the key reasons for the success of the pn junction compared to Schottky junctions lies in its ability to be locally modulated via an applied bias or the suitable design of the materials' band energies.[93]

## 2.5 Graphene-based pn and Schottky junctions

The absence of a band gap in graphene has motivated research to combine graphene with a semiconductor to obtain either Schottky junctions where graphene acts as the metal, or pn junctions where graphene is either the p-type or n-type component. In the following, these two types of devices are described in more detail.

In order to define a pn junction within a graphene sheet, a combination of top and bottom electrostatic gates has been used to create electrostatically doped regions. [94,95] Chemical doping has also been explored in order to create pn junctions. One common approach is to modify one half of a graphene sheet with donor (to create n-type graphene) or acceptor (for p-type graphene) molecules, while leaving the other half pristine.[42,96] Controlling the pristine half of the graphene by electrostatic gating then yields diodes in the configuration pp+ or pn.[98] This strategy can be extended by including additional doped or undoped graphene sections in order to obtain pnp or npn configurations.[97,98] Graphene diodes exhibit very interesting physics, including Klein tunneling (carrier incident normal to the pn interface)[99] and snake trajectories.[100] Of further interest are junctions between graphene and other semiconductors (like Si), where the doping can be tuned in both materials.[101,102]

The following sections describe how the pn junction has been exploited for device applications.

## 2.6 Graphene-based field-effect transistors

It has been stated the exceptional carrier mobility of graphene (one order of magnitude higher compared to silicon),[9] along with the high attainable current density, the most promising application for graphene will be in electronics. In this context, FETs have attracted the most attention.[21,103,104] Graphene FETs offer the advantage of flexibility and transparency, as demonstrated in Fig. 2.8,[105] both of which are difficult to achieve by other approaches. However, the impossibility to turn graphene device off still represents a major hurdle. While graphene nanoribbons face the problem of scalability, alternative approaches using chemically modified graphene, epitaxial graphene or chiral stacking of monolayer graphene are actively pursued by the scientific community.[5,26,47]

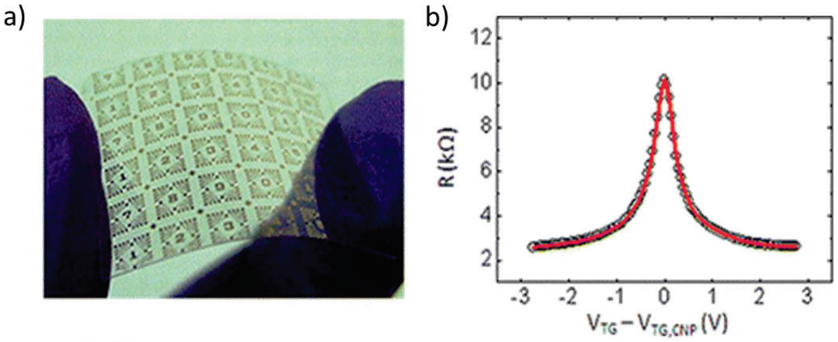

Figure 2.8. a) Graphene-based transparent and flexible FET and b) the characteristic transfer curve with an on/off ratio of ≈5. Figure adapted from ref. 105.

Although the zero band gap of graphene limits its application range, it is nevertheless highly useful for devices such as radio frequency FETs which do not require a large on/off ratio. Such devices require an ultra-high carrier mobility, which graphene is able to supply. In 2010, Lin *et al.* demonstrated an epitaxial graphene-based FET with a cutoff frequency of 100 GHz.[106] Since then, several other examples have been demonstrated,[28,107,108] with a maximum intrinsic cutoff frequency of 300 GHz.[109] Remarkably, such type of devices have also been fabricated on flexible substrates, reaching cutoff frequencies of up to 1.3 GHz.[110] Finally, within the ongoing struggle for further miniaturization the fabrication of graphene-based single electron transistors (SET) has attracted attention. It has been experimentally demonstrated that ultra-small graphene quantum dots behave like conventional large size SETs.[111]

## 2.7 Graphene-based optoelectronic devices

The requirements for a transparent conducting material to be technologically relevant are a low sheet resistance $R_s$ <100 $\Omega sq^{-1}$ and high transparency T >90% in the visible range.[26] State-of-the-art transparent conductors are mainly semiconductor-based. However, these materials are facing signifcant problems, including ever-increasing price, scarcity of one of the components, difficulties in patterning, low chemical stability and the degradation of their electrical properties.[26,36] The low resistivity, high transmittance, good chemical stability, and low cost of graphene make it an close-to- ideal conductive film.[112] Among other works in this area,[113–115] Blake *et al*.[116] have reported the best graphene transparent conducting film so far, which achieves $R_s$ = 400 $\Omega sq^{-1}$ and T ≈98% with n-doped graphene.

One of the most important optoelectronic devices is the photodetector. In these devices the absorbed photon energy is converted into an electrical signal.[37] Similar to the conducting films described above, the field of photodetectors has been predominantly developed using semiconductors materials.[117] However, the optical absorption of semiconductors is limited by their band gap, such that smaller photon energies cannot be detected.[36] In contrast, graphene's zero band gap enables it to absorb photons from the ultraviolet to the terahertz range.[37,118] As another advantage, graphene's high carrier mobility provides access to fast photodetection. Toward exploiting the fast photoelectrical response and broadband absorption of graphene, different device configurations have been explored,[44,119,120] such as metal-graphene-metal devices,[119] exhibiting a responsivity (R) of ≈6.1 mA/W and an internal quantum efficiencies (IQE) of ≈16%. Moreover, for hybrid devices like quantum-dots/graphene[121] an IQE of ≈25% and R ≈107 A/W has been reported, while graphene-semiconductors heterostructures[122] yielded an IQE of ≈10% and R ≈0.13 A/W.[36] Since graphene is compatible with silicon-based technologies, some of these devices have already reached a level of competitiveness with existing technologies.[37] However, the device performance is limited for SLG due to its short photocarrier lifetimes. The extraction of these hot-carriers, while challenging, is highly desirable for the implementation of graphene into solar harvesting systems. This problem and possible solutions are further discussed in chapters 6 and 7.

# Chapter 3 Experimental techniques

## 3.1 Graphene sample preparation

Although the detailed sample preparation varies with the specific type of graphene device to be investigated, in most cases it started with CVD graphene or exfoliated graphene on a Si-$SiO_2$ substrate (4 x 4 $mm^2$, oxide layer thickness of 300 nm) equipped with position markers. Initially, the Si-$SiO_2$ substrates were cleaned by immersion in N-ethyl-pyrrolidone (NEP), acetone and isopropanol for ≈20 minutes each in an ultrasonic bath (room temperature, 37 kHz), followed by 10 min oxygen plasma treatment (100 W, gas pressure of 0.3 mTorr) to remove any organic contamination. The following sections detail the manipulation of the two different types of graphene.

### 3.1.1 Transfer of CVD graphene

The CVD method for growing graphene yields sheets of large area (on the order of $mm^2$), which cannot be reached by most other techniques, in particular mechanical exfoliation of graphene. The CVD graphene is typically obtained on metallic surfaces such as copper using relatively straightforward methodologies.[123] Nevertheless, the presence of the underlying substrate limits the applicability of CVD graphene in electronics, as the intimate coupling between the metal and graphene significantly alters the electronic properties of the latter. For instance, a strong interaction between graphene sheets and some metals such as Ni(111) can result in an altered density of states (DOS) along with n-type doping of graphene, whereas graphene on less interacting surfaces like Pt(111) largely preserves the intrinsic Dirac cone shape, similar to free-standing graphene.[81,123] Therefore, various methods have been developed to transfer the graphene film onto a desired substrate.[124] While several reliable methods are now available, further improvements are still needed, since the electronic quality of the transferred CVD graphene is often inferior to that of exfoliated graphene.

For the present work, the wet transfer method outlined in Fig. 3.1 has been employed. It involves first coating the substrate by polymethyl-methacrylate (PMMA) as a mechanical support for the graphene. In this manner, wrinkle formation in the sheet is minimized, leading to a better quality of the transferred graphene.[124] The PMMA-graphene-Cu stack is then placed on top of an etching solution (a mixture of 7.5 ml of hydrochloric acid (36%, w/v), 2 ml of hydrogen peroxide (30%, w/v), and 40 ml of water) for ≈10 min. The

Cu reacts with the HCl to form the water soluble $CuCl_2$ (see reaction scheme below) which is easily removed later on by rinsing.

$$Cu_{(s)} + 2HCl_{(aq)} \rightarrow CuCl_{2(aq)} + H_{2(g)}$$

After complete dissolution of the copper, the sample is picked up from below with a glass slide and placed in DI water in order to remove all the residues. Finally, the PMMA-covered graphene is fished out with the target substrate, followed by dissolving the PMMA in acetone.

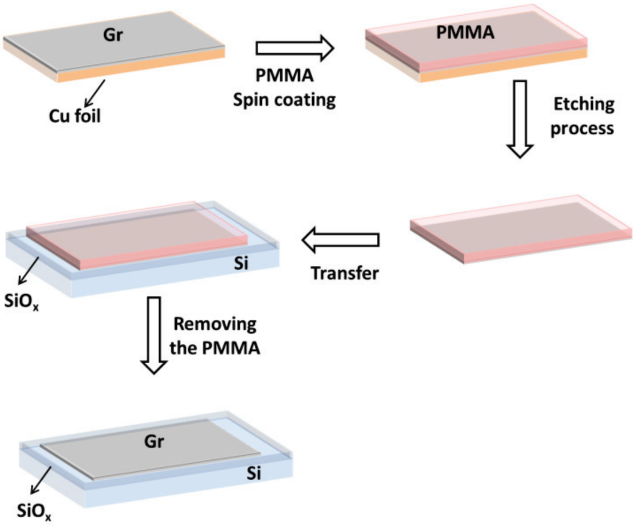

Figure 3.1. Schematic diagram of the wet transfer of CVD graphene from Cu foils onto Silicon substrates using PMMA as a support layer.

## 3.1.2 Mechanical exfoliation of graphene

The method used in this thesis is similar to the one used by Novoselov *et al.*[21] in their pioneering work on isolating graphene monolayers. An adhesive scotch tape was used to repeatedly peel layers from a crystal of highly-oriented pyrolytic graphite (HOPG). Subsequently, the scotch tape decorated with graphene was pressed against the marker substrate. The thickness of the graphene was judged from the optical contrast between graphene and the substrate under an optical microscope; as already mentioned, the optical absorption of a multilayered sheet increases linearly with the number of graphene layers, and hence the latter quantity can be determined by dividing the opacity by 2.3%.[57]

## 3.2 Sample characterization

### 3.2.1 Atomic force microscopy

Atomic force microscopy (AFM) served to detect whether the graphene was sufficiently clean, as well as to determine the thickness of the 2D materials or contact metals used in the different heterostructures. In an AFM (Fig. 3.2a), a tip is mounted on a flexible cantilever and brought close to the surface of the sample. As apparent from the dependence of potential energy on distance (Fig. 3.2b), when the SiN tip is very close to the surface, the tip and surface start to repel each other. The instrument measures the cantilever deflection caused by this repulsion forces, according to Hooke's Law: $F = -kx$ ($k$ is the spring constant of the cantilever and $x$ is the deflection due to the tip-sample interaction).[125] Forces in the range of $10^{-13}$ to $10^{-6}$ N are measured by the piezo-electric controller and an internal feedback system. The cantilever deflection is detected from the change in the position of a reflected laser into a photodetector, as sketched in Fig. 3.2c. There are three different AFM operation modes, namely (i) the non-contact mode, where the distance between the tip and the sample is between 10 Å and 100 Å, (ii) the contact mode, with the distance kept below 5 Å, and (iii) the intermittent contact or tapping mode, where the distance is between 5 and 20 Å.

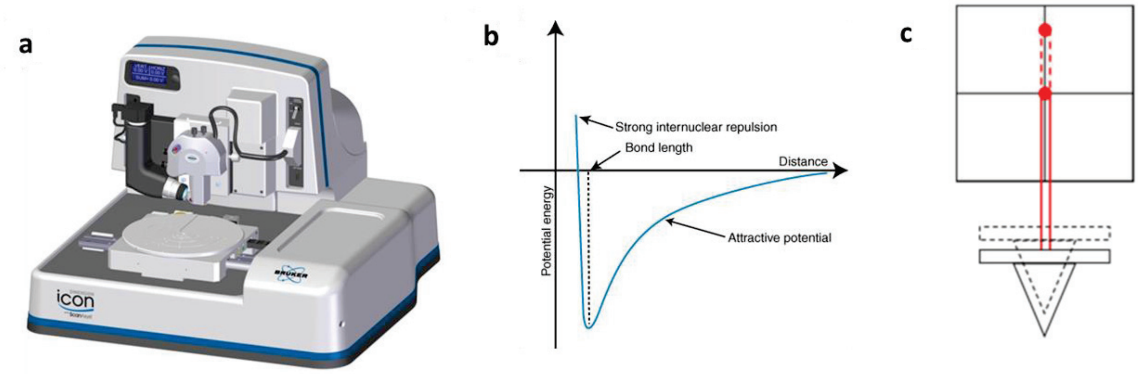

Figure 3.2. Schematic diagram of a) the AFM (Bruker Dimension Icon) used in this work. b) Plot of potential energy versus tip-sample distance. c) Sketch of the cantilever displacement detection mechanism. (Images adapted from the operation manual).

All AFM measurements in this thesis were performed in tapping mode, a non-contact mode where the tip oscillates back-and-forth close to the surface, such that the tip-sample interaction is restricted to a short period of time. The reduction of the cantilever oscillation amplitude due to tip-sample interaction or variations of topological height is converted to a 3D image. The tapping mode was selected due to its suitability for soft or deformable surfaces, such as (chemically modified) graphene. Furthermore, the used tips were made of SiN as a chemically inert material.

### 3.2.2 Raman spectroscopy

In this work, Raman spectroscopy was mostly used to determine the doping, the purity and the number of layers for the different 2D materials. This fast and non-destructive technique offers sub-µm spatial resolution and yields valuable electronic and structural information of the system.[82] The measurements were performed using a confocal set-up equipped with He-Ne, Nd:YAG and Ar-ion lasers of different wavelengths (488 nm, 533 nm and 633 nm), and a laser power on the order of 1 mW. The intensity of the Raman modes of graphene in general depends on the excitation energy. For instance, the $I_{(D)}/I_{(G)}$ ratio of strongly functionalized graphene is approximately 8 for an excitation energy of 2 eV, while it assumes a value of 3 for an excitation energy of 2.7 eV.[84] The diffraction-limited laser spot enabled measurements with a peak-to-peak resolution of about 1 $cm^{-1}$. Raman maps were recorded by placing the sample on a piezo-scanner table.

Photon absorption by a molecular system can occur by exiting an electron from the ground state of the molecule either into an unoccupied level of higher energy, or a virtual state. A virtual state is forbidden by quantum mechanics and therefore undergoes fast relaxation. If the relaxation takes place with concomitant excitation of a phonon, a so-called Stokes shifted photon is emitted. If, by contrast, the energy of a phonon is transferred onto the relaxing electron, a photon of higher energy is emitted, corresponding to the so-called anti-Stokes shift.[126] Raman spectroscopy thus provides access to a range of vibrational modes, provided they are associated with a change of polarizability of the system process.[127]

Confocal Raman microscopy, which enables the acquisition Raman spectra with spatial resolution, was first developed by Marvin Minsky in 1988.[128] In such measurement, the laser beam is focused through a pinhole that collimates the light onto a dichromatic mirror and then into a microscope objective to focus the laser on the sample. The light reflected from the sample passes through a second pinhole to a spectrometer combined with a CCD camera for signal detection, as depicted in Fig. 3.3.

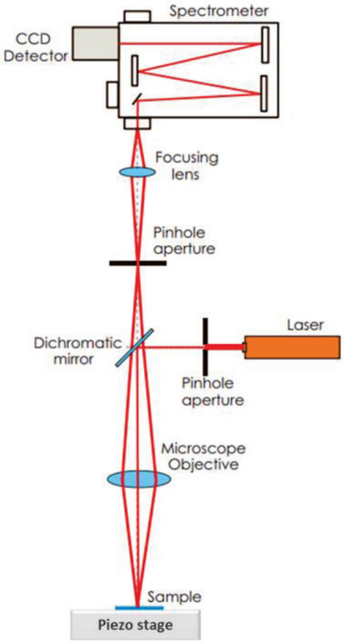

Figure 3.3. Schematic depiction of a confocal Raman spectrometer (image adapted from Princeton Instruments).

In this thesis, Raman spectroscopy is mainly used to determine the $I_{(D)}/I_{(G)}$ ratio in order to calculate the modification degree of the graphene samples. Furthermore, shifts of the 2D and G peaks are utilized to determine the doping level of graphene or black phosphorus.

### 3.2.3 Electrical characterization

Electrical transport measurements were carried out with three different set-ups. In all three cases, the electrical setup shown in Fig. 3.4a was used. Specifically, a Keithley 2400 electrometer was used as voltage source, while a current-to-voltage converter (FEMTO DLPCA-200) served to amplify the output current before being measured by a Keithley 2000 multimeter. This setup was mainly used to determine the diode behavior of the different systems, as well as the sheet resistance which is linked to the degree of modification of graphene (see chapters 4 and 5). For all measurements, the samples were glued into a chip carrier with silver paste, and subsequently the pads were bonded by gold wires. Tuning of the Fermi level in the different materials was accomplished by applying a gate voltage with a Keithley 2400 electrometer. The applied gate voltage leads to charging of a plate capacitor, whereby electrons or holes are accumulated in the conductive channel (see Fig 3.4b). Temperature dependent electrical measurements were carried out under vacuum within either a liquid nitrogen or liquid helium cryostat. The room temperature measurements were conducted under ambient conditions.

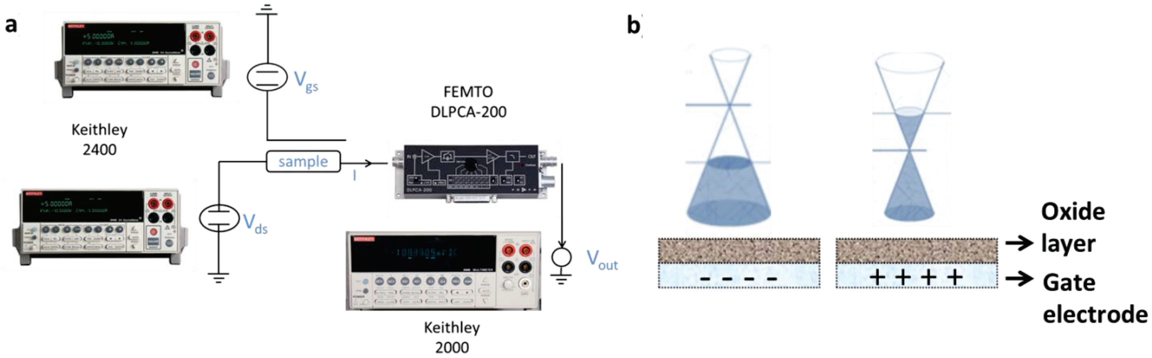

Figure 3.4. a) Schematic diagram of the setup used for the electrical measurements. Source and gate voltage were applied using a Keithley 2400 electrometer, with the signal being amplified by a femto DLPCA-200 and read out with a Keithley 2000 multimeter. b) Shift of the Fermi-level of graphene upon applying a negative or positive gate voltage.

Photocurrent measurements were carried out with the same setup; however, the system was coupled to a confocal microscope whit a laser probe, as is going to be explaining in the next section.

### 3.2.4 Scanning photocurrent microscopy

Scanning photocurrent microscopy (SPCM) was performed with a confocal laser scanning microscope (Leica TCS SP2), equipped with a piezoelectric table that holds the chip carrier during the measurements (Fig. 3.5a). In this manner, spatially-resolved photocurrent maps were obtained from the graphene-based pn heterojunctions (see chapter 7) and MIM diodes (see chapter 6). The Leica microscope operates with Helium-Neon (HeNe operating at 633 nm), GreNe (543 nm) and Ar/ArKr (458 nm, 488 nm and 514 nm) lasers at powers in the range of 1 µW to 430 µW. Variation of the laser power and wavelength allows distinguishing different types of photocurrent mechanisms. For instance, the dependence of photocurrent on laser power can yield information about trap states, and the occurrence of a photocurrent maximum at a certain laser power is indicative of a thickness limitation (see chapter 7). Furthermore, the photocurrent dependence on laser wavelength is not only useful to assess the practical application potential of the devices, but also yields hints about photocurrent mechanism (see chapter 6).

The confocal microscope and the achievable spatial resolution are identical as described for the Raman measurements (section 3.2.2). In this thesis, spatially resolved measurements were needed to elucidate the photocurrent generation mechanism. For example, the photo-thermal effect is usually associated with a higher photocurrent close to the metal contacts, whereas a photovoltaic signal tends to be more uniformly distributed over the sheet (see chapter 7). The electrical measurement principle is the same as for the electrical measurements (section 3.2.3). All SPCM and reflection images in this thesis were recorded under ambient conditions and processed using the WSxM image processing software.[129]

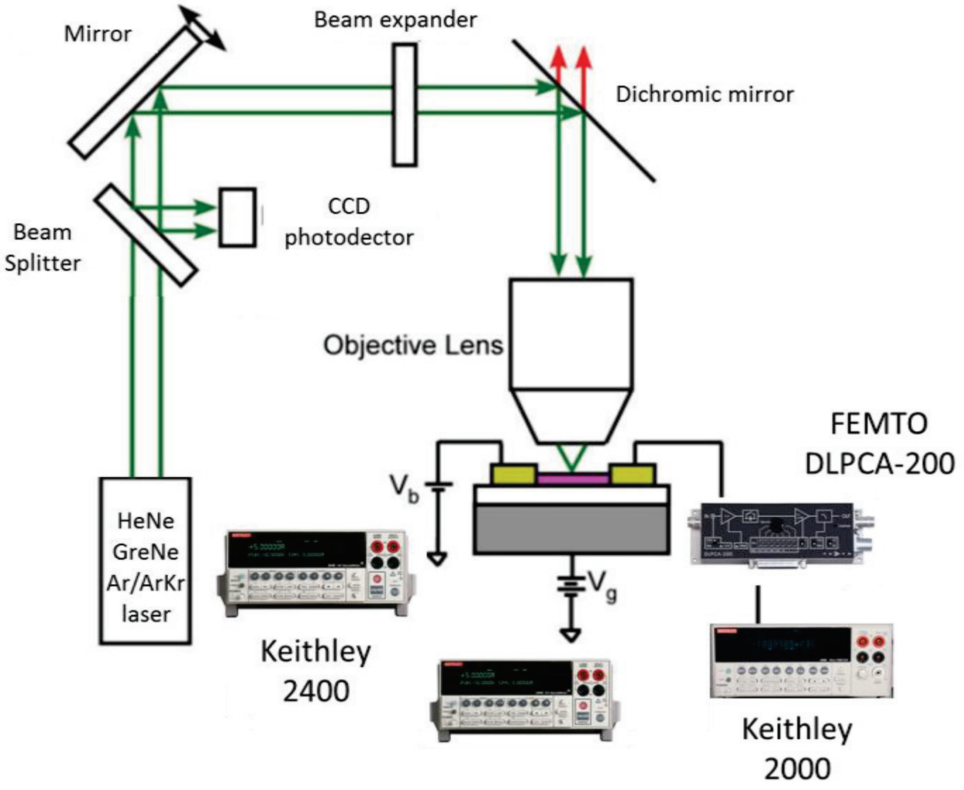

Figure 3.5. Schematic illustration of the set-up used for scanning photocurrent microscopy. The system is equipped with a HeNe (633 nm), GreNe (543 nm) and Ar/ArKr laser. A piezo-electric table is used to scan the sample through the confocal laser spot.

# Chapter 4 Chemical Modification of graphene via hyperthermal reaction*

## 4.1 Electrospray ionization

Electrospray ionization (ESI) is a powerful tool for the manipulation of molecules and chemical surface functionalization.[130,131] It has been applied, for instance, to large and fragile polar molecules that play a vital role in biological systems,[132] as well as to achieve chemical reactions on otherwise inert surfaces.[133] A major advantage of this method is that the integrated mass spectrometer enables an exceptional molecular selectivity. Electrospray ionization is a soft ionization technique that allows bringing non-volatile molecules into the gas phase with only little risk of breaking covalent bonds, and the possibility to preserve their weak non-covalent interactions.[131] It works by applying a high voltage (≈1-4 kV) to a needle, through which a small volume of the target molecule solution is forced. This creates a spray of small, highly charged droplets, which are accelerated through the instrument to a mass spectrometer, where desired molecular species can be selected according to their (charge/mass) ratio. The species are then deposited onto a substrate, with a kinetic landing energy that can be controlled via the applied acceleration voltage.

## 4.2 Modification procedure

The covalent modification of graphene through the impact of vibrationally cold, hyperthermal molecular ion collisions has been performed as follows. Fig. 4.1 illustrates the gas phase generation of a beam of intact, mono-protonated 4,4′-azobis(pyridine) (AZP) from solution using electrospray ionization. The charged species are transferred to vacuum, steered, focused and accelerated toward chemical vapor deposited (CVD) graphene on a Si-$SiO_2$ substrate. The collision energy is adjusted by the electrical bias $V_B$ applied to the substrate. Upon impact, a chemical bond is cleaved in the charged molecule, generating a reactive fragment that covalently bonds to the graphene. Most likely, the cleavage occurs at the C−N bond between the (protonated) pyridine ring and the azo-group, yielding an azopyridyl-radical, as depicted in Fig. 4.1b.

---

* Parts of this chapter are based on our publication *Chemical Modification of Graphene via Hyperthermal Molecular Reaction*[133]

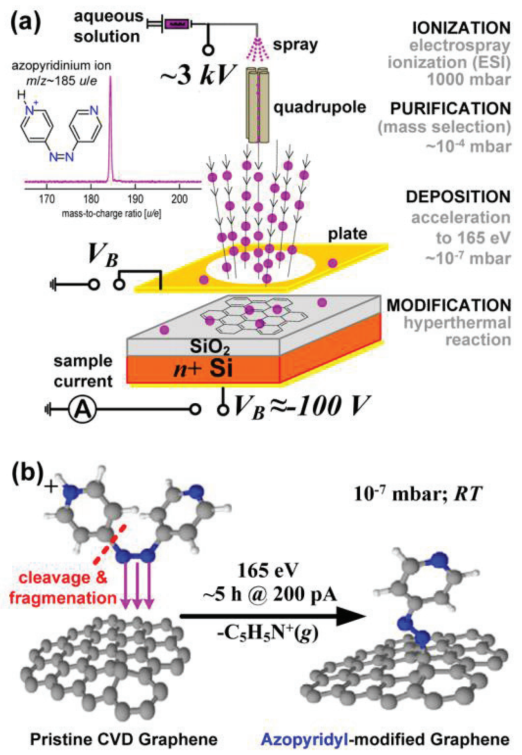

Figure 4.1. (a) Schematic depiction of the experimental setup used for graphene functionalization via hyperthermal reaction. (b) Sketch of the covalent coupling reaction yielding azopyridyl-modified graphene.

The electrospray ion beam deposition (ES-IBD) system[134,135] consists of an ambient nanospray source emitter biased to 3−4 kV, followed by a series of ion optics and differentially pumped stages. Sprays are formed from 1 mM AZP in 1:1 (v/v) $H_2O$:EtOH and 0.2% (v/v) formic acid. By time of-flight mass spectrometry (TOF-MS) (Fig. 4.1a) the formation of azopyridinium cations ($AZP^+$; m/z ≈185 $u/e$) was verified, and in combination with a mass-selecting quadrupole, a narrow mass-to-charge window specified so that the charged species is highly purified (>99.99%) before exposure. The beam arrives at the sample through a 4 mm diameter aperture at normal incidence. The primary beam energy (63 ± 3 eV, corresponding to $V_B = 0$) exiting the quadrupole is first measured by a retarding grid adjacent to the sample. During the covalent modification procedure, a deposition current is monitored at the substrate (200−330 pA) and integrated over time such that the coverage is precisely controlled. The total cation exposure was set to 1 nA over 1 h, corresponding to a dose of $\approx 2 \times 10^{14}$ $AZP^+/cm^2$, which is achieved in 3−5 hrs. Assuming a sticking coefficient of unity, this dose would approximately lead to a close-packed monolayer.

## 4.3 Characterization of modified sheets

Ex situ ambient confocal Raman scattering (blue spectrum in Fig. 4.2) reveals the characteristic G- and 2D-band of pristine, single-layer graphene before the modification.[136] The small D-peak is attributable to graphene wrinkles.[123] Upon modification with 165 ± 3 eV ions ($V_B$ = -102 V), a dominant D-peak appears, which is consistent with sp$^3$-hybridization induced disorder,[137] while the reduced 2D/G intensity ratio and the slight blue shift of the D-peak indicate the presence of disorder and/or doping.[138]

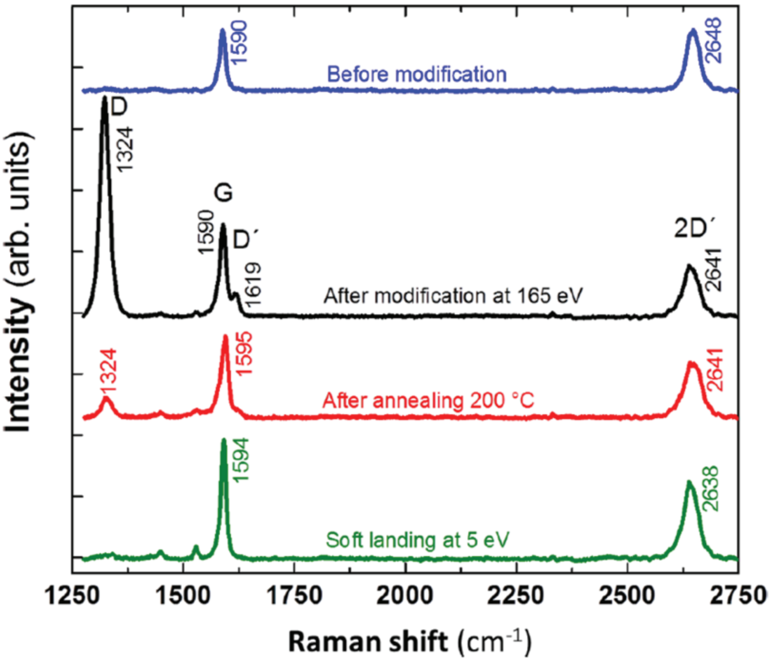

Figure 4.2. Raman spectra (recorded with λ = 633 nm) of a CVD graphene sample before and after hyperthermal functionalization with azopyridyl groups, as well as after annealing of the modified sample. The Raman spectrum of graphene subjected to soft landing is shown at the bottom for comparison.

Collisions at 5, 75, 100, and 125 eV result in the same Raman spectrum as for pristine graphene (Fig. 4.2, lowest spectrum). These deposition conditions can hence be considered as soft landing. The onset of chemisorption is observed near 165 eV, corresponding to 5.5 eV per covalent bond in the molecule, assuming center-of-mass translational kinetic energy equipartition among the internal degrees of freedom in AZP$^+$, and provided that the time-scale of the collision dynamics (on the order of picoseconds) permits particle equalization. An energy density of this order is relatively modest since in actuality it represents the upper limit of a loss-less system, yet dissipation into modes of graphene and other non-adiabatic pathways are likely. The onset energy is close to the results of molecular dynamics calculations of salt cluster collisions on inert surfaces, where 2.7 eV/particle have been found to cause fragmentation and dissipation.[139] Likewise, silver cluster collisions on platinum have been found to induce defects/chemisorption above 2.9 eV/Ag.[140] As the formation of single atom vacancies in graphene has been observed[141] after irradiation with Ar$^+$ ions of considerably higher energy (140 eV/Ar$^+$), it is plausible that the collisions are able to cause fragmentation and reactive landing of AZP$^+$ at 5.5 eV/bond.

To confirm the covalent attachment of the reactive species, the modified samples were subjected to thermal treatment. After heating in vacuum at 200°C for 1 h, Raman spectroscopy revealed a significantly reduced

D-peak intensity, signifying the desorption of chemisorbed molecules.[142] While as an alternative carbon vacancies created by the ion impact could be responsible for the pronounced D-peak, a restoration of the carbon framework of graphene would not be possible in this case, owing to the lack of a suitable carbon source and sufficiently high temperature.[143]

Raman maps displaying the D-peak intensity over an area of 100 μm$^2$, as exemplified in Fig. 4.3, show a uniform, large-area modification. Further measurements confirmed such homogeneous modification for sample areas as large as 4 mm × 4 mm. Using low neutral density filters, the D-peak area is seen to decrease in the direction of the raster scan path, resulting in sloped-maps, which likely arises from molecule desorption due to laser-induced heating.

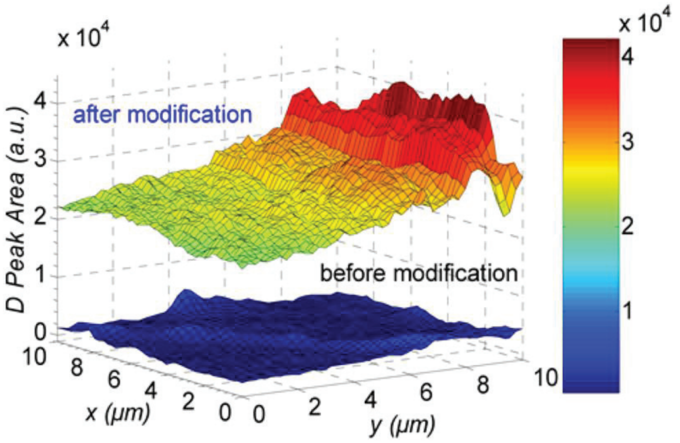

Figure 4.3. Integrated D-peak intensity area maps of a pristine and modified sample (laser excitation wavelength λ = 633 nm). Laser-induced heating causes partial desorption of the chemisorbed molecules, which results in a decreasing D-peak intensity along the scan.

From the Raman spectra, the average distance $L_D$ between the sp$^3$-defect centers (i.e., between the covalently attached azopyridyl groups) can be estimated. The intensity ratio of the D- and G-mode ($I_D/I_G$) in the spectra of the modified samples is well above 1, indicative of a high defect density regime, with $L_D$ being on the order of a few nanometers.[82] Based upon the sample-averaged value of $I_D/I_G = 2.5$, the best suited equation[82] is $L_D^2 = 5.4 \times 10^{-2} \cdot E_L^4 \cdot (I_D/I_G)$, where $E_L = 1.96$ eV is the laser excitation energy. It yields $L_D \approx 1.4$ nm, which translates into a high functionalization degree of approximately 3%, comparable to the value achievable through extensive hydrogen plasma treatment of graphene.[142] This functionalization degree corresponds to 50% of impacting ions being covalently attached to the graphene. The collision energy gives rise to competition from elastic scattering,[144] and the fragmentation efficiency is close to unity,[145] it is reasonable to attribute the remaining 50% of the collisions to elastic or dissociative projectile scattering and hence no bond formation.

Ambient tapping-mode atomic force microscopy (AFM) shows that despite the modest collision energy supplied to the surface, the pristine topographic quality of CVD graphene is still preserved after modification, as reflected by a highly smooth and flat surface. No substantial change in topography or morphology is seen over a 25 µm$^2$ area.

The elemental composition and chemical binding at the surface before and after modification was probed by X-ray photoelectron spectroscopy (XPS) using Al/K$_{\alpha1}$ photons (1486.7 eV). The C 1s peak of the pristine CVD graphene (Fig. 4.4a) has an asymmetric Doniach-Sunjic shape, characteristic of sp$^2$-hybridized C−C.[147]

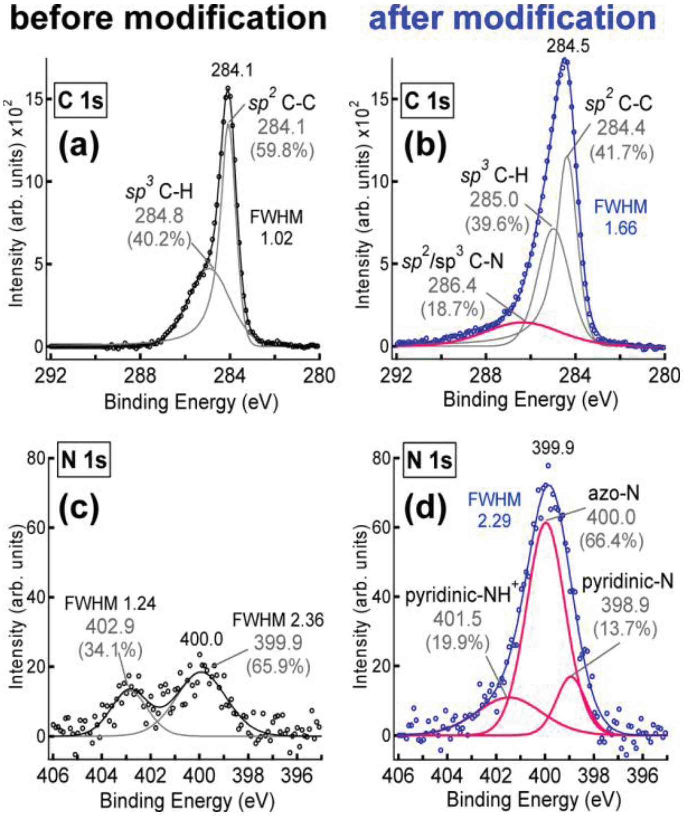

Figure 4.4. XPS spectra of pristine and hyperthermal-modified (165 eV/cation) graphene. Panels a) and b) show the C 1s peaks, while panels c) and d) display the N 1s peaks.

Upon modification, the C 1s profile broadens into a three-component envelope (Fig. 4.4b), comprising the same two peaks matching to the pristine spectrum in Fig. 4.4a, and an additional component centered at 286.4 eV, attributable to sp$^2$ C-N from the pyridyl-group and sp$^3$ C−N from the azo linkage to graphene.[148]

Compared to the pristine control (Fig. 4.4c), the modified sample (Fig. 4.4d) shows a significantly higher N 1s signal centered at 399.8 eV. The increased N/C ratio is consistent with the deposition of the nitrogen rich AZP or one of its fragments. The very broad N 1s peak with a FWHM of 2.3 eV signifies the presence of multiple types of nitrogen atoms. It can be deconvoluted into a pyridine-like nitrogen (389.9 eV), an azo-nitrogen (400.0 eV) and a protonated pyridine nitrogen (401.6 eV) signal.[148,149] These binding energies agree well with a previous XPS study of 2,2′-azopyridine,[149] reporting a FWHM of 2.7 eV and deconvoluted positions of 389.9 eV for the two nitrogen-pyridinic atoms, and 400.1 eV for the two azo-nitrogens.

For the relative abundance of azo-nitrogen to the combined neutral and protonated pyridinic-nitrogen a ratio of 2:1 is found based upon the component areas shown in Fig. 4.4d. This ratio points toward a binding mechanism wherein the diimide group cleaves preferentially at the protonated pyridyl-site ($C_5H_4NH$)-N=N-($C_5H_4NH^+$) of the $AZP^+$ ion beam, producing a neutral azopyridyl-radical (·N=N−$C_5H_4N$) that binds to graphene through a C-N covalent bond, as illustrated in Fig. 4.1b. The other part, a pyridinium-radical, will rearrange and leave as gaseous protonated pyridine. The XPS data indicate that 60% of the pyridine groups are protonated, which most likely occurs after sample exposure to the ambient rather than originating from the protonated ion beam itself.

Modeling other mechanisms to the nitrogen XPS data resulted in only poor agreement. Should the cleavage have occurred at the non-protonated pyridyl-site of the $AZP^+$ ion beam, the resultant azopyridinium- and pyridyl-radicals could both graft covalently to graphene (yielding a relative abundance of azo to pyridinic nitrogen in the ratio 1:1), or the azopyridinium-radical could rearrange, leaving as gaseous 4-diazenylpyridine, and only the pyridyl-radical would bind (resulting in only pyridinic-nitrogen). However, none of these scenarios are consistent with the intensities of the components in the N 1s peak (Fig. 4.4d). At the same time, symmetric, azo-initiator-type splitting with nitrogen elimination and concomitant formation of two pyridyl-radicals can also be excluded, as these would not give rise to the azo-nitrogen observed.

The above observations strongly favor covalent linkage of azopyridyl-moieties to the graphene. The hyperthermal activation, however, is a statistical process as well, which can overcome even a high activation barrier. Thus, within the margin of error of the fits, also other less likely reactions may have occurred in parallel.

Hyperthermal ion chemistry presents a unique solution to the challenge of controllably producing dense and ordered monolayers on graphene. Electrospray ionization accommodates both an enormous mass range (1 - $10^6$ Da) and a wide choice of reagents to activate non-equilibrium hyperthermal reactions of graphene that would otherwise remain kinetically unfavorable. High vacuum deposition further minimizes the influence of an electrochemical water/oxygen redox couple at the $SiO_2$ substrate, which is responsible for hysteretic device behavior under ambient.[150]

## 4.4 Electrical measurements

The hyperthermal protocol was further investigated as a possible means to open a band gap in graphene, in order to increase the electrical on/off ratio of pristine graphene, which is only ≈5 at room temperature.[22] Fig. 4.5 depicts the transfer curves of graphene before (inset, green curve) and after the azopyridine modification (blue curve). It is evident that the position of the resistance maximum shifts and also the on/off ratio changes due to the modification.

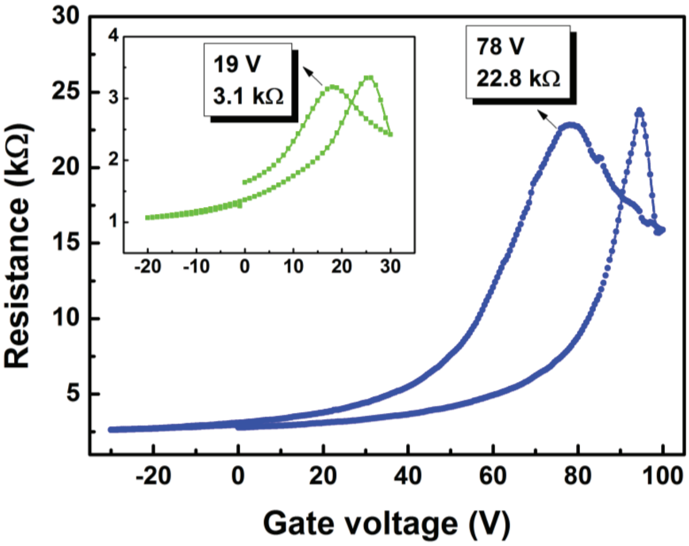

Figure 4.5. Characteristic transfer curves measured at room temperature with a two probe set up; before (inset) and after the hyperthermal modification (165 eV/cation).

The shift of the resistance maximum to more positive gate voltages is indicative of p-type doping. This doping reflects an electron-withdrawing character of the attached nitrogen atoms. After the modification, there is transfer of electrons from the graphene to the nitrogen, causing a well-documented graphene hole doping.[151] The resistance increase by approximately one order of magnitude, as compared to the pristine graphene, indicates the presence of (resonant) scattering centers, most likely the $sp^3$ carbons in the covalently functionalized graphene.[152]

## 4.5 Patterned modification

As only a small increase of the on/off ratio could be achieved by chemical modification of laterally extended graphene, we combined the modification with lateral patterning of the graphene. To this end, the hyperthermal reaction was applied to graphene sheets covered by a PMMA layer containing a narrow window. In this manner, modified graphene stripes with a width of about 1 µm were obtained within an unaltered graphene sheet. The major aim was to provide the stripe with a local top gate, in order to implement an efficient graphene-based field-effect transistor, as proposed theoretically by Fiori *et al.*[153]

The Raman spectrum of a representative graphene stripe (1P-Gr), chemically modified with $AZP^+$ (Fig. 4.6), features emergent D- and D′-peaks at 1326 $cm^{-1}$ and 1613 $cm^{-1}$, respectively. These two peaks arise from the introduced $sp^3$ carbons, as described above. There are also additional peaks between 1326 and 1586 $cm^{-1}$, matching with Raman peaks of PMMA (as determined using control samples), indicating that residues of this polymer remain on the surface after the modification. A Raman map displaying the D-peak intensity of a graphene sheet comprising two modified stripes (each 1 μm wide) is shown in the inset of Fig. 4.4. The stripe-like features displaying a higher D-peak intensity fit well to the patterned length and width.

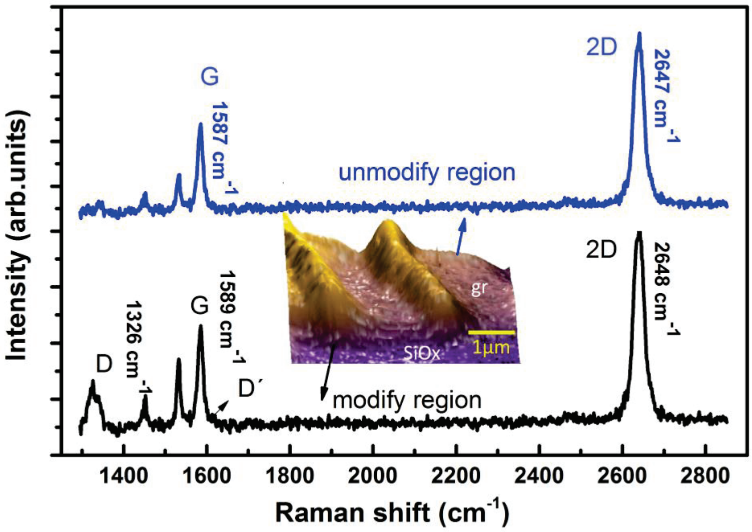

Figure 4.6. Raman spectrum (λ = 633 nm) of the unmodified area (blue spectrum) and the chemically modified (black spectrum) stripe within a graphene sheet. The inset is a D-peak map of the monolayer.

AFM images (Fig. 4.7a) display some residues on top of the modified graphene, in agreement with the Raman spectra exhibiting peaks between 1326 cm$^{-1}$ and 1586 cm$^{-1}$ that belong to PMMA. The AFM height of the modified stripes exceeds that of pristine graphene by approximately 1 nm. The transfer curve, recorded with a back gate, shows only little doping, along with a slight increase of the on/off ratio in comparison to pristine graphene (Fig. 4.7b). That the modification caused only a small change in the electrical behavior can be explained by the low accessibility of the ESI molecular beam to the graphene, due to shielding by the narrow PMMA window.

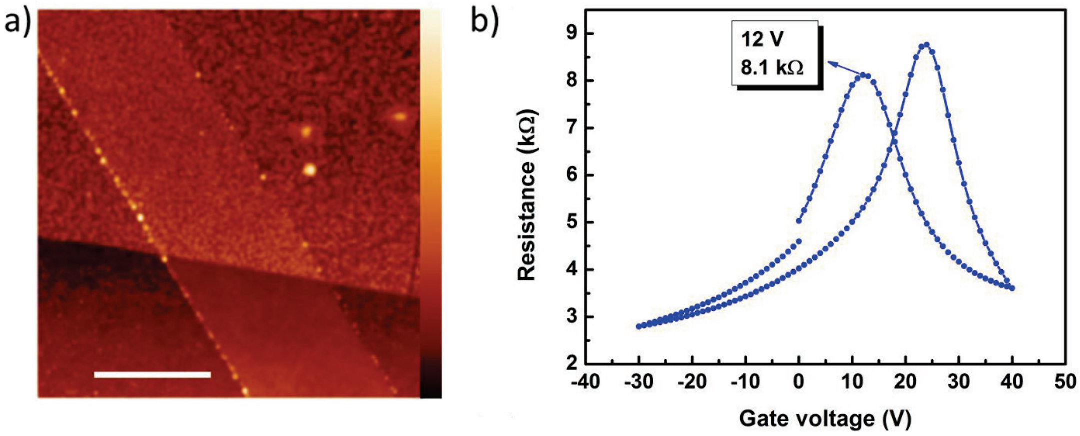

Figure 4.7. a) AFM image of a chemically modified graphene stripe. The scale bar is 1 μm, while the color scale ranges from 0 to 16 nm height. b) Two-probe measurement of resistance versus gate voltage, measured across one of the stripes in the chemically modified graphene sheet.

The above results demonstrate that hyperthermal molecular ion beams of azopyridine enable the controlled covalent functionalization of CVD graphene. Since the kinetic energy of the impinging species of 165 eV/ion is significantly larger than typical covalent bond-dissociation depths ($1 \leq D_0 \leq 10$ eV/bond), the excess energy breaks chemical bonds, and overcomes the costly activation barrier ($E_A$) that usually prohibits covalent linkage to the basal plane of graphene.[154,155] Raman scattering in combination with XPS confirms the covalent attachment of azopyridyl-groups, with a high functionalization degree of 3%, while AFM imaging testifies that the modified graphene retains its topographic integrity.

# Chapter 5 Chemical Modification of graphene by $OsO_4$ from vapor phase

## 5.1 Symmetric dihydroxylation of alkenes

The oxidation of alkenes is important in organic synthesis as a precursor of functional groups such as ketones, aldehydes and carboxylic acids, which are intermediates in the synthesis of various drugs and catalysts.[156] Particularly useful is the cis-hydroxylation of alkenes by osmium tetraoxide ($OsO_4$) due to its stereo-specificity yielding diols via a syn-addition.[157] The corresponding reaction mechanism is outlined in Fig. 5.1. It involves the formation of an osmium (VI) intermediate, whose hydrolysis affords the corresponding cis-diol.[158] Osmylation is feasible also with aromatic hydrocarbons, where the attack occurs at the sites of highest electron density.[159] This is relevant because graphene, in terms of chemical reactivity, behaves similarly to larger aromatic systems. In a pioneering experiment, $OsO_4$ has been successfully used by Cui *et al.* to oxidize single-walled carbon nanotubes.[160]

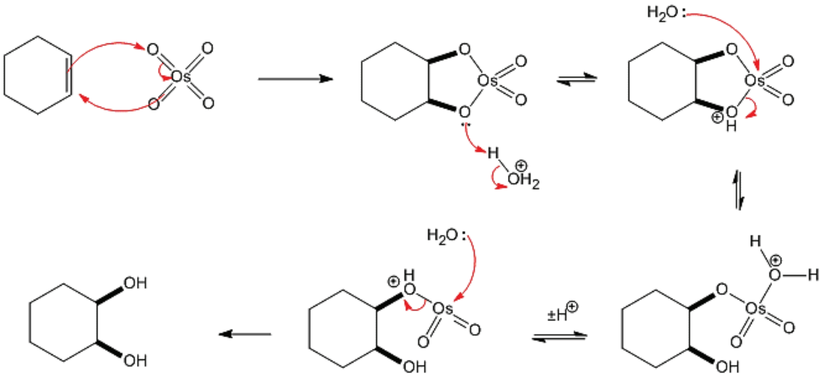

Figure 5.1. Reaction mechanism of the symmetric dihydroxylation of alkenes by $OsO_4$. The intermediate osmium (VI) ring-like structure is hydrolyzed by water.

While several oxidation methods have been applied to graphene, as described in section 2.2.2, all of them yield a mixture of different, oxygen-containing functional groups e.g. ketones, aldehydes and carboxylic acids. The absence of chemical selectivity renders the properties of the resulting graphene oxide difficult to control. As a consequence, graphene oxide samples prepared in different labs generally bear different types and densities of functional groups. In this context, osmylation by $OsO_4$ promises access to an alternative type of graphene oxide, wherein only one type of functional group (hydroxyl groups) is attached to exclusively one side of the sheet.

## 5.2 Modification procedure

A Si-$SiO_2$ substrate with mechanically exfoliated graphene was placed in the middle of a quartz tube with a small crystal of $OsO_4$ (Sigma Aldrich, >99.9% purity) located 10 cm upstream (Fig. 5.1). The tube was first purged with argon and the filled with 0.6 bar of oxygen (Fig. 5.2). After 30 min of equilibration, the sample was then irradiated with 254 nm UV light for 50 min. Subsequently, the sample was rinsed with water and isopropanol and finally blow dry with argon.

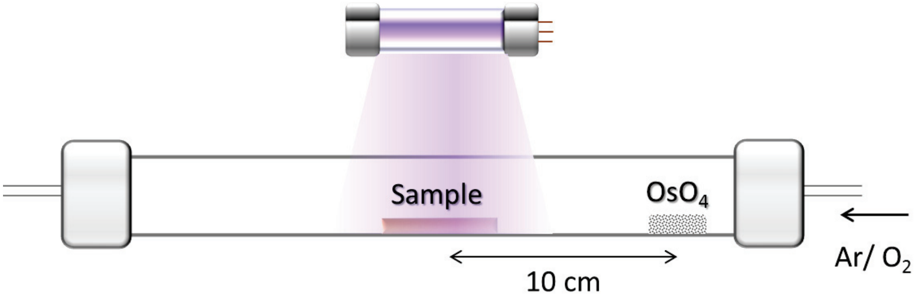

Figure 5.2. Schematic depiction of the home-made UV reactor used to chemically modify graphene by $OsO_4$ vapor at room temperature. The UV lamp emits a wavelength of 254 nm.

Patterned functionalization of 1 µm wide stripes was performed by first depositing a PMMA layer onto the substrate covered by graphene. Using e-beam lithography, 1 µm wide windows were then defined within the PMMA layer. The same modification procedure as explained above was then carried out, followed by removing the PMMA with acetone.

## 5.3 Sample characterization

After each modification experiment, the optical appearance of the graphene served as a first test whether the reaction was successful. In general, the more groups are covalently attached to graphene, the more transparent it becomes, because the functionalization reduces the density of π-states, as explained in section 2.1.2 and reported by Jeremy *et al.*[161] Importantly, full transparency is obtained only for high coverage.[68] The change of optical contrast under the microscope is exemplified in Fig. 5.3 for two neighboring, 1 µm wide stripes within the same graphene monolayer. The formation of such highly transparent regions could not be observed in case of the $AZP^+$ functionalization (see chapter 4), evidencing that the functionalization degree achievable with $OsO_4$ is significantly higher than for the hyperthermal approach.

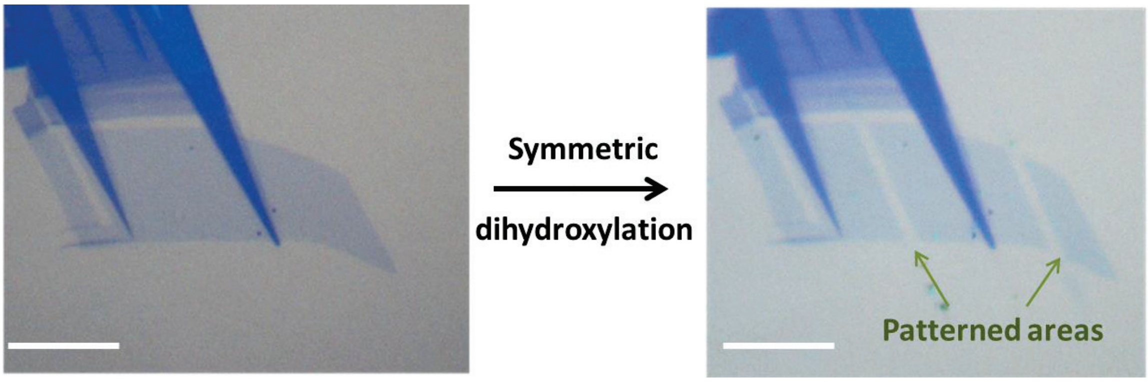

Figure 5.3. Optical micrograph showing two 1 µm wide stripes patterned into the same graphene monolayer by reaction with $OsO_4$. The white scale bars are 5 µm.

The AFM height profile in Fig. 5.4 reveals that the chemical modified, 1 µm wide stripe has a height of approximately 1 nm. As the sample was rinsed several times to remove adsorbates, the thickness increase can be attributed to graphene oxide formation. In contrast to the hyperthermal method (see chapter 4), the roughness of the unmodified graphene area is similar to that of pristine graphene, reflecting a cleaner process. It follows that the ESI method promotes cross-linking of the PMMA, whereas the ozone generated by the UV irradiation during the $OsO_4$ reaction is able to remove PMMA residues.[162]

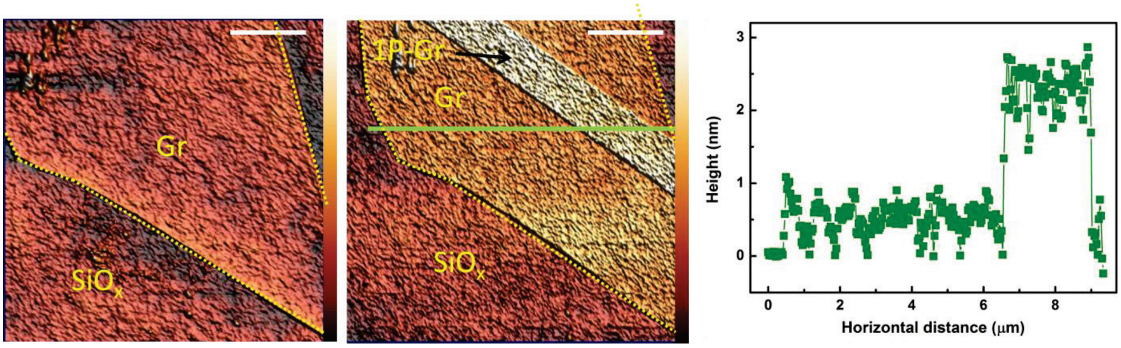

Figure 5.4. (Left) Topographic AFM images before and after formation of 1 µm wide graphene stripe by covalent functionalization using $OsO_4$. (Right) Cross-sectional profile along the green line in the right AFM image. The white scale bar is 2 µm and the color scale ranges from 0 to 5 nm height.

The covalent oxidation of graphene by $OsO_4$ could be further confirmed by Raman spectroscopy. The spectrum in Fig. 5.5 evidences the appearance of the D and D′ peak at 1324 $cm^{-1}$ and 1623 $cm^{-1}$ respectively, in the stripe area, consistent with the presence of $sp^3$ carbons or defect-induced disorder.[137] According to Eckmann *et al.*[84] the D peak position is only sensitive to the amount of disorder, whereas the D′ peak position strongly depends on the type of defect introduced into the lattice. They reported that for hydrogen modification of graphene, an $I_D/I_G$ ratio of 0.33 can be attributed to exclusive $sp^3$ carbon modification without vacancies (the ratio for vacancies is 0.82). The ratio of 0.50 obtained for the present samples can be assigned to a mixture of $sp^3$ carbons and vacancies, with the former being predominant. Raman maps displaying the D peak intensity across the graphene monolayer provide direct evidence for the modified stripe (Fig. 5.5, right panel). The visible feature corresponds well to the 1 μm stripe created by the UV-$OsO_4$ through the patterned PMMA mask. In contrast to the $AZP^+$ method, no PMMA peaks are observed, highlighting the intrinsic "cleaning capability" of the $OsO_4$ method.

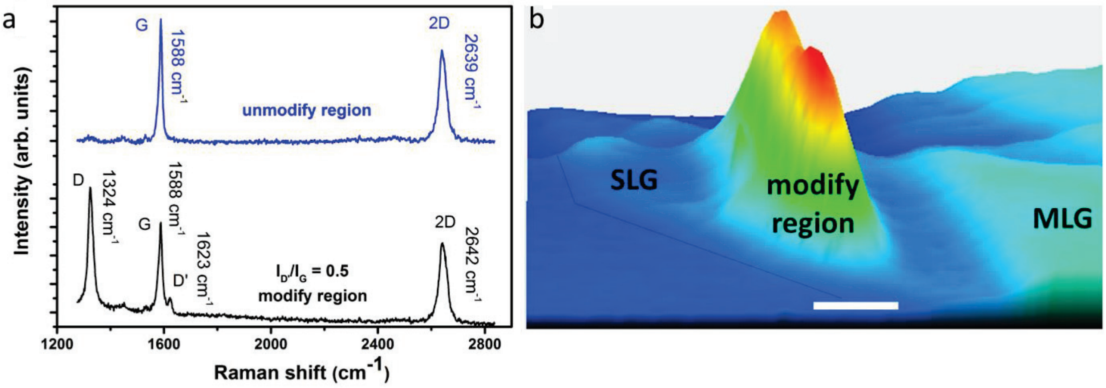

Figure 5.5. a) Raman spectra of the un-modified (blue spectrum) and the modified stripe (black spectrum) area. b) D-peak intensity map of the graphene monolayer. The scale bar is 1 μm.

From the Raman spectra, the average distance $L_D$ between the $sp^3$-defect centers was determined in the same manner as described in chapter 4. The intensity ratio of the D and G modes ($I_D/I_G$) are above 1 in the spectra of the modified samples, indicative of a high defect density regime, with $L_D$ being on the order of a few nanometers.[82] Based upon the value of $I_D/I_G = 1.9$, averaged over several stripes, the equation[82] $L_D^2 = 5.4 \times 10^{-2} \cdot E_L^4 \cdot (I_D/I_G)$, where $E_L = 1.96$ eV is the laser excitation energy, yields $L_D \approx 1.2$ nm. This translates into a functionalization degree of approximately 2.6%, similar to the value achieved in case of modifying an extended CVD graphene sheet by the ESI method.

## 5.4 Electrical characterization

To further confirm the chemical modification, as well as test the suitability of the devices as an FET, two-probe electrical measurements were performed. The resistance of the completely modified graphene monolayer in Fig. 5.6a reaches a sizable value of ≈350 kΩ, while the 1 μm modified graphene stripe displays only a four-fold resistance increase compared to the pristine sample (≈4 kΩ).[21] This difference supports that the functionalization degree of the stripe is smaller due to the limited access of the $OsO_4$. In both cases, pronounced p-doping is observed, similar to previous reports on graphene oxidation.[152]

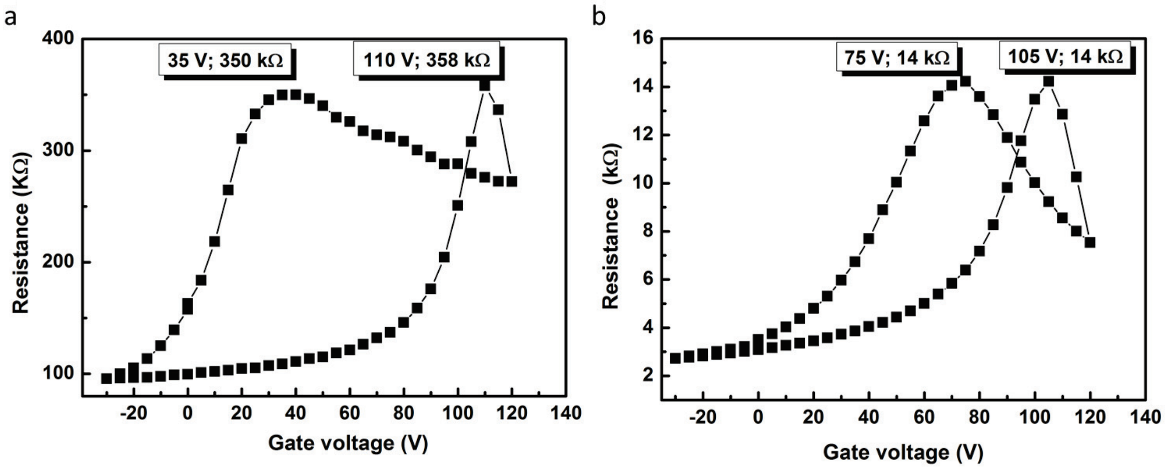

Figure 5.6. Two probe measurements of resistance versus gate voltage for a) completely modified graphene flake and b) 1PGr.

The charge transport properties were evaluated in more detail by temperature dependent resistance measurements (Fig. 5.7). Upon cooling, the "off state" resistance of the chemically modified sample monotonously increases, while the "on resistance" remains almost constant (Fig. 5.7a,b). The maximum on/off ratio of ≈550 is significantly higher than previously reported for graphene partially modified with flourine[163] or hydrogen.[65] As apparent from Fig. 5.7a, the Dirac point shifts toward zero gate voltage upon cooling, accompanied by a resistance increase of almost 3 orders of magnitude. This behavior points towards two-dimensional hopping as relevant charge transport mechanism.[164] The latter involves consecutive inelastic tunneling between localized states, and has also been observed for different types of graphene modifications.[65,152,163] Its temperature dependence is given by $R \propto \exp^{(T_0/T)^{1/3}}$, to which the present data can be well fitted (see Fig. 5.7c).[164] The fitting parameter, which is proportional to the density of localized states at the Fermi level and the localization length, is extracted to $T_0$ = 2248 K.[152,163] This value exceeds that reported for hydrogenated graphene, and is comparable to that for fully fluorinated graphene.[65,163]

For comparison, it was attempted to fit the data to the thermal activation exponential law (Fig 5.7d): $R = R_0 \exp^{(\Delta E/2K_bT)}$, where $R_0$ is an pre-exponential factor, $\Delta E$ is the energy gap and $k_b$ is Boltzmann constant. The low quality of the data fit further supports the hopping mechanism. Moreover, we ascribe the small gap obtained ($\Delta E = 9$ meV) to the gap between the trap state.[163]

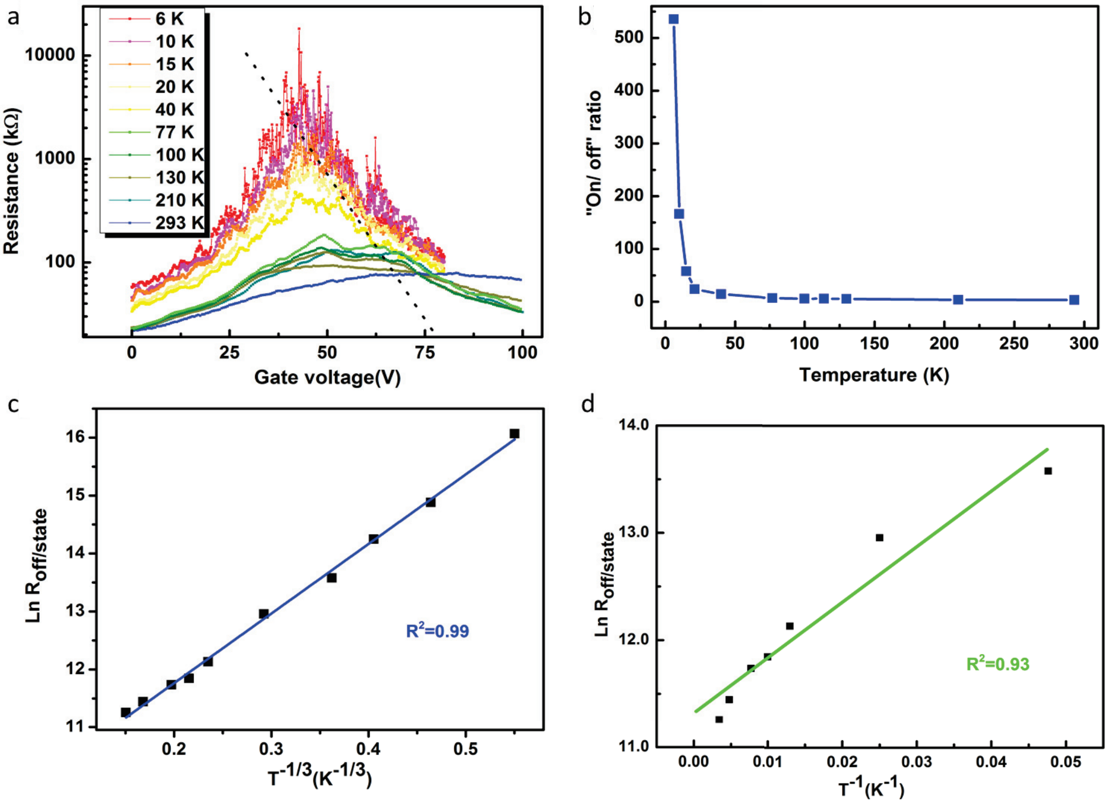

Figure 5.7. Charge transport properties of graphene covalently modified with $OsO_4$. a) Transfer curves in dependence of temperature. b) Exponential increase of the on/off ratio with decreasing temperature. c) Fitting according to the two-dimensional hopping transport mechanism. d) Arrhenius type of fit of the experimental data at low temperature.

The carrier mobility extracted from the transfer curves (Fig. 5.8) increases by almost two orders of magnitude from room temperature ($7.43 \cdot 10^{10}$ $V^{-1}cm^{-2}$) to 6 K ($2.12 \cdot 10^{13}$ $V^{-1}cm^{-2}$). This change can be explained by the “freezing” of trap states at low temperatures.[165,166]

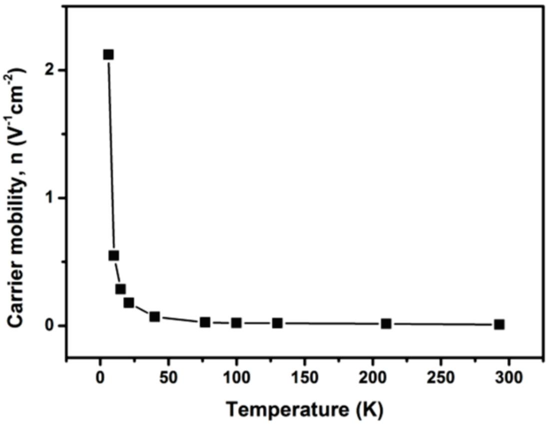

Figure 5.8. Temperature dependence of carrier mobility of graphene chemically modified with $OsO_4$. The measurement was done using a two probes set up.

# Chapter 6 Graphene-insulator-metal Diodes*

## 6.1 MIM diodes and their application as photodiodes

### 6.1.1 Basics of MIM Diodes

The ideal diode is a discrete component that allows current flow between its terminals in a particular direction (0 resistances), while the blocks it in the opposite direction (infinite resistance). There are several types of diodes, most prominently pn diodes, Schottky Diodes, pn-p diodes, and Zener diodes. The special case of the metal-insulator-metal (MIM) diode is composed of a thin insulator layer in between two metal electrodes. Its operation mechanism involves tunneling of charge carriers through the barrier and/or carriers overcoming the barrier due to thermal activation, the relative importance of which depends on the barrier heights, insulator thickness, and temperature. Tunneling becomes more significant the smaller the thickness of the oxide barrier becomes. In a normal MIM diode, electrons from metal 1 (M1) can tunnel into metal 2 (M2) when the insulator layer is several nanometers thick (less than ≈10 nm) and vice versa electrons from M2 can tunnel into M1 (further description will be given in section 6.3).[167] Electron tunneling from M1 to M2 causes a positive current from M2 to M1, and vice versa (see for further details section 6.4). The corresponding current densities can be calculated as follows:

$$J_{2\rightarrow 1} = \frac{4\pi m_2 q}{h^3}\int_0^\infty T(E_x)\left[\int_{E_x}^\infty f_2(E)dE\right]dE_x \qquad (6.1)$$

$$J_{1\rightarrow 2} = \frac{4\pi m_1 q}{h^3}\int_0^\infty T(E_x)\left[\int_{E_x}^\infty f_1(E)dE\right]dE_x \qquad (6.2)$$

Good MIM diode performance requires a high asymmetry ($f_{ASYM} = I_{forward}/I_{reverse}$), strong nonlinearity ($f_{NL} = (dI/dV)/(I/V)$), large responsivity ($f_{RES} = (d^2I/d^2V)/(dI/dV)$), as well as a low resistance or a high on-current.[168,169] These figures of merit are mainly determined by the work function difference of the electrodes, and the barrier height between the insulator and the electrode materials.[170–173] In the design of MIM diodes, a

---

[*] Parts of this chapter are based on our publications *High Performance Graphene–Oxide–Metal Diode through Bias-Induced Barrier Height Modulation* [226] and *Hot-carrier extraction from multilayer graphene* accepted in Nano Letters

trade-off between these parameters is needed. For instance, a high asymmetry requires both, a large work function difference between the two electrodes and a large barrier height, but a too high barrier decreases the on-current or increases the resistance of the device.[170,171] Among the various investigated metal-(multi)insulator-metal configurations, the best overall performance has been attained for Nb-$Nb_2O_5$-Pt diodes, featuring an asymmetry of 7800 and a nonlinearity of 4.7 at 0.5 V. [169,174–176]

As an alternative to using two metal electrodes in such diodes, one or both of them can be replaced by graphene, a two-dimensional semimetal whose excellent, tunable electrical properties render it into a valuable component of vertical devices such as barristors[177] and field-effect tunneling transistors.[178] In these three-terminal devices, the work function of graphene can be tuned over a span of hundreds of meV via an external gate electrode, whereby the height of the vertical transport barrier is modulated.[178–185] Graphene-based barristors and similar devices,[179–185] commonly rely upon modulation of the graphene-semiconductor junction, which limits the device operation speed. To date, only very few studies have been performed on graphene-insulator-metal (GrIM) devices, comprising hexagonal boronitride (hBN) nitride or molybdenum disulfide ($MoS_2$) as vertical transport barrier.[178,186] Owing to the low transit time of the tunneling electrons, such devices are expected to operate over a much wider frequency range than the graphene-semiconductor junction. In general, MIM diodes are promising for application as rectennas for solar energy harvesting,[168,169] photodetectors[187–190] and high frequency mixers.[191]

## 6.1.2 MIM Diodes for photodetection and light harvesting

Quantum mechanical tunneling is an ultrafast process that occurs on the order of femtoseconds, rendering MIM diodes useful high frequency applications, including fast photodetectors. In fact, it has been shown that detectors with band widths of several THz can be created using MIM diodes.[192] The ultrafast characteristic of a MIM diode ensures that the carriers are able to respond faster than the oscillation period of the electromagnetic field. This property opens access to optoelectronic devices with enhanced responsivity, such as photo-detectors based on surface plasmon resonance (SPR), or devices exploiting hot carrier extraction from semi-metallic materials (section 6.4). SPR enhancement can occur in MIM diodes comprising a sufficiently thin insulator, such that the electromagnetic field of the metal plasmon is able to increase the tunneling current. This enhancement has been demonstrated to render MIM devices into efficient photodetectors, solar cells as well as sensing devices.[193,194] Recent examples of MIM-based photodetectors and light harvesting devices are shown in Fig. 6.1. Specifically, Fuming *et al.*[195] have found efficiencies on the order of 1% for a planar Au-$Al_2O_3$-Au device (Fig. 6.1a). Following the same principle, Hamidreza *et al.*[188] investigated a device version where one of the electrodes is an Au nanorod (Fig. 6.1b), thereby reaching a photoresponsivity of 250 nA/W. Based upon a similar nanostructuring strategy, Gadalla *et al.*[187] fabricated gold nanogap devices (Fig. 6.1c) with a responsivity as high as 4 A/W. A different approach was pursued by Thacker and co-workers[190] who realized a planar configuration with various types of oxides as insulator (Fig.

6.1d). In these devices, the insulators ZnO and NiO enabled high-frequency rectification with a power transfer efficiency at 1 THz of 49% and 34%, respectively.

In the present thesis, graphene has been implemented as one electrode of a MIM diode configuration, resulting in graphene-insulator-metal (GrIM) diodes, whose electrical performance was studied in detail both in the dark and under light illumination.

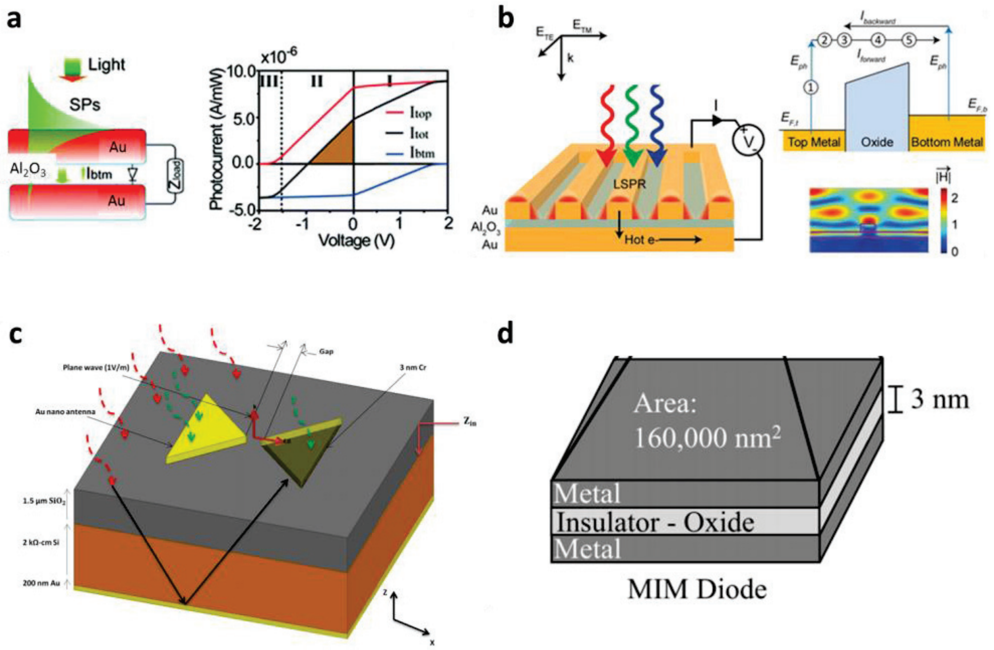

Figure 6.1. Examples of recently studied MIM diodes for optoelectronic applications. a) Au-$Al_2O_3$-Au device designed in a planar configuration for light-to-energy conversion. b) Light harvesting by nanostructured gold nanorods on an Au-$Al_2O_3$ substrate. c) Gold nanogap devices fabricated on $SiO_2$, in order to study plasmon enhancement effects. d) A MIM in a planar configuration comprising different types of oxides. The images are adapted from references 187,188,190,195.

## 6.2 Gr-$TiO_x$-Ti diode fabrication

The graphene bottom electrode was mechanically exfoliated from highly oriented pyrolytic graphite (HOPG) onto Si substrates coated with a 300 nm thick layer of $SiO_x$. The Ti-Au contact was then defined by standard e-beam lithography followed by thermal evaporation of the metals. Subsequently, 6 nm of $TiO_x$ was deposited by three cycles of thermal evaporation of ≈2 nm Ti, with a subsequent oxidation step after each cycle under ambient. Finally, 20 nm thick Ti metal top electrodes were fabricated on top of the $TiO_x$ insulator layer via e-beam lithography. All I-V characteristics were recorded under ambient with the configurations shown in Fig. 6.2. The SPCM measurements were performed under ambient conditions at zero source-drain bias with the aid of a confocal laser microscope. The temperature dependent photocurrent measurements were carried out in a cryostat THMS600 (Linkam) using a green laser ($\lambda$ = 514 nm).

The inverse device configuration required for doping the graphene was implemented by first evaporating 20 nm of Ti, followed by 6 nm $TiO_x$ and then transferring graphene chemical vapor deposited (CVD) on top of the oxide-coated Ti electrode. P-type doping of graphene was achieved by thermally evaporating F4-TCNQ at a rate of 0.1 Å/s on top of it. The thickness of the F4-TCNQ layer was adjusted by the number of evaporation steps (2 nm per step).

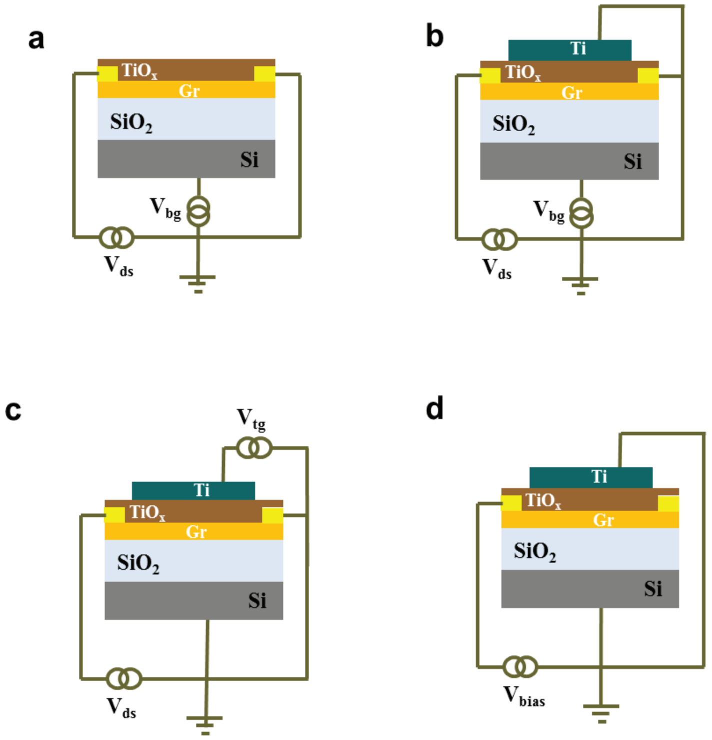

Figure 6.2 a,b) Schematic representation of the device configurations used for determining the electrical resistance of the graphene channel as a function of back gate voltage a) before and b) after deposition of the Ti electrode. c) Configuration used for measuring the graphene channel resistance in dependence of the Ti top gate voltage. d) Configuration used for recording the I-V characteristics of the Gr-$TiO_x$-Ti diodes.

## 6.3 Dark electrical behavior of Gr-$TiO_x$-Ti diodes

As mentioned above, an alternative to using two metal electrodes in MIM diodes is to replace one or both of them by graphene. In the following, it is demonstrated that in two-terminal Gr-$TiO_x$-Ti (GrIM) diodes, which lack an external gate as third terminal, barrier height modulation can occur solely based upon the applied bias, which leads to excellent device performance down to the smallest insulator thickness. This task requires a suitable choice of insulator in order to allow for sizable electron transport between the graphene and the metal. Moreover, our data reveal the importance of balancing the tunneling and thermionic contributions to the charge transport.

The work functions of graphene and Ti are 4.5[196] and 4.2 eV[93], respectively. Titanium thus fulfills the above mentioned requirement that the work function of the metal contact (M2) is smaller than that of graphene. The electron affinity of $TiO_2$ is ≈4.0 eV [197,198], which ensures the trapezoid shape of the tunneling barrier depicted in Fig. 6.3a The Dirac point shift of the graphene channel from +5 to -40 V after deposition of the Ti top electrode (in the appendix A, the transfer curves are shown) indicates appreciable n-type doping by the Ti layer. We furthermore determined the work function difference between Ti and graphene by Kelvin force microscopy, as illustrated in Fig. 6.3b. The detected potential difference of ≈200 meV is in reasonable agreement with the expected value of 0.3 eV. The somewhat smaller experimental value can be explained by the n-type doping of the graphene by the Ti.

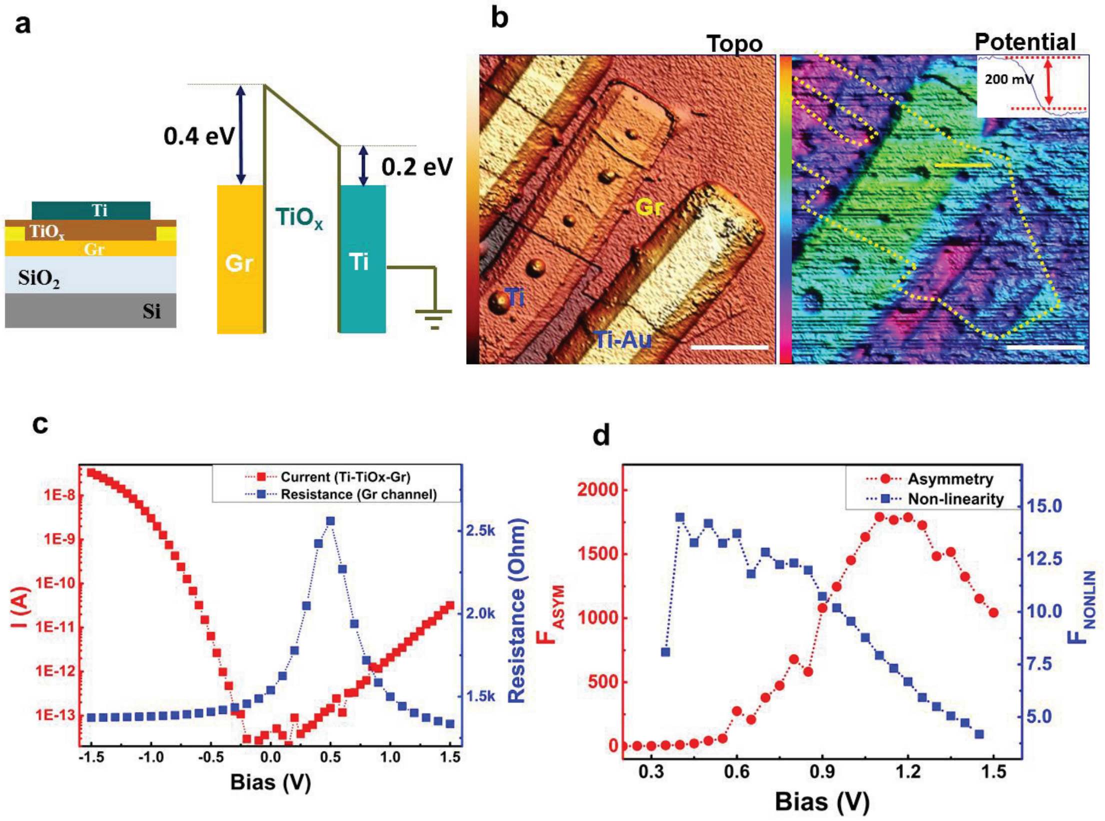

Figure 6.3. a) Schematic representation of the Gr-$TiO_x$-Ti diode structure (cross-section) and the corresponding band alignment. b) Topographic AFM (left), and surface potential image (right) of the GrIM diode. The profile along the red line in the surface potential map is shown in the inset. The dashed yellow line in the potential map marks the graphene sheet. The color code is 0 to 100 nm and -300 to 600 meV in the topology and potential image, respectively. The scale bar is 2 µm. Electrical performance of the Gr-$TiO_x$-Ti diode with a four layer-thick graphene sheet. c) Semilogarithmic I-V curves (red squares), obtained for current flowing from graphene to Ti electrode under a bias applied between graphene and Ti electrode, and resistance change of graphene channel as a function of bias applied between graphene and the Ti electrode (blue squares). In this measurement, a small bias of 0.01 V is applied to the graphene channel. d) Asymmetry (red circles) and non-linearity (blue squares) plotted against applied bias.

The I-V characteristics of a Gr-$TiO_x$-Ti diode (red curve in Fig. 6.3c), acquired between the four layer-thick graphene sheet and the Ti electrode, displays a diode-like behavior with a high current under negative bias and a low current under positive bias. Moreover, the graphene channel resistance measured as a function of bias applied to the Ti electrode (blue curve in Fig. 6.3c) signifies a change of graphene's work function. The plot in Fig. 6.3d reveals a maximum asymmetry of 1800 at 1.2 V (red curve) and a corresponding nonlinearity of 7. The decrease of the asymmetry at higher bias is attributable to the rate of the Fermi level shift being dependent on the applied bias. Specifically, when the Fermi level is near the Dirac point, this rate is high due to the low density of states. By comparison, when the Fermi level moves away from the Dirac point, this rate decreases, such that the forward current saturates while the reverse current increases. An additional contribution to the saturation behavior may arise from trap states within the $TiO_x$ layer, as discussed below.

The observed device behavior is explainable by a mechanism whose key feature is the modulation of graphene's work function intrinsically by the applied source-drain bias. Thus imparted change of the transport barrier height enables "synchronizing" the tunneling and thermal emission currents. This result in a fundamentally different device operation mechanism in comparison to MIM diodes, as schematically illustrated in Fig. 6.4. In the MIM diode (Fig. 6.4a), transport occurs via thermionic emission (dark-cyan arrows) and tunneling (red arrows). The difference between the metal work functions leads to a trapezoidal potential barrier at zero bias. When a positive bias V is applied, the barrier height for the thermionic current is reduced to $\Phi_1$-eV for a small bias, and reaches a minimum value of $\Phi_2$ for a high bias. In the negative bias regime, the barrier height for the thermionic current is $\Phi_1$, independent of the magnitude of the bias. Therefore, the thermal current is forward when a positive bias is applied to M1.[170,171] With respect to the tunneling current, it is relevant that the slope of trapezoid potential decreases upon application of a positive bias, but increases when a negative bias is applied. Accordingly, the tunneling current is forward when a negative bias is applied to M1.[170,171] The asymmetry of the MIM diode is strongly dependent on the dominant transport mechanism and the (oxide) insulator layer thickness. It assumes a high value ($\approx \exp((\Phi_1 - \Phi_2)/k_B T)$) when the thermionic current is dominant and the oxide layer thickness is above 10 nm.[174] Conversely, it is quite small (below 100) when tunneling is dominant and the oxide layer is thinner than 5 nm.[174]

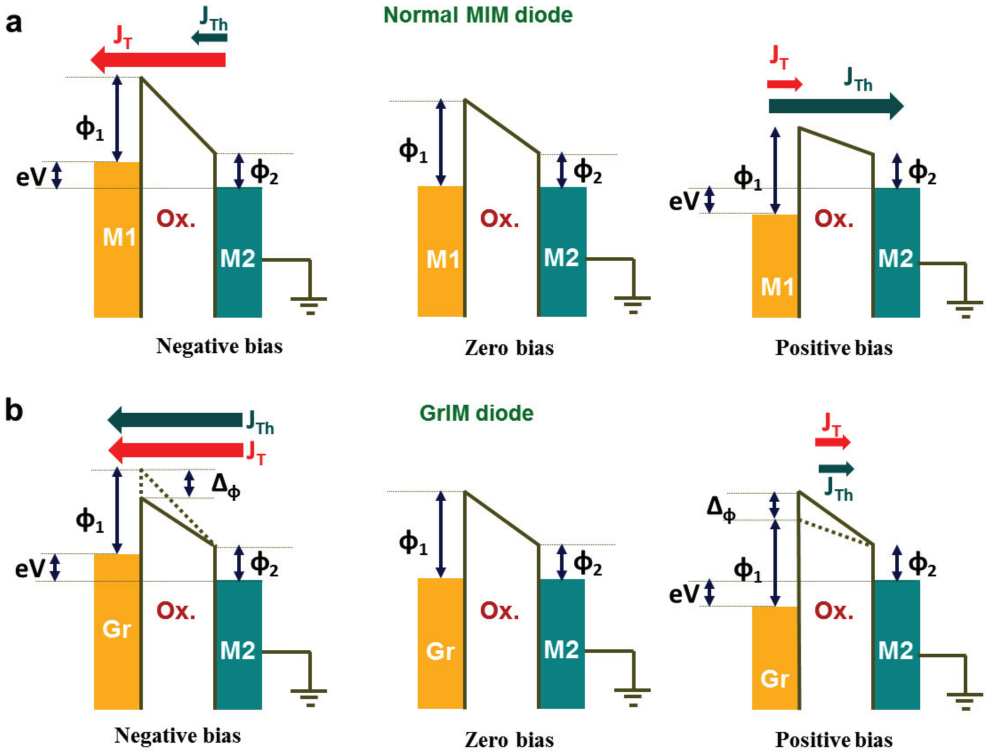

Figure 6.4. Comparison between the operation principle of a) a conventional MIM and b) a GrIM diode. $\Phi_1$ and $\Phi_2$ correspond to the difference between the respective work function of the metal electrode and the electron affinity of the oxide insulator. $J_{Th}$ and $J_T$ denote the thermionic emission and tunneling current, respectively. In both cases, it is assumed that the lower work function electrode (M2) is grounded and a potential is applied to the higher work function electrode (M1 or graphene, Gr). Moreover, possible image potential effects are neglected to a first approximation.

In contrast to the MIM diode, where the barrier height is fixed, in the GrIM diode the barrier height between graphene and insulator depends on the applied bias, as the latter is able to modulate the work function of graphene (Fig. 6.4b). In the depicted model, graphene has a higher work function than the metal M2. When a positive bias V is applied, the work function of graphene increases by ΔΦ, resulting in a barrier height for the thermionic current of $\Phi_1$-eV + ΔΦ. The thermionic current depends on the relative magnitude of eV and ΔΦ. If eV<ΔΦ, the thermionic current is fully blocked. This condition occurs when the oxide layer is sufficiently thin and has a very large dielectric constant. When applying a negative bias, the work function of graphene decreases by ΔΦ, leading to a barrier height is $\Phi_1$-ΔΦ. Hence, by contrast to the MIM diode, in the GrIM diode both the thermionic and tunneling current is forward for negative bias. Due to the bias-induced barrier height reduction, the tunneling current should exceed that in the MIM structure, thus rendering the former type of diode more efficient.

Fig. 6.5 shows the diode performance in dependence of the number of layers in the graphene sheet. According to the above proposed operation mechanism, the performance of the GrIM diode is expected to increase with the modulation rate of the barrier potential ΔΦ(V), which is a function of applied bias. Hence, the diode performance should increase when the thickness of the graphene electrode and the $TiO_x$ layer is decreased. In addition, the initial position of the Fermi level in graphene (due to external doping effects) should also influence the diode performance. Our experiments indeed confirmed both these trends. In particular, bilayer graphene devices, whose Dirac point was found to be close to 0 V, exhibited an asymmetry of up to 9000 and a nonlinearity of 8 at 1 V, as depicted in Fig. 6.5c. For the responsivity of the device, we obtained a value of $\approx 10$ V$^{-1}$ at +1 V bias voltage, which is above 7 V$^{-1}$, thus rendering the overall performance useful.[174]

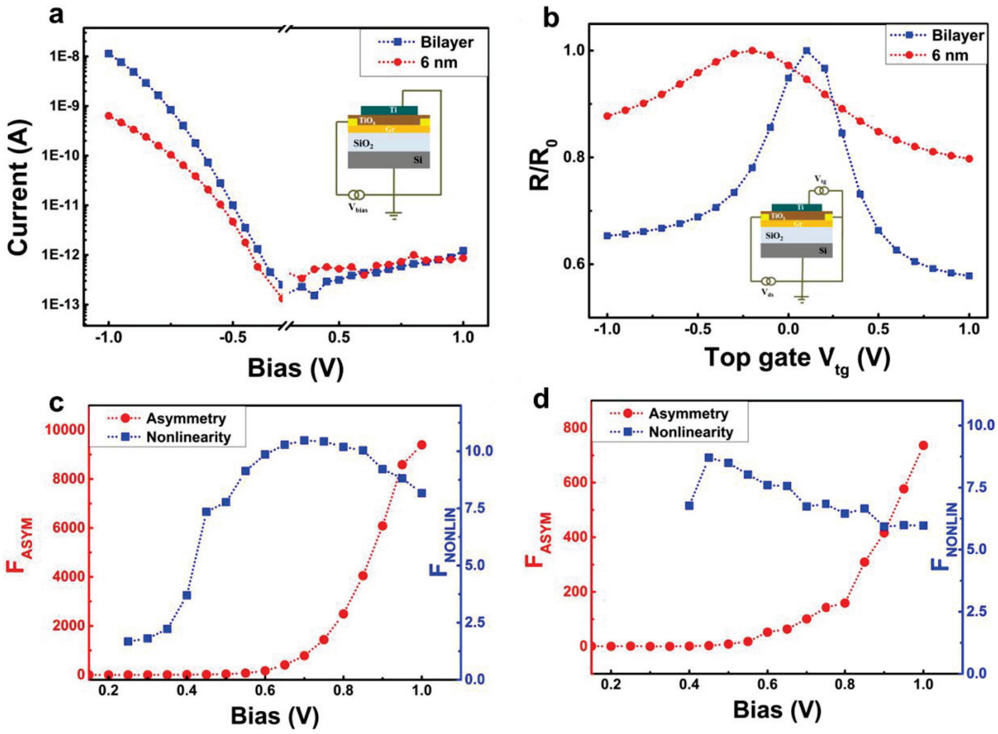

Figure 6.5. Electrical characteristics of the Gr-$TiO_x$-Ti diodes in dependence of the graphene thickness. All data were acquired at room temperature. a) Semilogarithmic I-V curves of two different diodes comprising a graphene bilayer (blue squares) and a 6 nm thick graphene sheet (red circles), respectively. b) Normalized resistance of the graphene channel as a function of Ti top gate voltage. Asymmetry and nonlinearity plotted vs. bias voltage for c) a bilayer graphene diode and d) a Gr-$TiO_x$-Ti diode comprising a 6 nm thick graphene layer.

By comparison, for a diode comprising monolayer graphene, we observed an increase of asymmetry for increasingly negative back gate voltages, i.e., when the Fermi level in graphene approaches the Dirac point which due to the n-type doping of graphene is located within the negative gate voltage regime (Fig. 6.6a). Moreover, based upon the lateral device size of 3 x 4 μm$^2$, the on-current density is estimated to be $\approx 0.1$ A/cm$^2$. This value is comparable to those reported for the best MIM diodes realized as Nb-$Nb_2O_5$-Pt,[174] and much higher than for Nb-$TiO_2$-Pt diodes[173] wherein also $TiO_x$ serves as insulator. In the GrIM diode, the Ti electrode acts like a top gate in field-effect transistor configuration. Thus, it is possible to control the work function of graphene even if the sheet is relatively thick,[199] as exemplified in Fig. 6.5b for a GrIM diode with a 6 nm thick graphene layer. It is noteworthy that the diode performance turned out to depend also on the size of graphene area. Specifically, we found that the performance decreases with decreasing the lateral size of the graphene sheet. This behavior can be attributed to an increasing influence of the Ti-Au contact, which in the smallest devices is likely to pin graphene's Femi level in the region below the $TiO_x$-Ti electrode (Fig. 6.6b).

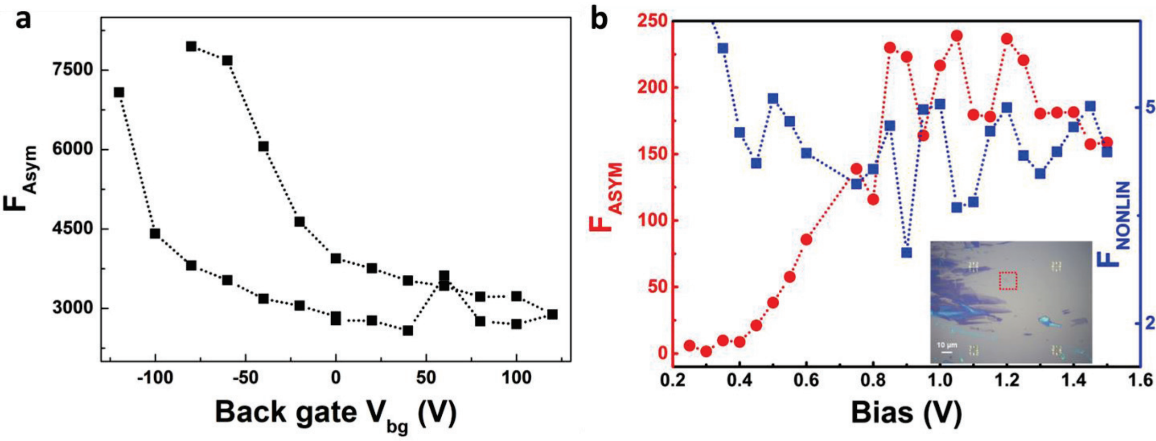

Figure 6.6.a) Back gate dependence of the asymmetry. The pronounced asymmetry at negative gate voltages indicates that when the Fermi level in graphene approaches the Dirac point, the lower density of states leads to a faster Fermi level shift. b) Performance of a GrIM diode with small lateral dimension. The graphene flake (marked by dashed red square in the inset) has a size of ≈3 μm. For such a small size, low device performance is observed, even for bilayer graphene.

To shine light on the mechanism of charge transport in the diodes, we determined the temperature dependence of the I-V characteristics of the device in Fig. 6.5. For both the positive and negative bias regime, the current decreases notably with decreasing temperature as shown in Fig. 6.7. In fact, below 100 K, the current is less than $10^{-12}$ A at 1.5 V (see appendix B for corresponding measurements at lower temperatures). This strong temperature activation demonstrates that tunneling is not the predominant transport mechanism within the bias window of ±1.5 V.

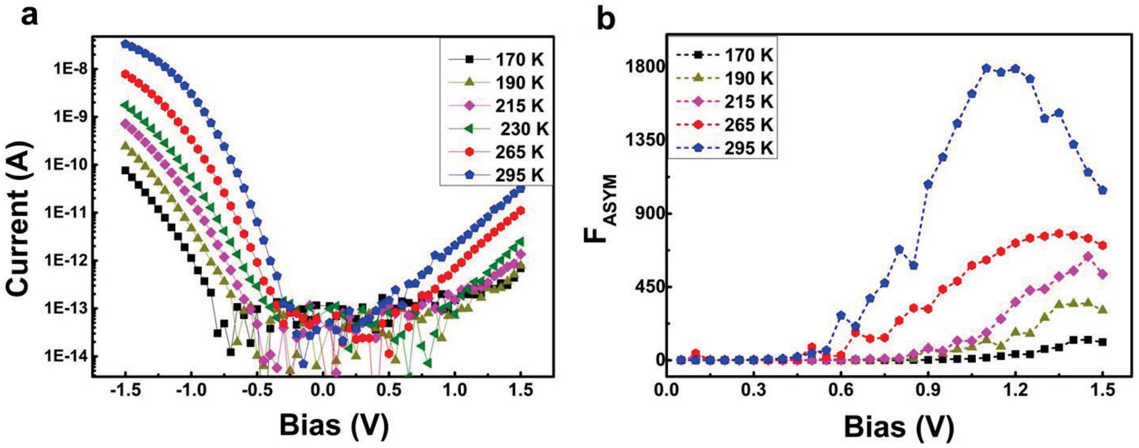

Figure 6.7. Performance of a Gr-$TiO_x$-Ti diode as a function of temperature. a) Semilogarithmic plot of current vs. voltage for a temperature range between 170 K and room temperature. b) Asymmetry of the device within the same temperature range as in panel a).

As concluded from the fits in Fig. 6.8a,b, charge transport in the positive bias regime rather occurs through thermionic emission and Poole-Frenkel tunneling (trap state-assisted tunneling).[200] In the bias range from +1.3 to +1.5 V, the extracted barrier potential for the thermionic mechanism is 180 - 200 meV, while the barrier height associated with the Poole-Frenkel mechanism is 220 - 240 meV. It follows that the potential drop across the oxide layer remains quite small even if a high bias is applied (Fig. 6.8). In the negative bias regime, the experimental current cannot be fitted by either the thermionic emission or the Poole-Frenkel mechanism. Instead, it is plausible to assume that the barrier height becomes so small that the current passes directly through the $TiO_x$ layer via hopping between the trap states (Fig 6.8c,d).

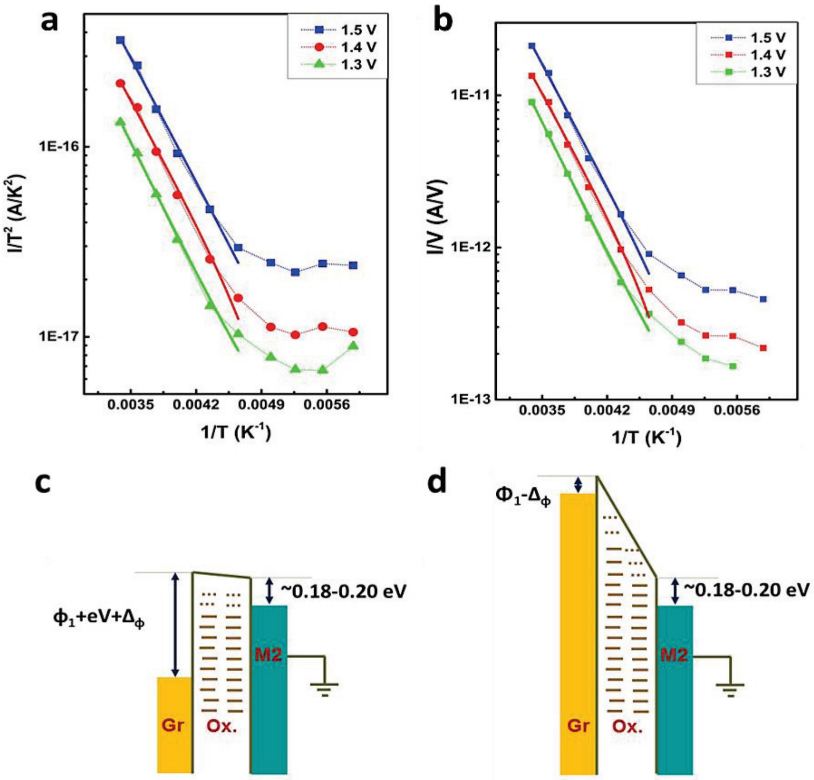

Figure 6.8. Fits of the electrical data gained from a bilayer graphene Gr-$TiO_x$-Ti diode, based upon the a) thermionic and b) Poole-Frenkel mechanism.[200] The fits in panel a) yield for the barrier height between the conduction band of $TiO_x$ and the Ti electrode values of 199, 176 and 185 meV at 1.3, 1.4 and 1.5 V, respectively. From the fits in panel b), one extracts a barrier height of the trap state of 230, 226, 219 and 240 meV at 1.3, 1.4 and 1.5 V, respectively. c,d) Band alignment at c) high positive and d) high negative bias applied to the Gr-$TiO_x$-Ti diode. While at high positive bias, the slope of the potential barrier is almost flat, for high negative bias the barrier height at the graphene side becomes very small.

The diode asymmetry decreases quite fast upon cooling (Fig. 6.7b). This change is somewhat unexpected, as $F_{ASYM}$ should increase with decreasing temperature if the thermionic current is dominant (($\approx \exp((\Phi_1-\Phi_2)/k_BT)$). A possible explanation for this discrepancy involves the presence of trap states inside the $TiO_x$ layer, which limit the charge transport through the barrier. At room temperature, the on-current at high negative bias increases only slowly, while the off-current at high positive bias still exponentially increases with bias. As a consequence, $F_{ASYM}$ first increases upon increasing the bias, then reaches a maximum at a voltage of ≈1.1 V, and finally decreases. That the voltage position of the maximum shifts to higher bias upon cooling can be explained by the presence of trap states, due to which a higher bias must be applied to reach maximum current at lower temperatures. An opposite trend compared to $F_{ASYM}$ is observed for $F_{NONLIN}$, which increases upon cooling. Furthermore, in the plot of $F_{ASYM}$ and $F_{NONLIN}$ (both at a bias of 1.2 V) as a function of inverse temperature (Figure 6.9), in each case two different exponential regimes can be discerned, indicative of two major types of current contributions. Taking the above observations together, the trap states emerge as the major factor that limits of the diode performance. Significant reduction of the trap density could be achieved by alternative methods of depositing the $TiO_x$ layer, for instance with the aid of atomic layer deposition.

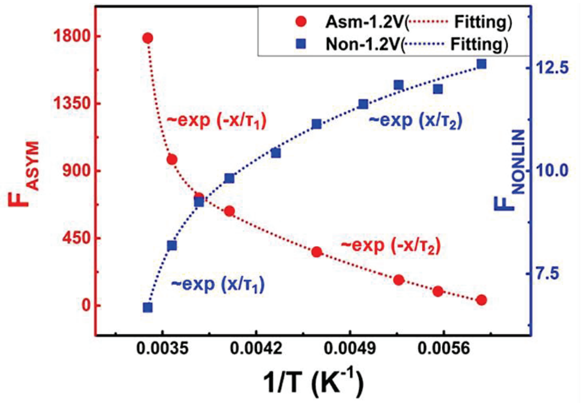

Figure 6.9. a) Temperature dependence of nonlinearity of a GrIM diode. b) Plot of asymmetry (red points) and nonlinearity (blue points) against inverse temperature. The dotted red and blue lines are exponential fits to the data.

The major advantage of the GrIM diode becomes evident when the minimum possible oxide thickness is approached. In the conventional MIM diode, the tunneling current is high in the negative bias regime, whereas the thermal current is high in the positive bias regime. Moreover, its asymmetry is smaller for a very thin oxide layer (leading to dominant tunneling), as compared to a thick oxide layer (dominant thermal current). Accordingly, it is rather difficult to achieve good performance of the MIM diode in the high frequency range, for which predominant tunneling is essential. The situation is more favorable for the GrIM diode, as here the tunneling and thermal current have the same polarity (high current at negative bias), such that the asymmetry is maintained or even increased when the oxide thickness is decreased. In the Gr-$TiO_x$-Ti diode with the 6 nm thick $TiO_x$ layer (Fig. 6.5), charge transport still occurs mainly through the thermal mechanism. To investigate the performance for a very thin oxide, we fabricated devices of inverted configuration, wherein a 15 nm thick layer of Ti serves as bottom electrode instead of graphene. A natural, approximately 2 nm thick oxide layer was then formed on the Ti by oxidation under ambient. In the next step, graphene was mechanically exfoliated on top of the Ti-$TiO_x$. For reference, we used Ti-$TiO_x$-Pd devices as typical MIM diodes. The performance of the Ti-$TiO_x$-Gr and Ti-$TiO_x$-Pd devices, both with a natural $TiO_x$ layer, is compared in Fig. 6.10. In the Ti-$TiO_x$-Pd diode, the forward current occurs in the positive bias regime, but the current at negative bias is also quite high, leading to a low asymmetry of only 30. By contrast, the I-V characteristic of Ti-TiO$_x$-Gr diode features the forward current in the negative bias regime, along with a significantly larger asymmetry of 400, one order of magnitude larger than for the Ti-TiO$_x$-Pd device. It should be noted that the performance of the inverted structure (Ti-TiO$_x$-Gr) is smaller than for the Gr-TiO$_x$-Ti devices. This unexpected difference may be explained by adsorbates from the ambient that restrict the bias-induced work function change in graphene.

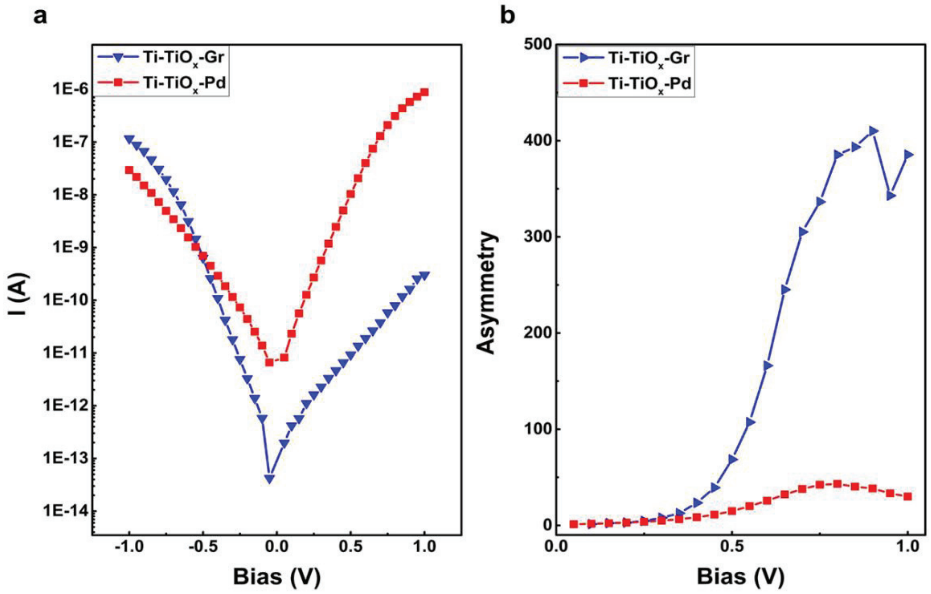

Figure 6.10. Comparison of I-V curves a) and asymmetry b) for Ti-TiO$_x$-Gr (blue triangles) and Ti-TiO$_x$-Pd (red squares) devices. All data were recorded at room temperature. Both types of devices comprise native TiO$_x$ (formed by Ti oxidation under ambient) with a thickness of approximately 2 nm.

We furthermore studied devices comprising TiO$_x$ layers of increasing thickness. In order to reach an oxide thickness above ≈2 nm, the native oxide formation was combined with subsequent atomic layer deposition of TiO$_x$. The asymmetry of Ti-TiO$_x$-Pd devices is seen to decrease with decreasing oxide thickness (from almost 7000 to 30), while it increases for the Ti-TiO$_x$-Gr devices (Fig. 6.11), further highlighting the advantage of the GrIM diode.

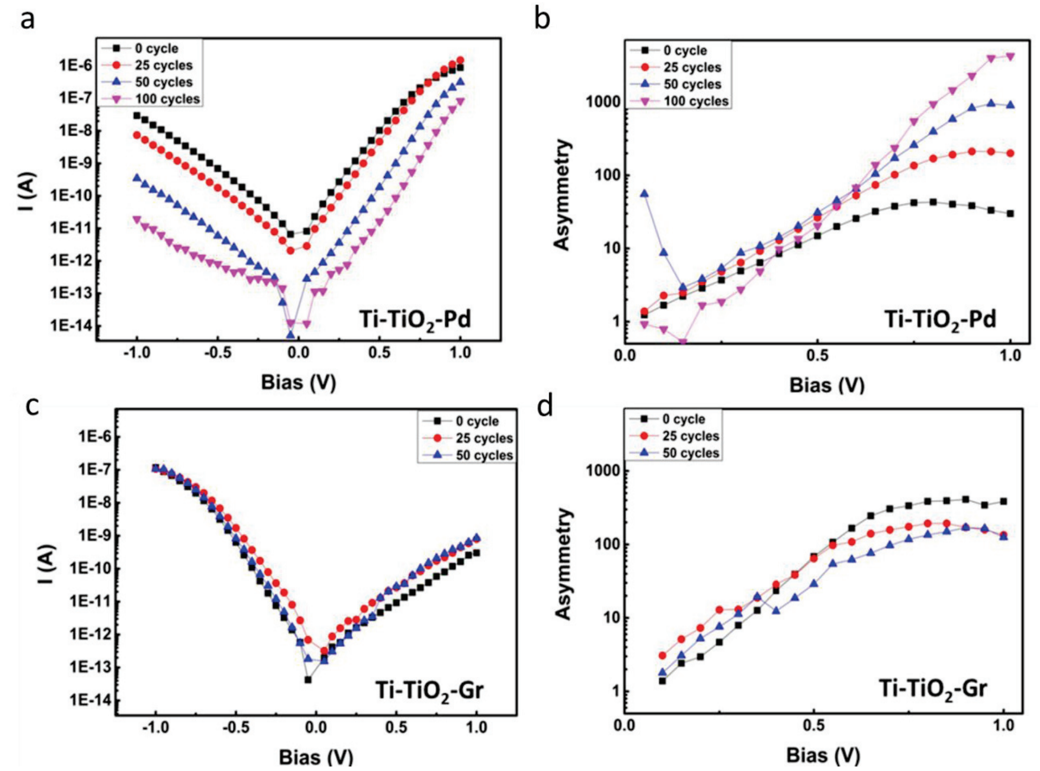

Figure 6.11. Performance of Ti-TiO$_x$-Pd diodes fabricated using a different number of atomic layer deposition cycles of TiO$_x$ (i.e., different thickness of TiO$_x$ oxide). a) I-V curve and b) the asymmetry at different bias. The current in the negative bias regime strongly increases with decreasing the TiO$_x$ thickness. In all devices, there is an underlying natural TiO$_x$ layer (about 2 nm thick) formed by Ti oxidation in air. c,d) Performance of Ti-TiO$_x$-Gr diodes obtained using a different number of atomic layer deposition cycles of TiO$_x$. The I-V curves remain almost unchanged upon decreasing the TiO$_x$ thickness.

## 6.4 Hot carrier extraction in Gr-TiO$_x$-Ti diodes: third generation photovoltaics

Hot carriers generated during chemical reactions or via photoexcitation are important for a wide range of optoelectronic or molecular processes. For example, heterogeneous catalysis often involves a flow of hot electrons with an excess energy of 1 to 3 eV. [201] In general, photo-excited hot electrons in a metal can stimulate various effects, including photoemission, photochemistry, photo-desorption, as well as electrical doping.[201,202] With respect to device physics, hot carriers are relevant for achieving efficient photodetection,[203] and they are a major factor contributing to the degradation of transistors.[204] Moreover, they open up the possibility to enhance the light harvesting efficiency of semiconductor-based solar cells. In such devices, photons with energies smaller than the material's band gap cannot be absorbed, while higher energy photons lose their extra energy via fast thermal-relaxation processes.[205] These two major factors limit the efficiency of single band gap solar cells to 41%.[206] One possibility to avoid the loss of non-absorbed photons involves the use of heterostructures combining multiple band gaps.[205] The relaxation-induced loss of the extra energy, on the other hand, can be reduced by multicarrier generation,[207–209] i.e., photon conversion into additional electron-hole pairs, or by extracting the hot photo-excited carriers before they relax to the band edge.[189,201,210–213] The above strategies have been pursued for decades, with focus mainly on semiconductor quantum dots in the case of multicarrier generation, and metallic nanostructures or ultrathin films in the hot carrier case. However, despite some recent progress in these directions, the maximum attained solar cell efficiency is still below that needed for technological applications.[214]

Their atomic layer thickness renders 2D materials especially suitable for hot carrier manipulation.[215–217] In this context, graphene has attracted particularly strong attention due to its zero band gap, high intrinsic carrier mobility, broadband photon absorption, as well as the phonon bottleneck for electrons with low energies (<200 meV).[13–15] These features endow excited or hot carriers in graphene with longer lifetimes than in normal metals,[16] thus facilitating extraction of the hot carrier before they relax to the Fermi level. Hence, many efforts have been directed to exploit hot carriers in graphene, most prominently for photo-electrical conversion.[38–43] However, in these devices the photo-thermal effect usually dominates over the photovoltaic effect[38,39] and due to the small Seebeck coefficient of graphene only very small photo-voltages on the order of few hundreds of microvolt are obtained.[39] For instance, photo-signals generated at graphene-metal junctions, where both photovoltaic and thermoelectric contributions occur, are on the order of several millivolts.[40,43–45] In the following, Gr-$TiO_x$-Ti devices are described which due to the dominance of the photovoltaic effect yield an open circuit potential ($V_{oc}$) of up to ≈0.3 V after graphene doping. The key strategy involves the use of $TiO_x$ as a hole blocking layer to harness the work function difference between the graphene and Ti electrodes.

The structure of the Gr-$TiO_x$-Ti heterojunction device is schematically illustrated in Fig. 6.12a. As discuss in the previous section, when the graphene and Ti electrodes are electrically connected, the oxide layer in between is expected to form a trapezoid-shaped barrier. The actual barrier heights for electrons in the graphene and Ti electrode sides are 0.4 eV and 0.2 eV, respectively, as determined in the previous section. There arise two possible mechanisms to extract the hot carriers from graphene through the $TiO_x$ barrier into the Ti electrode, as shown in Fig. 6.12b. Upon illumination by photons with energy larger than 0.4 eV, electrons in graphene are excited above the conduction band edge of the $TiO_x$ layer. In the first mechanism, the excited electrons are directly transferred through the $TiO_x$ conduction band to the Ti electrode before they relax below the conduction band edge of $TiO_x$ (process 1). Here, charge transport can occur either through the empty conduction band[189] or trap states of $TiO_x$. The second mechanism involves fast relaxation of the excited electrons to the newly established quasi-Fermi level, where they reside longer due to the bottleneck of the optical phonon scattering. From there, the electrons can tunnel (process 2) either directly or indirectly through trap states in $TiO_x$ (Poole-Frenkel tunneling) to the Ti electrode. In addition, electrons at the Fermi level, which are heated by the relaxation of photo-excited carriers, can also contribute to the photocurrent of the device.[15] At the same time, the light-generated holes are effectively blocked by the deep lying valence band edge of $TiO_x$.

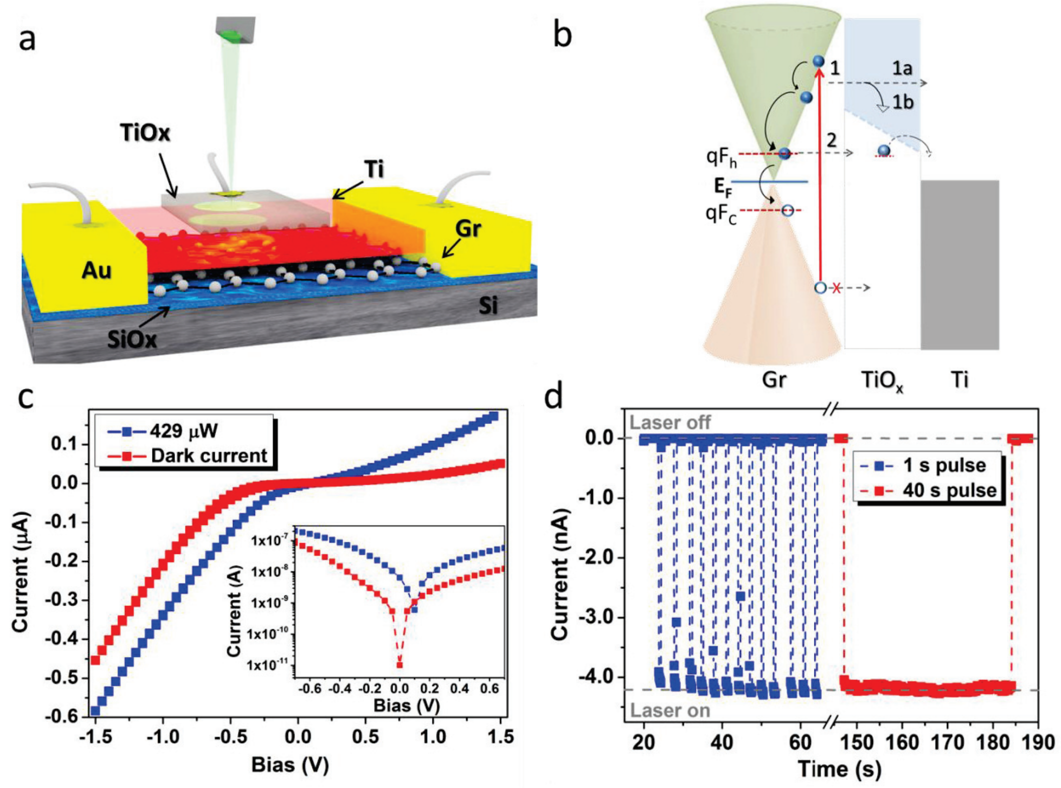

Figure 6.12. Structural design of the device used for hot carrier extraction from graphene. a) Schematic representation of the Gr-$TiO_x$-Ti device. b) Electronic band alignment of the Gr-$TiO_x$-Ti heterostructure. The two major mechanisms of hot carrier extraction are denoted by dashed horizontal arrows 1 and 2. c) Room temperature I-V characteristics acquired with and without laser illumination. The inset is a semi- logarithmic plot of current in dependence of bias voltage, revealing a $V_{oc}$ and $I_{sc}$ of 0.1 V and 7 nA, respectively. d) Time-dependent $I_{sc}$ detected upon sample illumination with laser pulses of 1 s (blue dots) and 40 s (red dots) duration.

Fig. 6.12c shows I-V characteristics, acquired between the graphene and Ti bottom electrode of one device, without (red curve) and with (blue curve) illumination by a green laser ($\lambda = 514$ nm). The dark I-V curve is rectifying as a consequence of the much more pronounced blocking capability of the $TiO_x$ barrier for holes than for electrons, which leads to the unusual diode-like behavior explained above. This involves the forward (reverse) current occurring at negative bias (positive) bias, in contrast to conventional MIM diodes. As a consequence, under illumination a quasi-equilibrium state is created, which reduces the barrier height between graphene and $TiO_x$, explaining the emergence of a comparable photocurrent for both, negative and positive bias. The semi-logarithmic plot (inset of Fig. 6.12c) reveals generation of a short-circuit current ($I_{sc}$) of 6 nA and an open circuit voltage ($V_{oc}$) of 0.1 V. Remarkably, the detected $V_{oc}$ is two orders of magnitude larger compared to previous reports on graphene-based devices whose photoresponse is governed by the photo-thermal effect.[38,39] We assign the sizeable $V_{oc}$ to the extraction of hot carriers from graphene.

However, the fact that $V_{oc}$ is well below values typically observed for conventional solar cells indicates significant hot carrier relaxation. The question of whether this relaxation occurs predominantly within the graphene or $TiO_x$ layer will be addressed further below.

To test the importance of the $TiO_x$ for the device performance, we investigated also devices without the $TiO_x$ layer (Fig. 6.13). In general, the Ti-Gr devices under illumination displayed lower short circuit currents on the order of 1 nA, and no detectable open circuit potential (see the semi-logarithmic plot in the inset). This low $I_{sc}$ is caused by the photo-thermal effect, similar to previous observations on the graphene-metal interface.[40,43–45] The above Gr-$TiO_x$-Ti device was further studied under non-continuous illumination (Fig. 6.12d). Consecutive 1 s pulses (blue circles) yielded a highly reproducible photocurrent response, with a two orders of magnitude larger and also faster response compared to Gr-$Ta_2O_5$-Gr devices.[120] Moreover, even after applying a longer, continuous pulse of 40 s duration (red circles), the signal returns instantaneously to zero (within our millisecond detection limit).

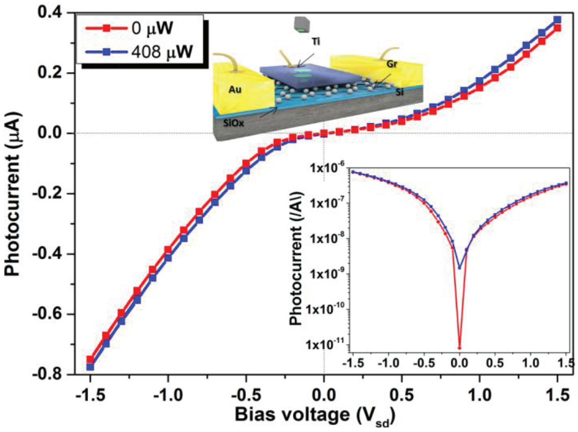

Figure 6.13. I-V characteristics of the Gr-Ti device without $TiO_x$ insulator layer. Although there is a photocurrent response in this device, no $V_{oc}$ is detectable in our measurements.

In order to confirm that the photo-excited carriers originate from graphene, we studied devices comprising graphene regions of different thickness by scanning photocurrent microscopy (SPCM). In Fig. 6.14a, an optical micrograph of such a device is presented. Fig. 6.14b compares I-V curves acquired under green laser illumination on a 3 nm and a 6 nm thick region (see Fig. 6.14c), respectively. As apparent from the profiles in Fig. 6.14d, the $I_{sc}$ induced upon local illumination of the thinner graphene region (14 nA) is twice compared to that at the thicker region (7 nA), whereas both regions displayed the same $V_{oc}$.

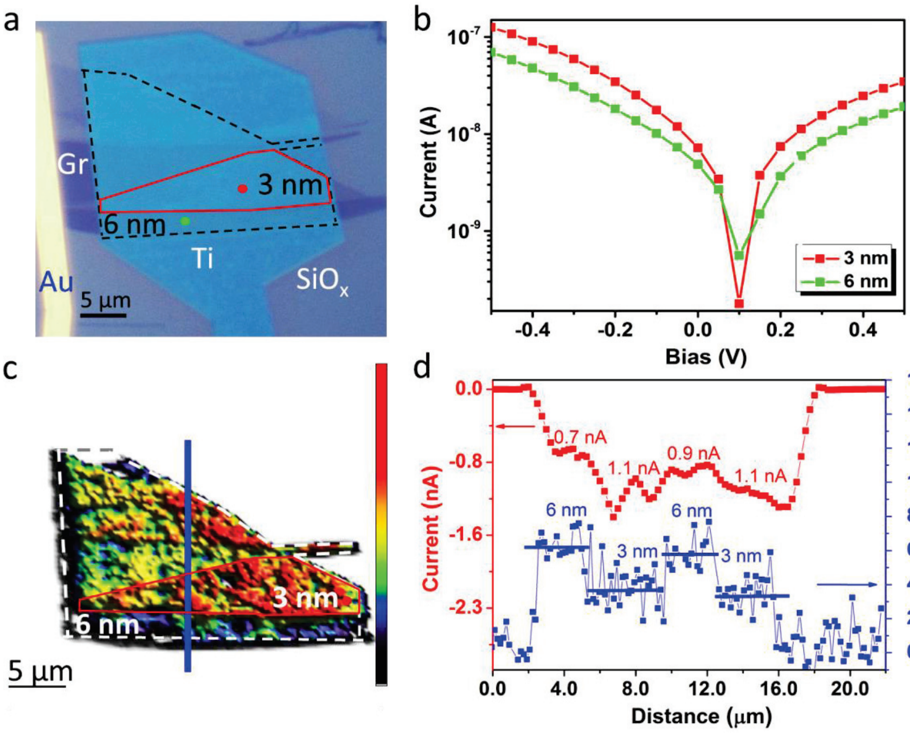

Figure 6.14. Dependence of photoresponse on graphene thickness**.** a) Optical image of a Gr-TiO$_x$-Ti device. b) I-V characteristics recorded by positioning the laser spot ($\lambda$ = 514 nm, 430 µW power) at the red and green spot in panel a), corresponding to a multilayer graphene thickness of 3 and 6 nm, respectively. c) Photocurrent map of the device, acquired at 514 nm with a power of 300 µW. The color bar is from 0 to 1.30 nA. d) Topographic AFM height (blue) and photocurrent (red) profiles, both taken along the vertical blue line in panel c).

A similar dependence of photocurrent on the thickness of the graphene areas was observed for several other devices (see Fig. 6.15). Overall, we found that the photocurrent first increases when the thickness increases from monolayer graphene ($I_{sc}$ ≈0.1 nA,) up to 3 nm thick multilayered graphene, which is followed by a photocurrent decrease up to the largest investigated thickness of 6 nm. This trend displaying a maximum around 10 monolayers is fully consistent with observations made on the intensity of graphene's Raman bands as a function of the number of layers. The latter originates from the interplay of multi-reflection and interference of the laser light for multilayered graphene on Si-SiO$_2$ substrates.[218] An additional contribution to the photocurrent decrease for thicknesses above 3 nm may arise from electrostatic screening. Such screening leads to a reduced electric field within multilayer graphene, and affects also the switching capability of graphene-based field-effect transistors.[199] That the photocurrent indeed stems from carriers in graphene gains support by the fact that the alternative mechanism involving photoexcitation of carriers from trap states in TiO$_x$ is quite slow[219,220] and hence not compatible with the respectable response speed of the devices (Fig. 6.12d).

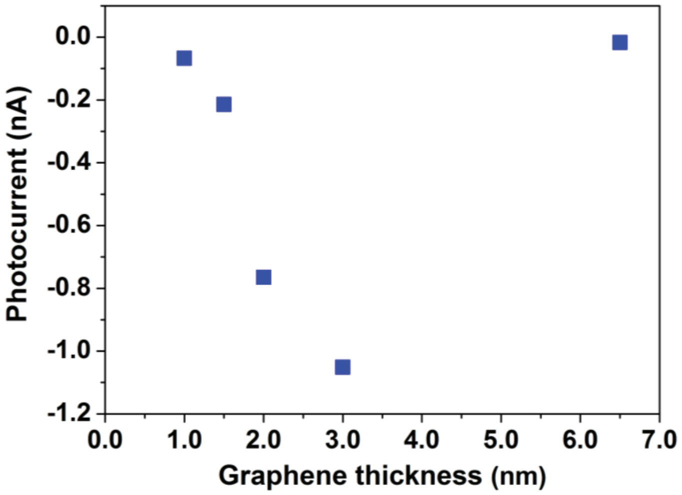

Figure 6.15. Photocurrent of Ti-TiO$_x$-Gr diodes dependence on the thickness of graphene with a green laser ($\lambda$ = 514 nm) at a power of 428 μW

Figure 6.16 shows the dependence of the photoresponse on the laser wavelength and photon flux (laser power P normalized by the photon energy hν). Figure 6.16a and b plot $I_{sc}$ and $V_{oc}$ detected under different photon flux at laser wavelengths of 488 nm, 513 nm, and 633 nm, respectively. Both $I_{sc}$ and $V_{oc}$ are seen to rise with increasing photon flux and photon energy. Such dependence on photon flux is well-documented for photovoltaic solar cells, as the higher density of excited carriers increases the photocurrent.[221] We ascribe the photon energy dependence of $I_{sc}$ to enhanced electron-electron scattering at higher photon energy, which results in a hotter carrier distribution,[15] such that more carriers are able to tunnel into the TiO$_x$. Considering that the decay time of an excited electron from the excited state to the hot quasi Fermi level is independent of the photon energy in graphene,[15] it follows that the predominant mechanism of photocurrent generation is process 2 (Fig. 6.12b). The carrier dynamics in graphene establishes a new quasi-equilibrium of the hot carriers around 0.2 ps after the optical phonon scattering.[15] As graphite shows a similar carrier dynamics like graphene,[222] the conclusion that process 2 is predominant should be valid also for multilayer graphene. In a hot carrier solar cell, $V_{oc}$ should in principle increase with increasing laser excitation energy. The plot in Fig. 6.16b, however, reveals only a small change of $V_{oc}$, at least between the two shorter wavelengths of 514 nm and 488 nm. This observation directly reflects the above mentioned hot carrier relaxation, which renders the $V_{oc}$ of the present diodes similarly insensitive to the excitation energy like for conventional solar cells.

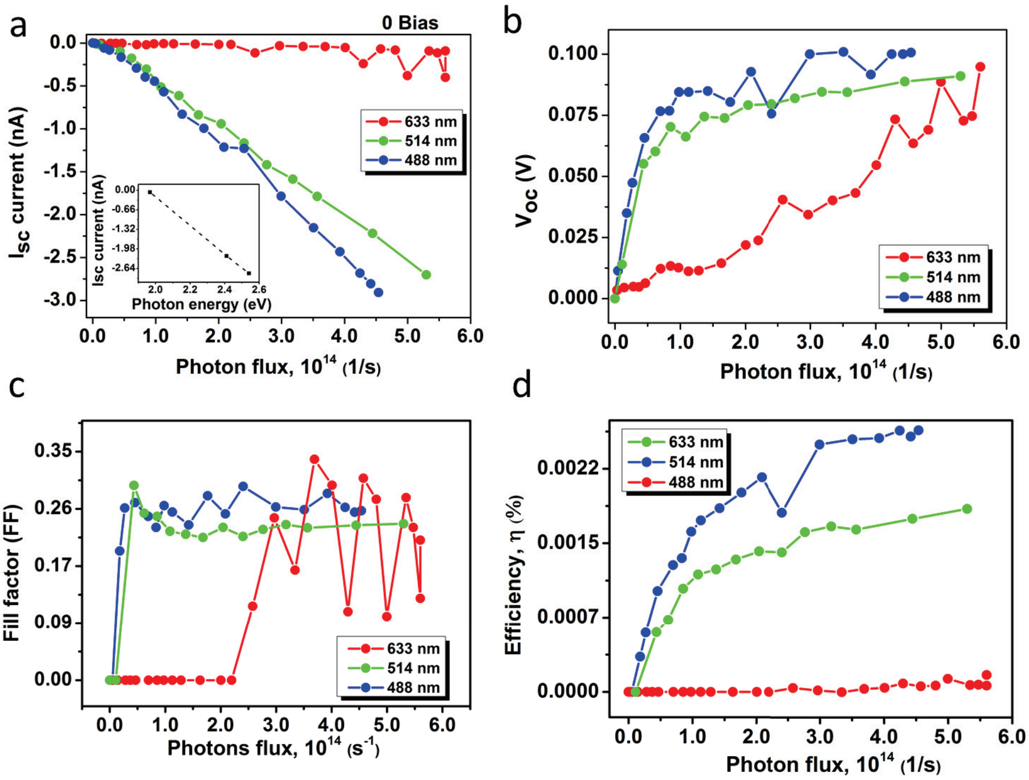

Figure 6.16. Dependence of Gr-$TiO_x$-Ti device performance on laser wavelength and power. a) Wavelength and power dependence of $I_{sc}$. For consistent comparison, the power was converted to the photon flux (P/hν). The inset shows $I_{sc}$ as a function of photon energy at constant photon flux. b) Open circuit voltage, c) fill factor and d) power conversion efficiency as a function of photon flux for three different laser wavelengths.

The calculated fill factor (FF) and the power efficiency of the device are presented in Fig. 6.16c and d. The power efficiency, defined as $\eta = \frac{I_{sc}.V_{oc}.FF}{\text{Input Power}}$ (the input power takes in account the absorption from the top Ti-$TiO_x$ electrodes), decreases with the wavelength and increases with the photon flux. This increase is initially fast, and then slows down. The ratio of $I_{sc}$ to the input power is constant, consistent with the fact that $I_{sc}$ linearly increases with increasing power. On this basis, the pronounced initial increase of efficiency is attributable to the change of $V_{oc}$ with photon flux (Fig. 6.16b). The highest detected power efficiency (internal photo-conversion efficiency, IQE) is 0.025% (0.17%). The small IQE reflects the limitation imposed by fast recombination at the metal-insulator interface, in analogy to plasmon energy collection in gold-alumina-gold devices, whose IQE of less than 1% remains well below the theoretically predicted maximum of 2.7%.[195] A slightly larger IQE of 2.75% could be reached for gold nanorod-$TiO_x$-Ti devices by ensuring that all collected carriers stem from the gold.[223]

Further insight into the charge transport mechanism in the diodes could be gained from temperature dependent measurements. As apparent in Fig. 6.17a,b, $I_{sc}$ significantly decreases upon cooling, independent of the applied bias. This temperature activation behavior points toward the presence of electron hopping between the trap states within the $TiO_x$ layer. Alternatively, hopping may occur between trap states and the conduction band of $TiO_x$. The temperature dependence of $I_{sc}$ can be well fitted by an Arrhenius-like exponential equation: $I_{sc} = I_0 \exp^{-\frac{\Delta}{2k_B T}}$, where $k_B$ is the Boltzmann constant, T is the temperature and Δ is the depth of the trap states.[224] From the fits, a barrier height of 0.1 eV is obtained. This value is significantly smaller than the barrier height for electrons of 0.4 eV (i.e., the difference between the work function of graphene and the electron affinity of $TiO_x$), and hence in accordance with the band diagram sketched in Fig. 6.12b.

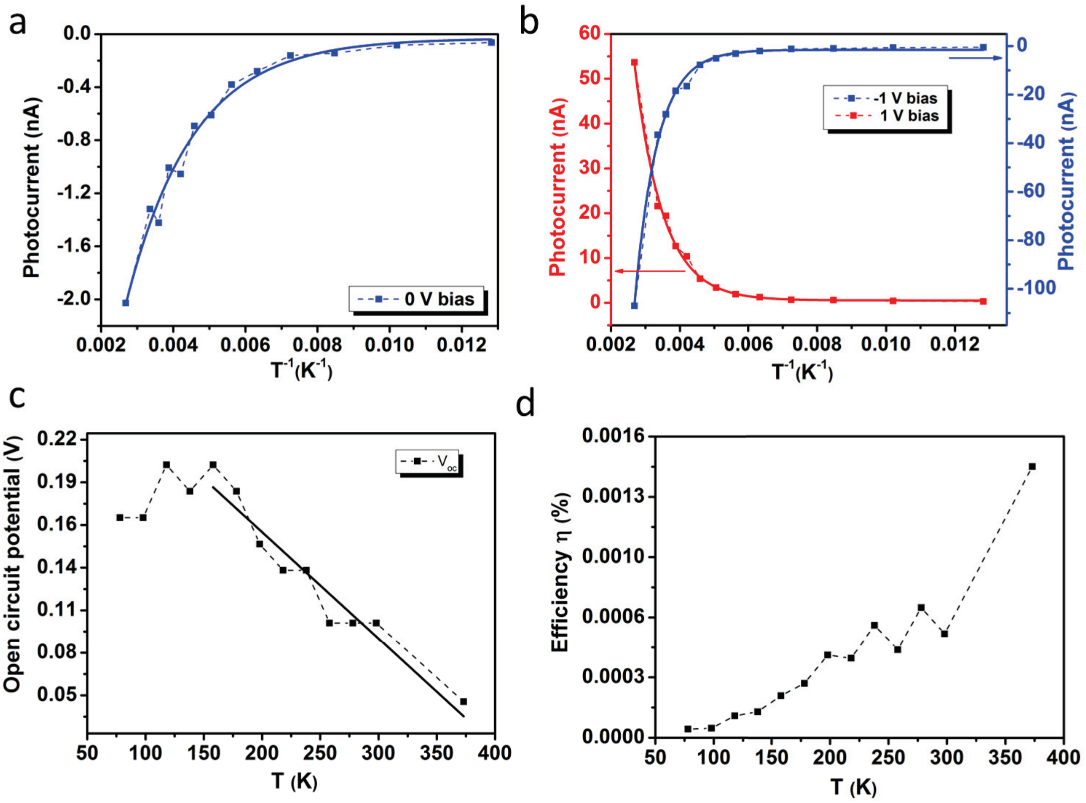

Figure 6.17. Temperature dependence of Gr-$TiO_x$-Ti device performance. The photocurrent is plotted against inverse temperature at 0 V a) and ±1 V b). The blue and red lines are fits to an exponential decay function. Temperature dependence of c) the open circuit voltage ($V_{oc}$) and d) the power conversion efficiency (η), both between 75 and 375 K.

The temperature dependence of the photocurrent at 1 and -1 V is similar to that at zero bias, although a higher photocurrent is detected under applied bias. Fig. 6.17c and d shows the temperature dependence of $V_{oc}$ and the η, respectively, at zero bias. In contrast to $I_{sc}$, $V_{oc}$ displays a close-to-linear increase upon cooling. Similar behavior has been documented for, e.g., dye-sensitized solar cells,[225] and assigned to thermally excited carriers from the trap states, which reduce the built-in electric field between graphene and the Ti electrode. Below 150°C, $V_{oc}$ reaches a saturation value of ≈0.2 V, in accordance with the potential difference between graphene and the Ti electrode.[226] From the temperature characteristics of $I_{sc}$ and $V_{oc}$ (Fig. 6.17a and b), one expects η to increase with increasing temperature, as observed by experiment.

Based upon the device operation mechanism put forward in Fig. 6.12b, it should be possible to increase $V_{oc}$ by p-type doping of the graphene. We have tested this assertion by inverting the device configuration, such that the graphene is located on the top of Ti and subsequently depositing a thin layer of the electron acceptor F4-TCNQ.[227] The influence of the doping becomes apparent from Fig. 6.18, which displays I-V curves under laser illumination for increasing thickness of the F4-TCNQ layer. Evidently, $V_{oc}$ increases with increasing amount of deposited F4-TCNQ, reaching saturation after three deposition steps (corresponding to a nominal layer thickness of 6 nm). While $V_{oc}$ increases five-fold from 0.05 V to 0.3 V, $I_{sc}$ decreases slightly, in accordance with the doping-induced increase of barrier height. These observations further consolidate the proposed mechanism of hot carrier extraction.

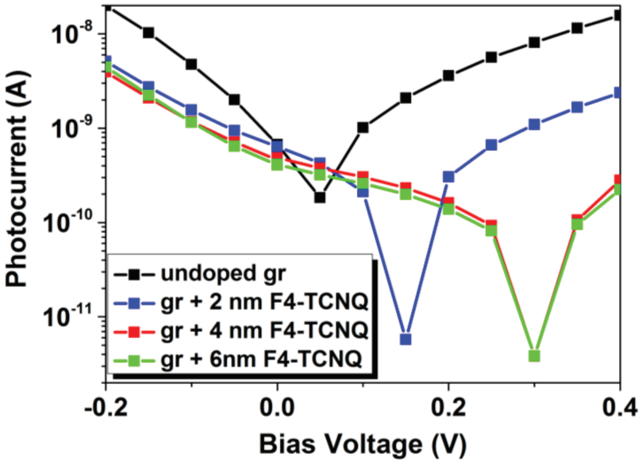

Figure 6.18. Open circuit voltage in dependence of p-type doping of graphene. Increasing deposition of the electron acceptor F4-TCNQ onto the graphene shifts $V_{oc}$ from 0.05 to 0.3 V.

# Chapter 7 Graphene-black phosphorous vertical heterostructures*

## 7.1 Black phosphorous

The lack of a band gap in graphene, which leads to only small on/off ratios,[22] renders this 2D material only partially suited for optoelectronic applications.[228,229] Advantageous in this respect is phosphorene, the monolayer constituting black phosphorous (BP) (see Fig. 7.1a). In particular, BP exhibits a fast and broadband photoresponse,[230] a carrier mobility of up to 1000 cm$^2$/Vs (for a thickness of 10 nm),[231] a tunable band gap that varies from 0.35 eV in the bulk to more than 1.5 eV in its monolayer form (direct band gap, Fig. 7.1b),[232,233] as well as the possibility of electrostatic gating.[234,235]

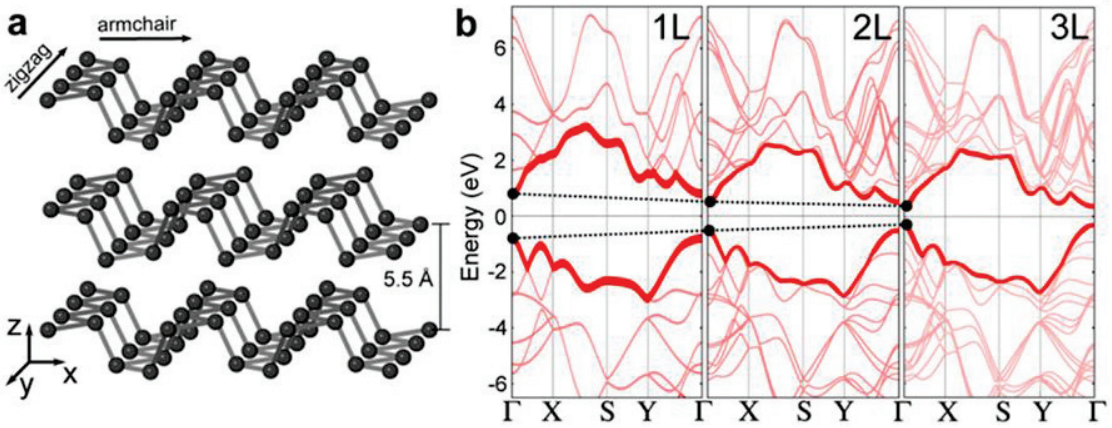

Figure 7.1. a) Schematic representation of the layered structure of black phosphorous. b) Change of the electronic band structure of BP as a function of the number of phosphorene layers. Figure adapted from ref. 236.

The tunable band gap of BP makes it an attractive material for optoelectronic devices which are able to absorb light from the visible to the near-infrared range. Such devices might find application in, for example, energy harvesting, photocatalysis, fiber optics telecommunications, and thermoelectric power generation.[236]

---

* Parts of this chapter are based on our publications *Thin-layer black phosphorus/GaAs heterojunction pn diodes* [264] and d*ual gate black phoshphorus/graphene photodetectors with high responsivity in preparation.*

Various high performance electronic devices combining BP with other 2D materials have been realized, including field-effect transistors,[237,238] ultrashort pulse generation,[239] as well as pn photodiodes.[240,241] In addition, the use such of heterostructures as active component of photodetectors has been described. While they achieve high responsivity and photo-conversion efficiency, the speed of the devices still needs to be optimized.[234,235,241,242]

This chapter deals with the use of BP as a component of photodetectors. To this end, two different types of heterostructures were investigated, which combine BP with either highly n-doped GaAs (section 7.2) or graphene (section 7.3). The first type of device was studied in order to gain first experience with the manipulation and environmental stability of black phosphorous. This knowledge was then transferred to the fabrication of BP/graphene heterostructure devices.

## 7.2 Black phosphorous-GaAs pn junction

The thin-layer BP-GaAs pn heterojunction devices were fabricated in four steps (see Fig. 7.2a). Initially, Te-doped n-GaAs substrates ($N_D^{GaAs} \approx 10^{24}$ m$^{-3}$) were first cleaned/etched and then provided with Au-GeNi contacts using standard e-beam lithography and thermal evaporation. Subsequently, the samples were annealed in order to diffuse and alloy the contact material into the GaAs substrate, and thus achieve Ohmic contacts. In the second step, immediately after additional cleaning/etching of the GaAs surface to remove native oxides and ensure good electrical contact to phosphorene, phosphorene flakes from a BP crystal (Smart Elements, Vienna, Austria) were exfoliated on top using the Scotch tape method. We observed phosphorene flakes with lateral size up to several µm and thickness down to 10 nm (Fig. 7.2c).

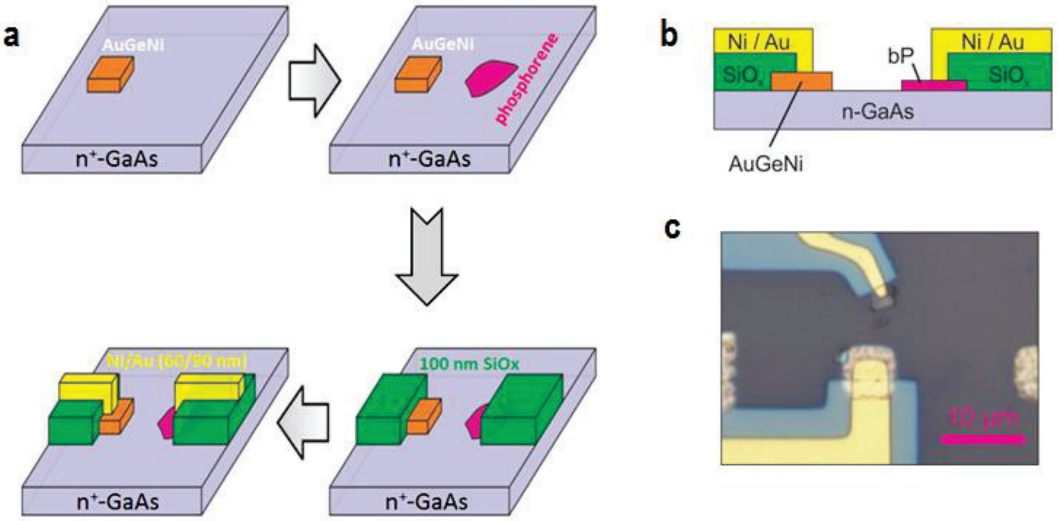

Figure 7.2. Fabrication scheme of the black phosphorous-GaAs pn heterojunction devices. a) Schematic representation of the device fabrications steps, b) sketch of the cross-section of a completed device, and c) optical micrograph of a heterojunction device (top view).

Separate electrical measurements on individual phosphorene flakes confirmed their p-type behavior (Fig. 7.3). The third step involved thermal evaporation of a 100 nm thick $SiO_x$ film at the contact regions, in order to avoid the formation of a trivial Schottky barrier between the electrical contacts to phosphorene and the underlying GaAs substrate. In the last step, the black phosphorous flakes and AuGeNi anchor points (closest to the flakes) were electrically contacted via e-beam lithography and thermal evaporation of 60 nm Ni/90 nm Au. Fig. 7.2b,c display a schematic of the cross-section and an optical micrograph of a typical device, respectively. To prevent degradation of the black phosphorous under ambient, a 50 nm thick film of PMMA was spin-coated onto the substrate directly after the lift-off procedure.

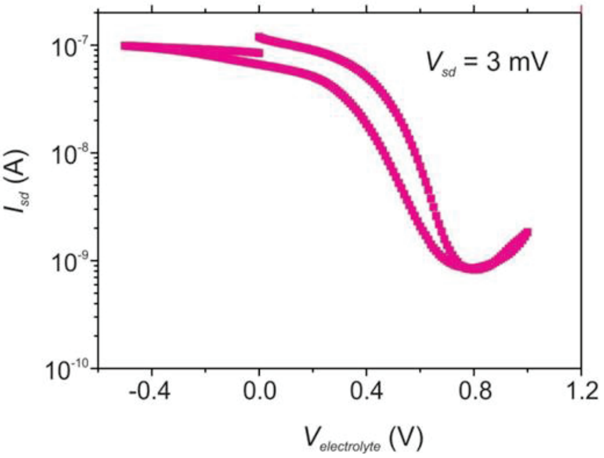

Figure 7.3**.** Electrical characterization of bare BP sheets. The transfer characteristic was recorded using a bias of 3 mV under EMI-TFSA liquid electrolyte gating. The orignally p-doped BP can be switched into the n-type regime by the gate action.

In Fig. 7.4, the band alignment of the n-GaAs-p-black phosphorous heterostructure, as derived from the Anderson model of semiconductor heterojunctions,[243] is schematically illustrated. For the work function of the heavily n-doped GaAs we assume a volue of approximately 4.1 eV, close to the electron affinity of the intrinsic material. As the band gap and work function of the BP both depend sensitively on the flake thickness, we used the numerical values for ten layers of phosphorene of $\Phi_{\mathrm{bP}} = 4.5$ eV, $\chi_{\mathrm{bP}} = 4.13$ eV and $\mathrm{E_g^{bP}} = 0.6$ eV, which should be valid for phosphorene with a thickness of several tens of nm.[244,245] Based upon these values, one calculates a built-in electric potential of $\mathrm{V_{bi}} = \Phi_{\mathrm{bP}} - \Phi_{\mathrm{GaAs}} = 0.44$ eV a conduction band offset of $\Delta\,\mathrm{E_c} = \chi_{\mathrm{bP}} - \chi_{\mathrm{GaAs}} = 0.06$ eV, and a valence band offset of $\Delta\,\mathrm{E_v} = \left(\chi_{\mathrm{GaAs}} + \mathrm{E_g^{GaAs}}\right) - \left(\chi_{\mathrm{bP}} + \mathrm{E_g^{bP}}\right) = -0.78$ eV.

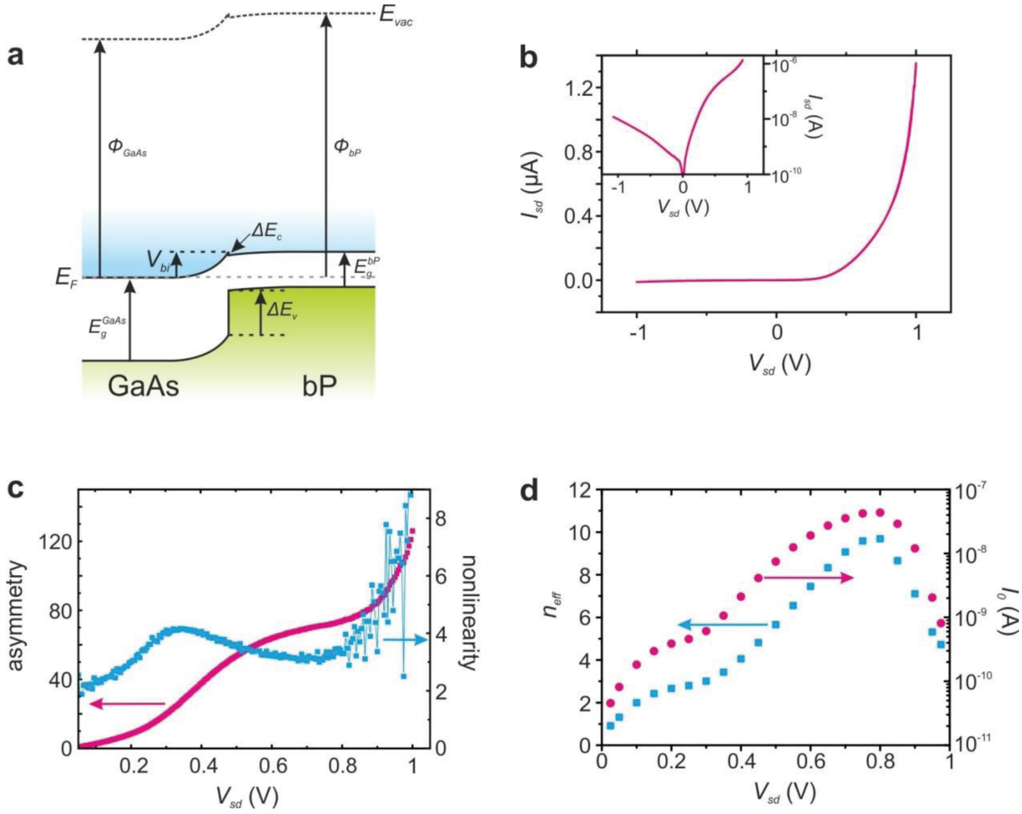

Figure 7.4. Electrical device behavior in the dark. a) Schematic depiction of the band alignment at the BP-n-GaAs heterojunction constructed using Anderson's model. The valence and conduction band are colored in green and blue, respectively. b) Room temperature I-V characteristic in linear and log scale (inset) of the device in Figure 7.2c. c) Asymmetry (pink) and nonlinearity (blue) of the device as a function of forward bias. d) Effective ideality factor and effective saturation current extracted from fits of the I-V characteristic (window size of the individual fits: 100 mV).

The output characteristic of the device described above, where the contact to n-doped GaAs is used as source and the contact to p-doped BP as drain, is shown in Figure 7.4b for the $\mathrm{V_{sd}}$ range of -1 to 1 V. The asymmetric I-V curve signifies typical rectification behavior in linear and log scale (inset) as expected for a pn junction. The asymmetry $\frac{\mathrm{I_{sd}(V)}}{\mathrm{I_{sd}(-V)}}$ and the nonlinearity $\frac{\mathrm{dI/dV}}{\mathrm{I/V}}$ extracted from this curve are plotted in Fig.

7.4c.[246] For this specific device, the rectification ratio (= asymmetry) is 120 at a bias of 1 V. From the entire set of investigated devices, we determined rectification ratios between 100 and 1000. Such notable variation most likely originates from variations in both, the BP flake thickness and the active device area (corresponding to a different area to edge ratio of the heterostructures).[247] In addition, the fabrication process itself might slightly change the device characteristics, since BP is chemically quite sensitive against ambient.[248] Another important parameter that can be extracted from the I-V characteristic of the diodes is the ideality factor n which provides useful information about charge transport mechanism as well as the device quality.[249] Fig. 7.4d displays the effective saturation current $\mathrm{I_0^{eff}}$ along with the effective ideality factor $\mathrm{n_{eff}}$ of the above device, as extracted from the I-V curve using $\mathrm{I_{sd}} = \mathrm{I_0^{eff}} \exp\left(\frac{\mathrm{V_{sd}}}{\mathrm{n_{eff} k_B T}} - 1\right) - \mathrm{I_{pc}}$, where $\mathrm{I_{pc}}$ is the photocurrent. Both these parameters contain contributions of a recombination current and Ohmic shunt (parallel to the diode) and series resistances. At low bias, $\mathrm{n_{eff}}$ is found to be close to 2, the theoretical value for an ideal diode where only recombination currents occur at the junction. Upon increasing the bias, $\mathrm{n_{eff}}$ reaches a maximum value of 9.7 (at 0.8 V). Such high value indicates strong recombination due to defects,[247,250] which might comprise intrinsic point defects inside the BP, surface defects on it arising from chemical degradation, or due to a bad contact between BP and GaAs. Another explanation involves the presence of an alternative transport channel (shunt resistance). In the high bias regime (above 0.8 V), the ideality factor decreases again as a consequence of the increased diffusion current

The pn diode behavior of the devices could be further confirmed by scanning photocurrent microscopy measurements (SPCM). Fig. 7.5a,b, respectively, depict an optical reflection image and photocurrent map of the above device, recorded at $\mathrm{V_{sd}} = 0$ V using a laser wavelength of 514 nm and a laser power of 36 µW. It is evident that efficient charge carrier separation and thus photocurrent generation exclusively occurs at the region, where the BP flake and the underlying GaAs substrate form a heterojunction. The negative sign of the photocurrent is in accord with the corresponding band diagram in Fig. 7.4b. Moreover, the uniformity of photocurrent over the whole BP region even near the Ni/Au contact, combined with the absence of photocurrent generation at the AuGeNi contact to GaAs, prove that the asymmetric I-V characteristic originates from a real pn junction rather than Schottky barriers at the contacts to the individual semiconducting components. In the latter case, a gradual decrease of photocurrent with increasing the distance from the contact is commonly observed.[45] Although a (small) Schottky barrier might exist between Ni/Au and BP the overall photocurrent signal is clearly dominated by the signal located at the pn junction.

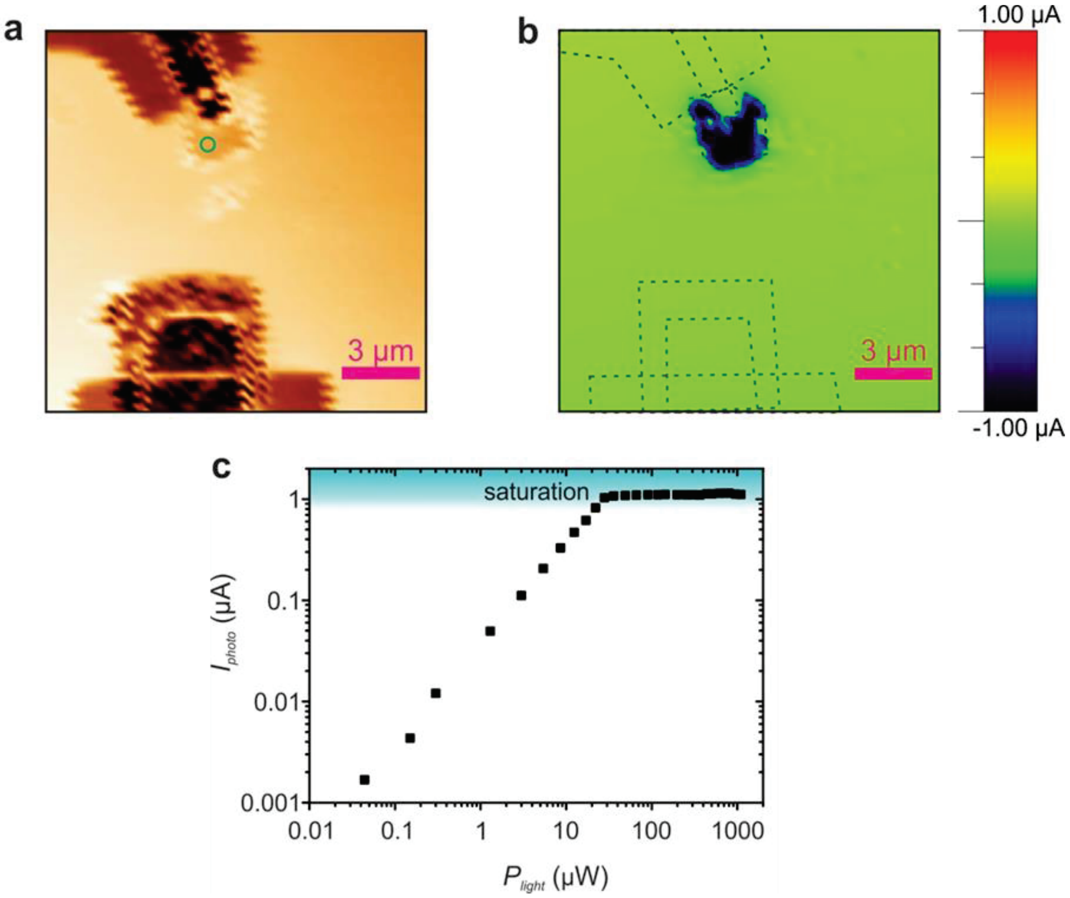

Figure 7.5. Zero-bias photoresponse. a) Optical reflection image and b) photocurrent map of the device in Fig. 7.2c. c) Photocurrent as a function of laser power at λ = 514 nm. The signal was acquired from the green circle in panel a). The blue shaded region visualized current saturation.

The dependence of photocurrent on laser power is illustrated in Fig. 7.5c, which plots the maximum photocurrent of the same device extracted from individual zero-bias photocurrent maps recorded at different light powers. The linear increase of photocurrent with increasing light power is in agreement with the established behavior of photodiodes. From a linear data fit, one obtains a responsivity $R = I_{pc}/P_{light}$ of 37 mA/W (at zero bias and λ = 514 nm), comparable to values reported for BP-MoS$_2$ or CNT-MoS$_2$ heterojunctions, although the latter were recorded under sizable bias.[251,252] Above approximately 30 µW, the photocurrent abruptly flattens (at about 1.1 µA) owing to the saturated optical absorption of the BP flake at high light intensities. In the present device, due to the very high doping level of the GaAs, the space charge region is mostly confined to the BP layer (see Fig. 7.6), whereas only a very thin positive space charge region exists in GaAs. Hence, the magnitude of the photocurrent is mainly governed by the number of available charge carriers inside the BP flake. The thickness of the depletion layer can be estimated by the equation:

$$W = \sqrt{\frac{2\cdot\varepsilon_{GaAs}\varepsilon_{bP}\cdot\left(N_A^{bP}+N_D^{GaAs}\right)^2(V_{bi}-V)}{qN_A^{bP}N_D^{GaAs}\left(N_A^{bP}\varepsilon_{bP}+N_D^{GaAs}\varepsilon_{GaAs}\right)}} \qquad (7.1)$$

if GaAs is considered, or by:

$$W = \sqrt{\frac{2 \cdot \varepsilon_{bP} \cdot (V_{bi} - V)}{q N_A^{bP}}} \tag{7.2}$$

if it is assumed that $N_A^{bP} \ll N_D^{GaAs}$ and thus the depletion layer only forms inside the BP sheet. In equations 7.1 and 7.2, $N_A^{bP}, N_D^{GaAs}$ and $\varepsilon_{GaAs}, \varepsilon_{bP}$ are the carrier densities and dielectric constants of BP and GaAs, respectively, and $V_{bi}$ is the built in potential. For the estimation we used $N_A^{bP} \approx 1.2 \cdot 10^{23}$ m$^{-3}$, $N_D^{GaAs} \approx 2.7 \cdot 10^{24}$ m$^{-3}$, $\varepsilon_{bP} = 10$, $\varepsilon_{GaAs} = 12$ and $V_{bi}$ = 0.44 eV. It can be seen, that the part of the depletion layer inside GaAs can be neglected. Another reason is screening by the photo-generated carriers which eliminates the bias across the depletion layer.[253]

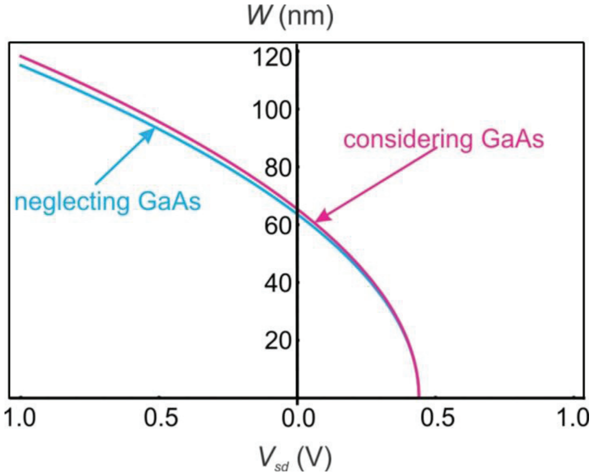

Figure 7.6. Estimation of the depletion layer thickness. The results obtained when GaAs is considered or neglected in the depletion layer calculation are almost identical, revealing that the depletion layer only forms inside the BP sheet.

The photo-response of the device exhibits a clear wavelength dependence, as evident from Fig. 7.7a, which plots the external quantum efficiency $\mathrm{EQE} = \frac{I_{pc}}{P_{light}} \cdot \frac{hc}{e\lambda}$ (where h is the Planck constant, c is the speed of light, e is the elementary charge and λ is the laser wavelength) at zero bias as a function of light power and laser wavelength. The EQE reaches a maximum value of 9.7% for λ = 514 nm, which is of the same order of magnitude as reported for atomically thin TMDC heterostructures.[254–256] For higher laser power the efficiency drops drastically due to the current saturation effect apparent in Fig. 7.5c. The observation of maximum EQE at λ = 514 nm is consistent with the reported behavior of electrostatically define phosphorene pn junctions, and attributable to enhanced optical absorption around this wavelength arising from van Hove singularities in the joint density of states.[257]

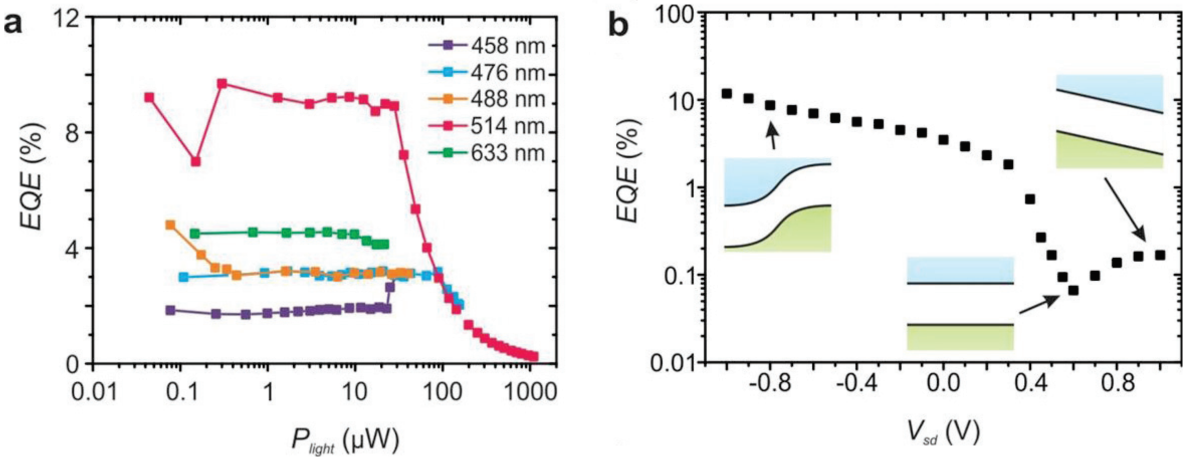

Figure 7.7. Photoresponse under applied bias. a) EQE as a function of laser power for different laser light wavelengths. b) The plot shows the external quantum efficiency (EQE) as a function of bias voltage at λ = 514 nm. The maximum photocurrent was extracted from individual photocurrent maps recorded at different bias voltages. In the inset, the crossover from a pn junction to flat bands to normal resistive behavior is indicated by corresponding band alignments.

Toward evaluating the bias dependence of the EQE, we recorded photocurrent maps at different bias voltages for a constant laser power of 8.6 µW and a laser wavelength of 514 nm. Thus gained EQE values (Fig. 7.7b) monotonously increase with increasing reverse bias, as expected from the enhanced band bending and the size of the depletion layer. As a consequence, at an applied bias voltage of -1 V the EQE doubles compared to zero bias. By comparison, application of an increasing forward bias flattens out the band bending, such that the photocurrent decreases significantly. This trend continues until the flat-band situation is reached at approximately $V_{fb}$ = 0.6 V. Upon further increasing the forward bias, the applied voltage drops over the entire device, whereupon the photocurrent sign changes (see Fig. 7.8) and the EQE increases again. Within the entire set of investigated devices, we observed EQE values of up to 31% at a bias of -2.5 V.

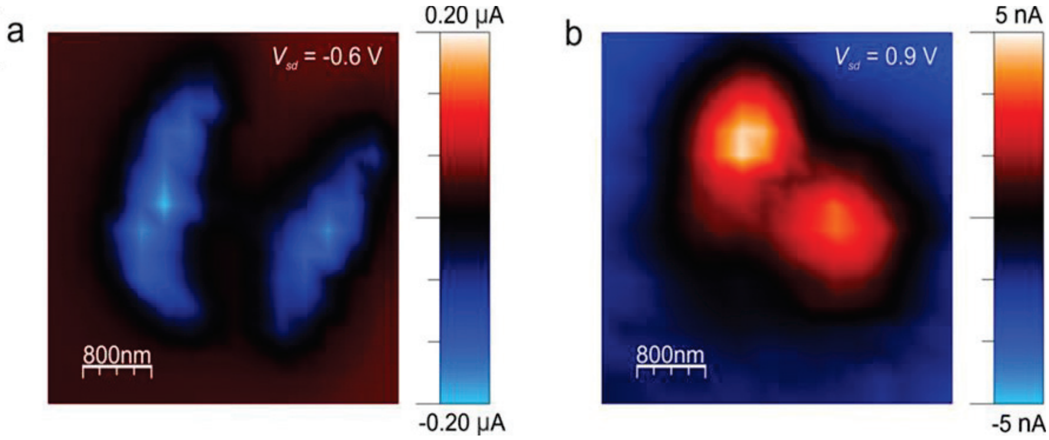

Figure 7.8.Gate dependence of the photocurrent around the flat band condition. The photocurrent of the device changes sign from negative a) to positive b) when the bias is larger than the built-in voltage $V_{bi}$.

We further explored the photoresponse of the BP-GaAs pn heterojunctions in dependence of laser power. Fig. 7.9a compares I-V traces of the above device for a series of different laser powers (λ = 514 nm) recorded with the laser spot at a fixed position (green circle in Fig. 7.5a). Upon increasing the laser power, both the short circuit current $I_{sc}$ as well as the open circuit voltage $V_{oc}$ can be seen to first increase and then to saturate. This behavior reproduces the laser power dependence in Fig. 7.5c. The maximum open circuit voltage of ≈0.6 V corresponds well to the estimated band gap of ≈0.56 eV for the present BP sheet (15 nm, thick). It is noteworthy that the experimental transport band gap of BP with the same thickness is smaller than this estimate.[232] In Fig. 7.9b, the electrical power $P_{el} = V_{sd} \cdot I_{sd}$ is plotted as a function of the applied bias for the corresponding laser powers. In conjunction with the open circuit voltages $V_{oc}$ (see inset of Fig. 7.9c) and the short circuit currents $I_{sc}$, a maximum fill factor $FF = \frac{P_{el}}{V_{oc} \cdot I_{sc}} = 0.3$ is obtained for this device. This value is inferior to the typical range of 0.5 - 0.8 documented for conventional solar cells.[258]

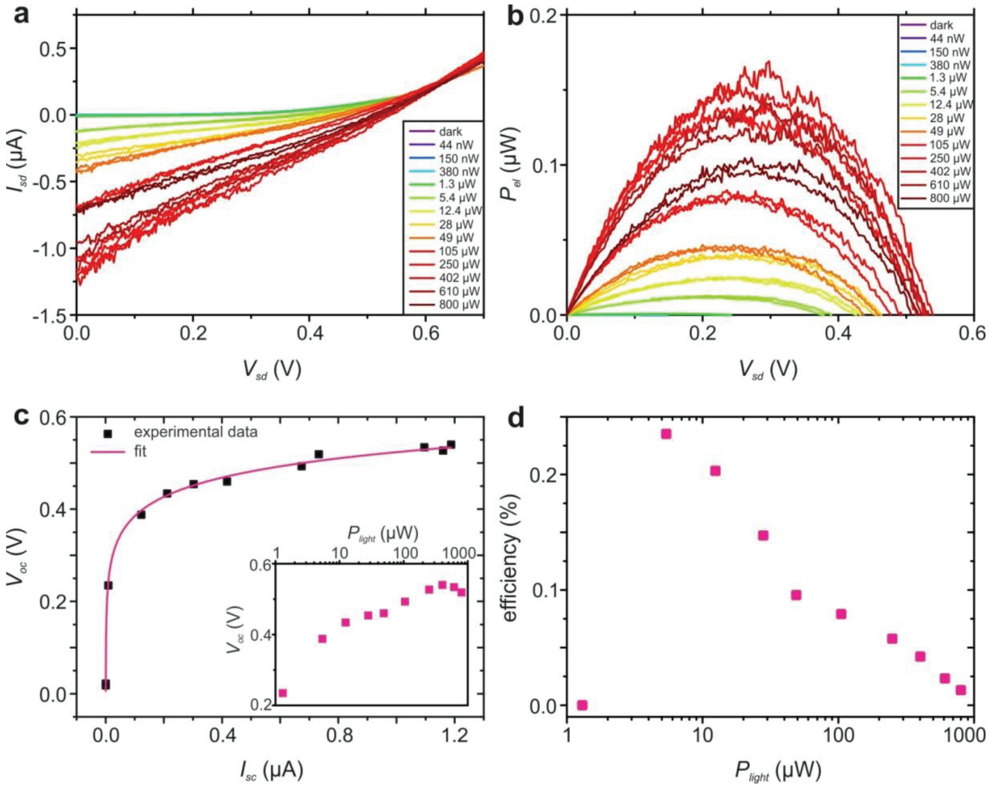

Figure 7.9. Photovoltaic device characteristics. a) I-V curves and b) corresponding electrical power output of the device depicted in Figure 7.2c for different laser powers (λ = 514 nm). The signal was recorded from the green circle in Figure 7.5c. c) Open circuit voltage as a function of short circuit current derived from the plot in panel a). The pink curve is a data fit. Inset: Open circuit voltage in dependence of laser power. d) Photoconversion efficiency of the device as a function of llaser power. The deviation of the data point at lowest laser power is due to the limited resolution in these measurements.

Closer analysis reveals that this difference results from a low shunt resistance $R_{sh}$ combined with a high series resistance $R_s$ in the present devices (see Figure 7.10).[259] The former testifies the presence of an alternative current path for the separated electron-hole pairs, such as charge transport through a Schottky barrier between the metal contact to BP and the underlying GaAs (formed due to possible imperfections in the $SiO_x$). The high series resistance, on the other hand, is a direct consequence of the quite high contact resistance between Ni/Au and BP (see Fig. 7.10). In fact, we observed a two-point resistance in the MΩ range for the BP flakes, whereas much lower values on the order of tens of kΩ have been reported by others.[233] The origin of the non-optimal contacts in our devices remains to be clarified, although the high surface reactivity of BP is most likely involved. The above scenarios are consistent with our fitting model of the dark current, where the extracted ideality factor is significantly higher than the values expected for an ideal pn junction.

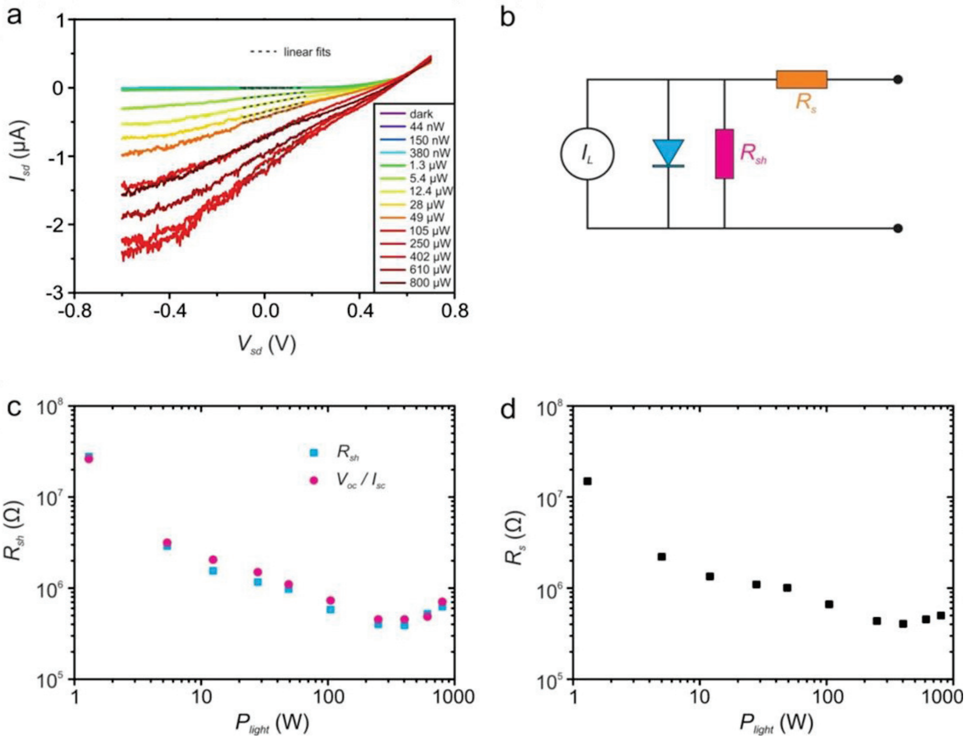

Figure 7.10. Estimation of the shunt and series resistance. a) Full bias range of the I-V curves shown in the main text. The linear parts around V = 0 were used to estimate the shunt resistance $R_{sh}$, the linear parts around I = 0 could be used to estimate the series resistance $R_s$. b) Equivalent circuit for a real solar cell. The current $I_L$ generated inside the cell can flow through the diode (blue) or a parallel shunt $R_{sh}$ resistance (pink). All resistances of the contacts/interfaces are included in a series resistance $R_s$ (orange). c) $R_{sh}$ (extracted from the plot in panel a)) for different light powers. The characteristic resistance $V_{oc}/I_{sc}$ is given as a comparison. Since both values are on the same order of magnitude the fill factor is expected to be low. d) $R_s$ (extracted from the plot in panel a)) for different light powers. The series resistance, which is most likely dominated by the resistance between the BP sheet and the underlying GaAs, and the contacts resistance to the BP flake is on the order of 1 MΩ which further reduces the efficiency of the devices.

In Fig. 7.9c, the open circuit voltage $V_{oc}$ of the above device is shown in dependence of the short circuit current $I_{sc}$. Theoretically, the open circuit voltage $V_{oc}$ should increase with the light-generated current $I_L$ (≈ $I_{sc}$) according to $V_{oc} = \frac{nkT}{q}\ln\left(\frac{I_L}{I_0}+1\right)$. The pink curve in Fig. 7.9c represents a data fit based on this model, which yields an ideality factor of n = 2.3 and a saturation current $I_0$ = 0.17 nA. Both these values coincide very well with those extracted from the I-V curves in the low bias regime (see Fig. 7.3d). Furthermore, based upon the maximum electrical power $P_{el,max}$ for different laser powers $P_{light}$ the photo-conversion efficiency $P_{el,max} / P_{light}$ can be calculated. It features a maximum of 0.24% and decreases notably with increasing laser power (see Fig. 7.9d), comparable to the performance of van der Waals heterojunctions composed of ultrathin layers of BP and molybdenum disulfide ($MoS_2$).[251]

## 7.3 Graphene-black phosphorous pn junctions

The device structure fabricated to combine the fast photoresponse of graphene with the strong optical absorbance of PB is schematically illustrated in Fig. 7.11a. For these devices incorporating a vertical gr-BP junction, a higher responsivity, quantum efficiency and speed were observed at zero gate voltage and under short-circuit conditions, as compared to similar BP-based pn junctions.

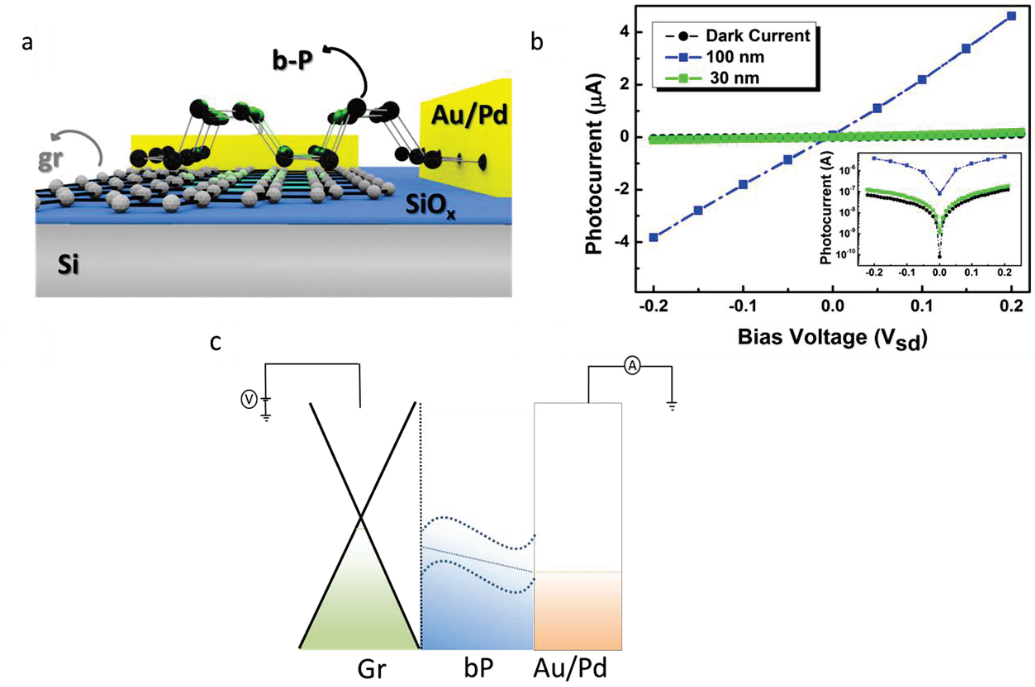

Figure 7.11. Structural design of the gr-BP device comprising a p/p+ junction**.** a) Schematic representation of the vertical gr-BP heterostructure device. b) Room temperature I-V characteristics acquired with and without laser illumination. The inset is a semi-logarithmic plot of current in dependence of bias voltage, for two different devices with a respective BP thickness of 30 and 100 nm. c) Electronic band alignment expected for the gr-BP heterostructure.

Fig. 7.11b shows the I-V characteristics acquired from two different gr-BP heterojunction devices with a BP sheet thickness of 100 nm (denoted as “thick”) and 30 nm (denoted as “thin”). In both cases, comparison is made between illumination by a green laser ($\lambda = 514$ nm) and without illumination (black curve). The semi-logarithmic plot in the inset reveals the generation of a short-circuit current ($I_{sc}$) of 90 nA and 1.4 nA, respective, along with an open circuit potential ($V_{oc}$) of 9 and 5 mV for the devices with thick and thin BP sheets, respectively. The higher photocurrent observed for the thick BP is in accordance with a previously reported trend,[260] can be explained by the increase in optical absorption combined with the decrease in the band gap with increasing number of layers in BP.[232]. Moreover, the sign of the photocurrent points toward the band alignment proposed in Fig. 7.11c, where the graphene is p-doped and the BP is p+-doped. These doping levels are corroborated by the corresponding transfer characteristics (Fig. 7.12), with graphene displaying its neutrality point close to 20 V, whereas that of BP is even above 100 V. Such strong p-doping has previously been reported for thick BP devices and gr-BP heterostructure transistors.[238,261]

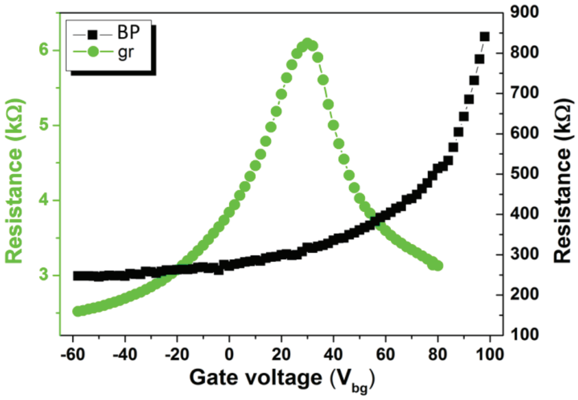

Figure 7.12. Back gate dependence of the resistance of the graphene (green circles) and the BP (black squares) channel. The pronounced shift of the Dirac point to positive gate voltages is indicative of p-type doping of the graphene and p+ doping of the BP.

Further evidence for the doping character of the two components could be gained by Raman spectroscopy. The Raman spectra of graphene before and after the exfoliation of BP on top (Fig. 7.13a) reveal a shift of the G peak from 1593 $cm^{-1}$ (black curve) to 1587 $cm^{-1}$ (green curve), together with an increase of the $I_G/I_{2D}$ ratio from 0.88 to 0.97, with both changes indicating reduced p-doping of graphene.[85] In combination with the transfer curve in Fig. 7.12, it can be concluded that the BP reduces the originally strong p-doping of the graphene by electron transfer, whereupon the BP itself becomes p+-doped. Also the Raman spectra of bare BP, gr-BP and the gr-BP heterostructure after deposition of the top gate contact (Fig. 7.13b) display peak shifts. Yu *et al.*[235] have reported a shift of the $A_{2g}$ mode with chemical doping of BP. For the bare BP, we observe a shift of 1 $cm^{-1}$ compared to the previously reported value of 467.7 $cm^{-1}$.[262] Although of small magnitude, this shift underscores the highly p-doped character of the bare BP. Similar to the graphene case, after the exfoliation of BP the $I_{B2g}/I_{Ag}$ ratio has changed, an observation that we tentatively ascribe to enhanced p-doping of the BP, in accordance with the band diagram in Fig. 7.11c. The $I_{B2g}/I_{Ag}$ ratio return to the value of 0.83 after the deposition of the top gate contact, suggesting a decrease of the p-type doping, in agreement with the shift of the charge neutrality point discuss towards the end of the chapter and with previous reports.[260]

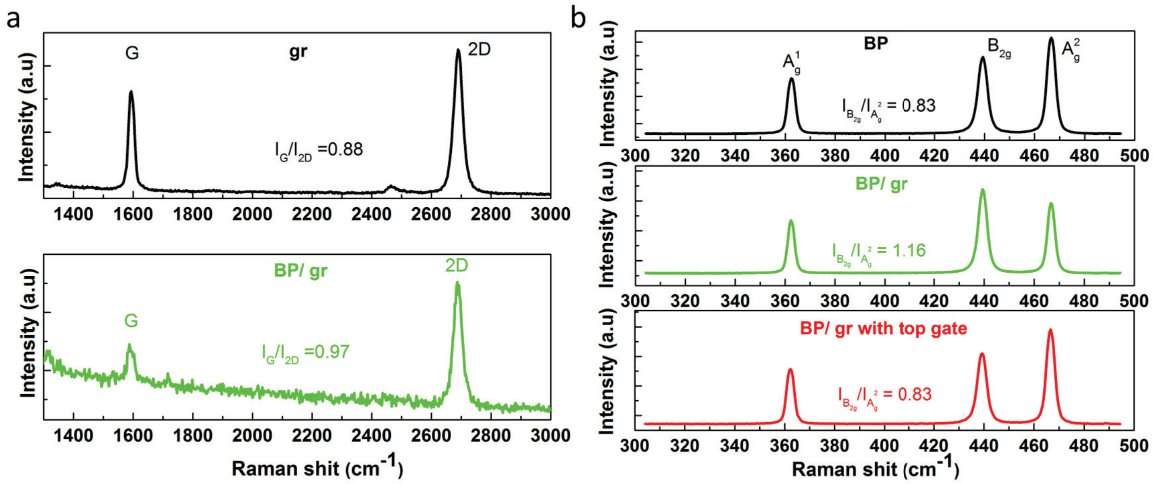

Figure 7.13**.** Raman spectra of the gr-BP device. a) Raman spectra of graphene before (top spectrum) and after the exfoliation of BP on top (bottom spectrum). b) Raman spectra of bare BP, BP-gr and the BP-gr heterostructure after deposition of the top gate contact (from top to bottom).

As already mentioned, one of the main drawbacks of BP-based heterostructures is their only moderately fast photoresponse on the order of ms.[251] To test the response time of the present devices, they were illuminated by light pulses of 1 ms and 1 s (Fig. 7.14a and b). The time traces show that the photocurrent instantaneously reaches its maximum value, and when the light is turned off, it immediately (with the ms time resolution of the set-up) returns to the dark current level. Upon application of repeated pulses (>40), the photoresponse is seen to be well reproducible (Fig. 7.14d). Even for pulses of 1000 s (Fig. 7.14d), the photocurrent decreases by less than 3%, and it instantaneously returns to the dark current level after each pulse, demonstrating a stable and fast response.

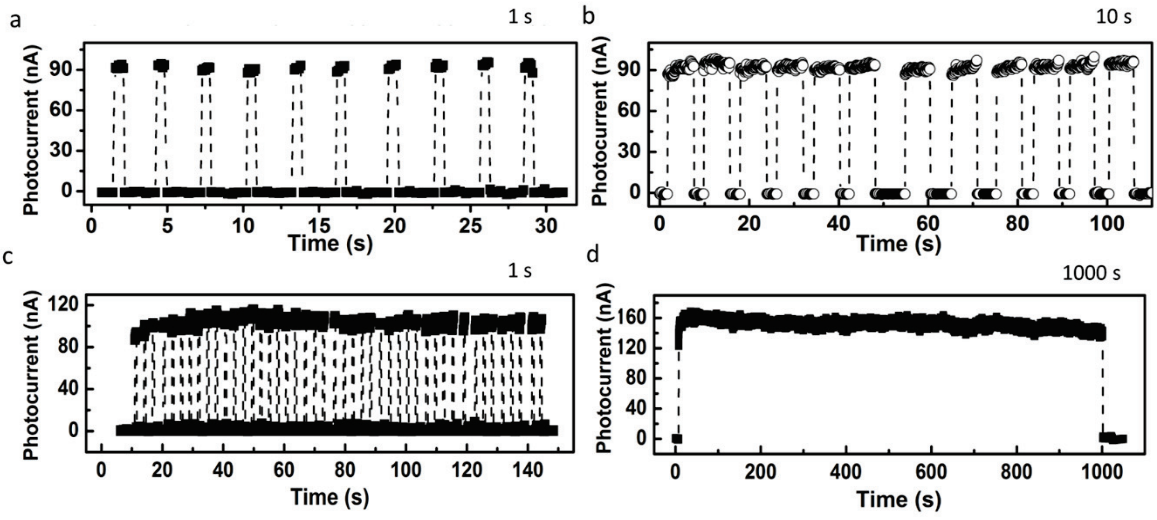

Figure 7.14. Time-dependent photocurrent $I_{sc}$ of BP-gr devices detected upon sample illumination with laser pulses of a) 1 s, b) 10 s, c) 1 s and d) 1000 s duration each ($\lambda$ = 514 nm).

To evaluate the photocurrent behavior of the gr-BP devices in more detail, scanning photocurrent microscopy (SPCM) measurements were performed. Fig. 7.15a and b shows the reflection image and a photocurrent map of the "thick" device (recorded with a laser power of 50 µW), respectively. The positive photocurrent generated at the junction corresponds to an electron (hole) flow towards the gr (BP). This behavior is compatible with the upwards bending of the energy bands of BP when it gets in contact with the graphene (Fig 7.11c). The $I_{sc}$ observed in the SPCM we expected to be predominantly due to photo-thermal effects, according to the study of Low *et al.*[263] which concluded that at low bias and high doping levels (i.e., sizable electron-electron scattering), this mechanism dominates over bolometric and photovoltaic effects.

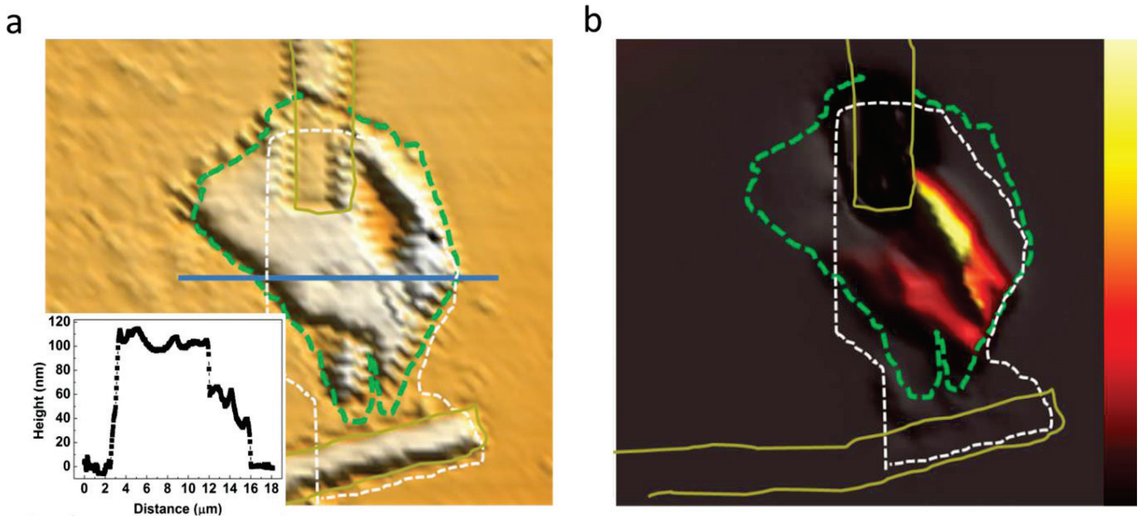

Figure 7.15. Photoresponse of the gr-BP heterostructure device. a) Reflection image and b) photocurrent map of the device, acquired with λ = 514 nm and a laser power of 297 µW. The color bar ranges from -1 to 10 nA. The inset on the left shows the AFM height profile along the blue line in panel a).

It has been reported that close to the charge neutrality point of BP, where the doping level is low, the photocurrent generation mechanism changes from predominantly photo-thermal to photovoltaic, leading to an increase in the quantum efficiency of BP.[260,263] This conclusion is support by the increasing in the photocurrent observe in Fig. 7.16a. That the photocurrent does not reach a maximum is due to the highly p-doped character of the BP which brings the charge neutrality point out the accessible gate voltage range. Furthermore, the photocurrent in dependence of the gate voltage is seen to be higher for positive source-drain bias (Fig. 7.16b). In this measurement, $V_{SD}$ was kept below 0.2 V in order to remain within the photo-thermal or photovoltaic regime, thus avoiding the photo-bolometric mechanism that sets in at higher bias voltages.[260,263] The back gate voltage dependence of the photocurrent (recorded at ±0.2 V source-drain bias) follows the same trend as described above for zero bias, although the photocurrent is one order of magnitude higher.

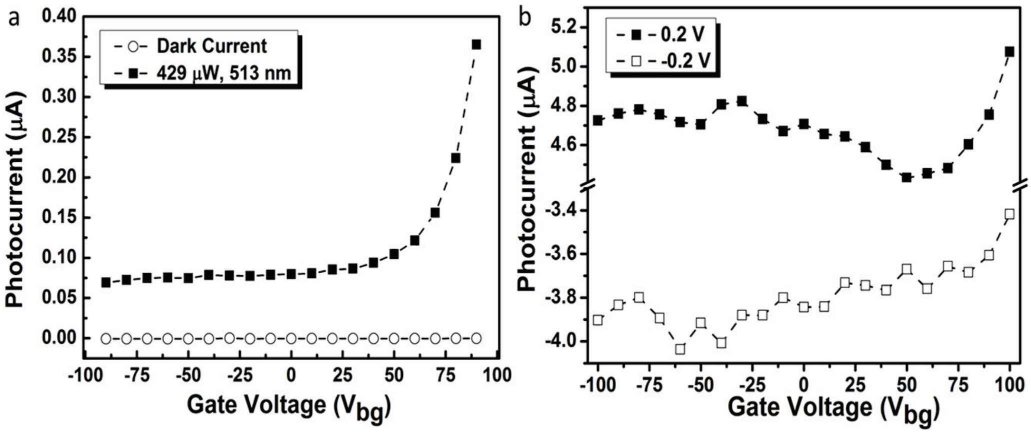

Figure 7.16. Dependence of the photocurrent of a gr-BP device on a) the source-drain bias and b) the back gate voltage.

In further experiments, the IQE and the responsivity of the gr-BP devices was determined as a function of source-drain bias and gate voltage (Fig. 7.17a and b, respectively). The first two quantities were calculated assuming that BP absorbs approximately 30 % of the incoming light. This yields a maximum IQE and responsivity of 13% and 10.7 mAW$^{-1}$, respectively, at a gate voltage of 100 V gate and a source-drain bias of 0.2 V. These values exceed those reported for photodiodes composed of heterostructures of BP and a 2D material,[234,241,242] and are comparable to that of pn junctions based on BP-GaAs[264] and of the most efficient photodetectors based on BP.[236,260,261,265] The photoresponse in dependence of laser wavelength and photon flux (laser power P normalized by the photon energy hv) is plotted in Fig. 7.17c and d. $I_{sc}$ rises with both, increasing photon flux and photon energy. Such dependence on photon flux is well-documented for BP photo-electronic devices.[230] Remarkably, gr-BP junctions like other BP-based devices display a sizable photoresponse close and into the infrared.[230,261] It is apparent from Fig. 7.17d that he IQE as well as the responsivity saturates at higher photon flux. This behavior can be accounted for by the specific recombination kinetics of the photoinduced carriers in BP, combined with their self-interactions and with the trastates.[230,264]

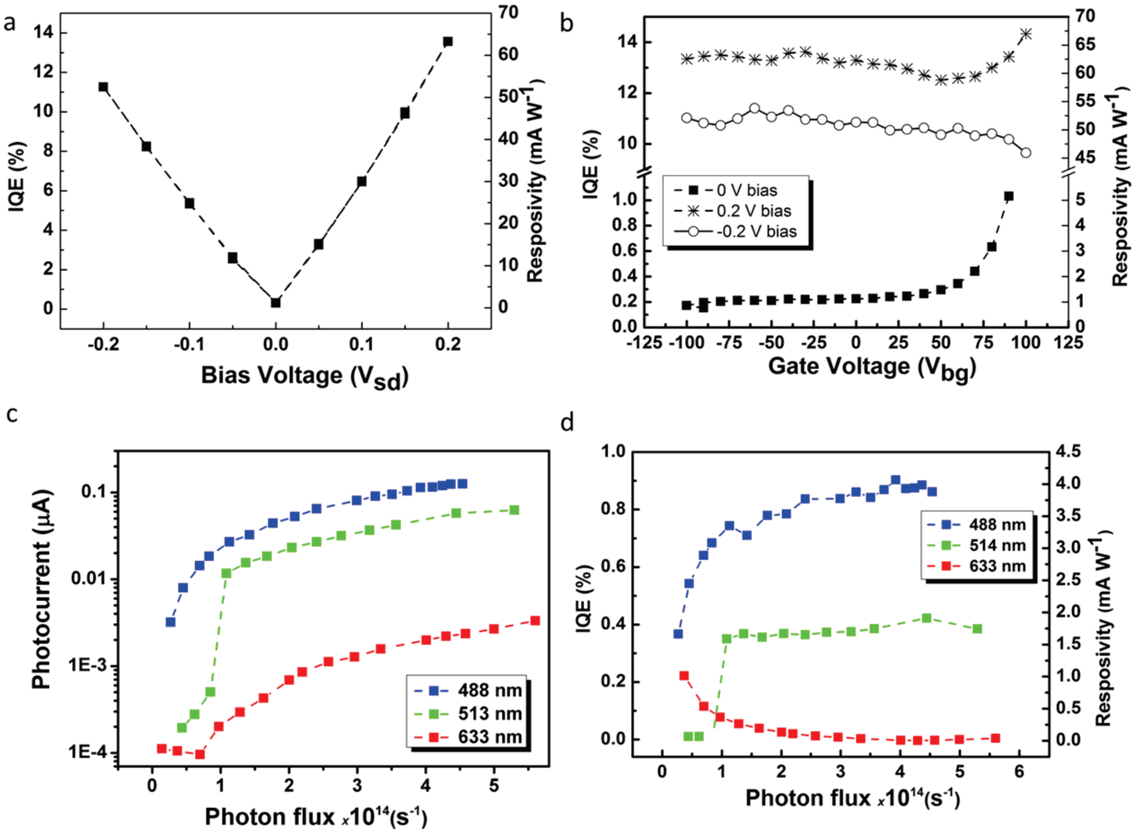

Figure 7.17. Dependence of the gr-BP device performance on the source-drain bias, gate voltage, laser wavelength, and laser power. a) IQE vs. source-drain bias. b) IQE and responsivity vs. back gate voltage for different source-drain voltages. c) Photocurrent vs. photon flux (laser power P/hν) for different laser energies. d) IQE and responsivity vs. photon flux for different laser energies.

In connection with Fig. 7.16a and 7.17b, it was mentioned that it is not possible to reach the charge neutrality point by the back gate action. This limitation is due to the finite screening length of BP[260,266] and the appreciable thickness of the BP sheet (100 nm). Therefore, a top gate electrode was implemented into the “thin” device in order to enhance the gating field. Interestingly, after the top gate deposition a decrease in the p-doping level of the BP was observed, in agreement with the behavior of similar devices[260] and supported by Raman spectroscopy (see Fig. 7.13). The photocurrent dependence on the top gate voltage (Fig. 7.18a) shows a maximum close to the charge neutrality point, reflecting a maximum responsivity of ≈1.1 mA/W and maximum IQE of 1.4% for the thin device. Furthermore, the dual gate behavior of the device (Fig. 7.18b) is similar to that observed for BP top-gated devices.[260] For thin BP-based devices it is possible to control the photocurrent sign by electrostatic gating, whereby the photocurrent generation mechanism changes from photo-thermoelectric via photo-bolometric to photovoltaic.

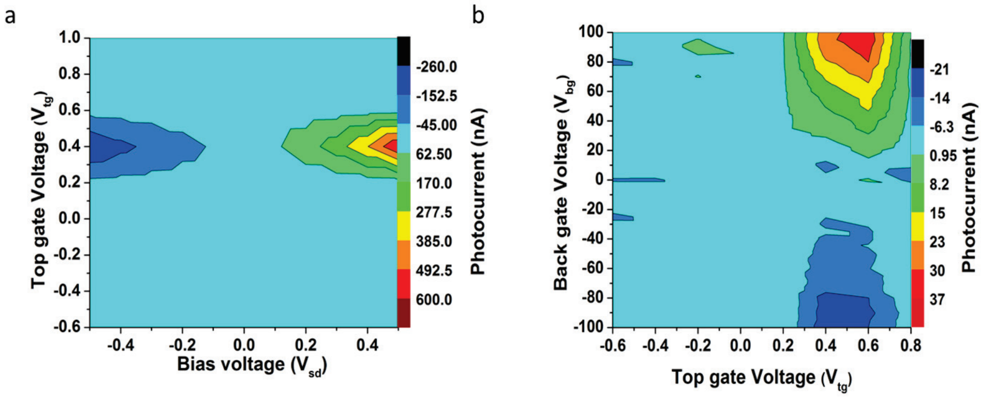

Figure 7.18. Modulation of the photocurrent of a gr-BP heterostructure device by the back and top gate voltage. a) Photocurrent map in dependence of bias voltage and top gate voltage. b) Dual gate photocurrent map.

# Chapter 8 Summary and outlook

In this thesis, the electronic properties of graphene were successfully tuned by its implementation into either lateral or vertical heterostructures. In the first case, chemical functionalization was utilized to create sp$^3$ hybridized patterns within a graphene sheet, whereas in the second case, the graphene was combined with either another 2D material (black phosphorous, BP) or an oxide insulator ($TiO_x$).

Toward the covalent functionalization of graphene, a novel method was explored, specifically the hyperthermal molecular ion collision with 4,4´-azobis(pyridine) (AZP). This one-step, non-destructive method was demonstrated to work very well with CVD graphene on Si-$SiO_2$ substrate. Raman scattering in combination with XPS proved the covalent attachment of azopyridyl-groups to the carbon framework of graphene, with a high functionalization degree of 3%, while AFM imaging showed that the graphene sheets retains its topographic integrity.

The new functionalization protocol based upon hyperthermal ions opens intriguing perspectives, in particular to achieve reactions on graphene that are otherwise not feasible because the large activation barrier cannot be overcome. In future experiments, a wide range of molecules could be used instead of the AZP. One option are metallo-phthalocyanines, which likewise contain pyridine groups.[267] Moreover, the class of heteropoly acids, exemplified by phospho-tungstic-acid (PTA) in Fig. 8.1, could also be covalently appended to graphene, which could open interesting (electro-)catalytic applications.

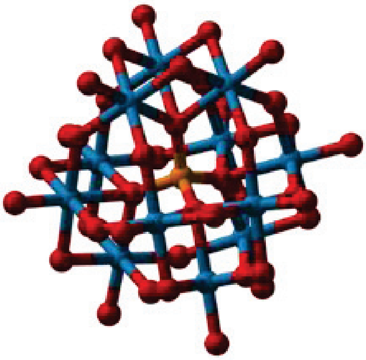

Figure 8.1. Chemical structure of phosphor-tungstic acid (PTA) used in the deposition with ESI on CVD graphene.

Besides using alternative molecules, also the details of the hyperthermal reactions could be further tuned, for example, by adding an electric field to control the landing location of the impinging ions and thereby to attain a patterned functionalization. In this manner, the need for a polymer resist mask (like PMMA) could be avoided.

As a second covalent functionalization approach, the oxidation of graphene by osmium tetroxide vapor was investigated. Raman spectroscopy, AFM and electrical transport measurements revealed a high coverage of oxygenated functional groups on graphene. The method could also be used to pattern functionalized graphene stripes within an extended graphene sheet. Electrical transport measurements across such a stripe featured an on/off ratio as high as 500 at low temperature. At room temperature, the charge transport was found to be dominated by 2D hopping. Further improvement could be made by performing the modifications and the subsequent electrical measurements under vacuum, with the aim of minimizing doping effects due to water molecules in the ambient.[268] This procedure may yield a more defined band gap and hence higher on/off ratios.[163] Furthermore, the reaction to be tested also with CVD graphene, which is available in larger areas than the here studied exfoliated graphene.

The first type of investigated graphene-based heterostructure was a Ti-$TiO_x$-graphene diode. The operation mechanism of these devices was shown to be different from that of conventional MIM diodes, and enables a performance enhancement upon decreasing the oxide thickness, thus overcoming a major weakness of MIM diodes. It involves the bias-induced modulation of the work function of graphene, which in turn alters the transport barrier height. The Gr-$TiO_x$-Ti diodes exhibit a very high asymmetry and nonlinearity of up to 9000 and 8, respectively, while maintaining a large on-current of 0.1 $A/cm^2$ at 1 V, rendering the devices competitive to state-of-the-art MIM diodes. In future experiments, it may be possible to further improve the device performance by optimizing the cleanliness of the graphene as well as the structural quality of the oxide layer. In addition, the Si-$SiO_2$ substrate could be replaced by quartz in order to test the diode behavior at high frequencies. For real technological applications, an up-scaling to wafer size would be needed.

The Ti-$TiO_x$-graphene diodes turned out to be very interesting also as photovoltaic devices. They display a maximum open-circuit voltage of 0.3 V and a short-circuit photocurrent of 14 nA under global illumination. The observation of a sizeable photovoltage constitutes the first-time proof-of-principle of hot carrier extraction from graphene. Although the photo-conversion efficiency of the diodes is still quite low, it might be improvable by minimizing the trap state density in the $TiO_x$ or by work function engineering of the metal, graphene and insulator. However, as the optical absorption of graphene is quite weak, practical device application would require transferring the operation principle to other semimetallic 2D materials, such as $TiSe_2$. Furthermore, it may be worth trying to extend the principle to thin metal films. Preliminary experiments in this direction indicated that Pd and Au (instead of graphene) yield a higher open- circuit potential and short-circuit current. In the case of palladium, the open-circuit potential reaches up to 0.45 V, rendering this configuration of interest not only for photovoltaic also photocatalytic applications.[211]

As another type of vertical heterostructure, heterojunctions comprising graphene as the p-type component and BP as p+-type component were studied. The devices achieved a maximum IQE and responsivity of 13% and 10.7 mA/W, respectively. This efficiency is the highest thus far reported for diodes consisting of a heterostructure of BP and another 2D material. As a promising perspective for future experiments, the nature of these two materials enables chemical and physical doping, whereby the photocurrent signal might be further increased. Further tuning of the photocurrent could be achieved by carefully adjusting the BP thickness.

Complementary to the graphene-BP heterojunction devices, diodes composed of multilayered BP as the p-type component and GaAs as n-type component were investigated. The latter devices exhibited pronounced rectification behavior, which in the low bias regime approaches that of ideal diodes. Moreover, when operated as photodiodes they reached external quantum efficiencies of up 10% under zero bias, and more than 30% under higher reverse bias. Despite these impressive values, the device performance is still limited, as reflected by a quite low fill factor (<0.3), as well as an only moderate electrical power output.

For both types of BP-based diodes, significantly improving the overall device performance will critically depend on devising strategies to control the very sensitive surface chemistry of the BP. As very recently demonstrated for BP-based FETs, the ambient stability of the BP surface can be increased for instance by Te-doping.[269]

# Chapter 9 Appendix

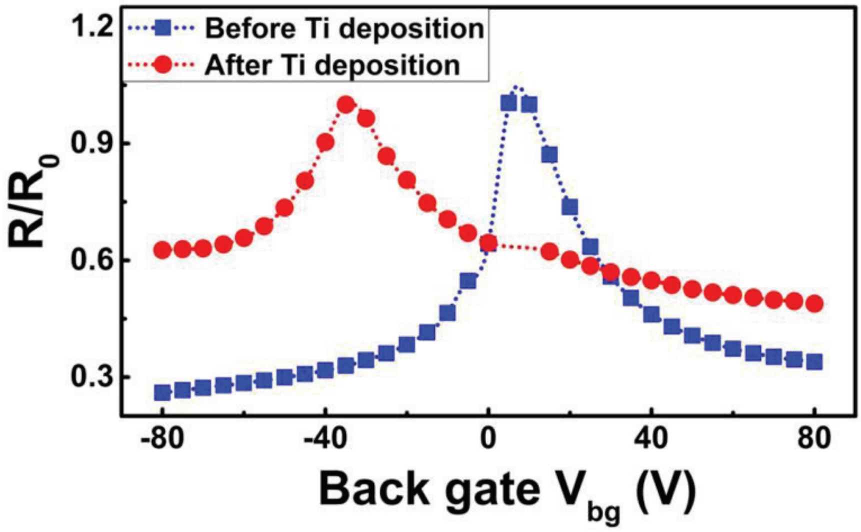

**Appendix A.** Back gate dependence of the normalized resistance of the graphene channel before and after deposition of 25 nm of Ti on top. The pronounced shift of the Dirac point to negative gate voltages is indicative of n-type doping of the graphene by the Ti.

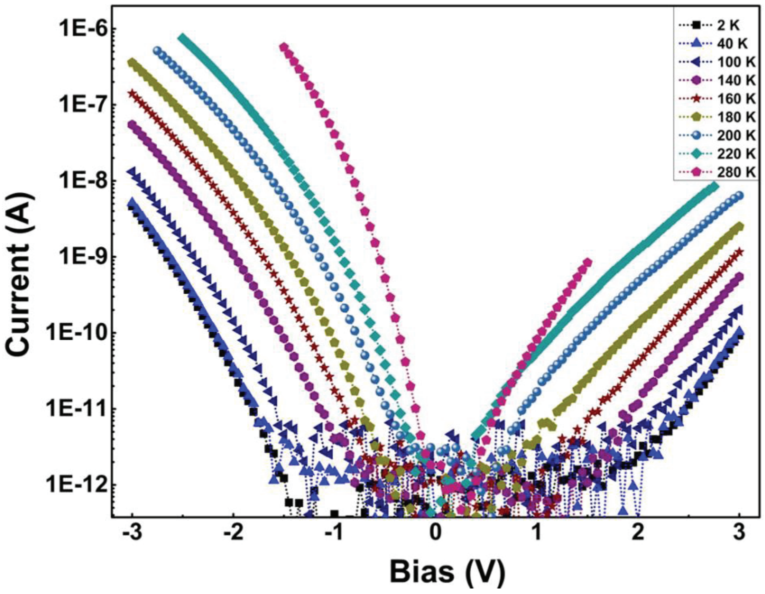

**Appendix B**. Semilogarithmic I-V plots of a Gr-TiO$_x$-Ti diode, measured as a function of temperature. The range of bias that was applied depends on the temperature. Below 60 K, the I-V characteristics are independent of temperature within the range of ±3 V, identifying direct tunneling as the dominant current contribution. Below 100 K, only very small currents are detected for ±1.5 V, indicating that the direct tunneling is negligible in this bias window. Above 100 K, the current displays a strong temperature dependence, which can be explained by thermionic emission and the Poole-Frenkel mechanism as the major transport contributions.

# Chapter 10 Bibliography

1. Kumar, S. Fundamental Limits to Moore's Law. *ArXiv e-prints* (2015).
2. Brown, G. F. & Wu, J. Third generation photovoltaics. *Laser Photon. Rev.* **3,** 394–405 (2009).
3. Huang, X. *et al.* Graphene-Based Materials: Synthesis, Characterization, Properties, and Applications. *Small* **7,** 1876–1902 (2011).
4. Iski, E. V, Yitamben, E. N., Gao, L. & Guisinger, N. P. Graphene at the Atomic-Scale: Synthesis, Characterization, and Modification. *Adv. Funct. Mater.* **23,** 2554–2564 (2013).
5. Georgakilas, V. *et al.* Functionalization of Graphene: Covalent and Non-Covalent Approaches, Derivatives and Applications. *Chem. Rev.* **112,** 6156–6214 (2012).
6. Huh, S., Park, J., Kim, K. S., Hong, B. H. & Kim, S. Bin. Selective n-Type Doping of Graphene by Photo-patterned Gold Nanoparticles. *ACS Nano* **5,** 3639–3644 (2011).
7. Reina, A. *et al.* Large Area, Few-Layer Graphene Films on Arbitrary Substrates by Chemical Vapor Deposition. *Nano Lett.* **9,** 30–35 (2009).
8. Bolotin, K. I. *et al.* Ultrahigh electron mobility in suspended graphene. *Solid State Commun.* **146,** 351–355 (2008).
9. Zhu, Y. *et al.* Graphene and Graphene Oxide: Synthesis, Properties, and Applications. *Adv. Mater.* **22,** 3906–3924 (2010).
10. Blake, P. *et al.* Making graphene visible. *Appl. Phys. Lett.* **91,** (2007).
11. Casiraghi, C. *et al.* Rayleigh Imaging of Graphene and Graphene Layers. *Nano Lett.* **7,** 2711–2717 (2007).
12. Lui, C. H., Mak, K. F., Shan, J. & Heinz, T. F. Ultrafast Photoluminescence from Graphene. *Phys. Rev. Lett.* **105,** 127404 (2010).
13. Bistritzer, R. & MacDonald, A. H. Electronic Cooling in Graphene. *Phys. Rev. Lett.* **102,** 206410 (2009).
14. Song, J. C. W., Rudner, M. S., Marcus, C. M. & Levitov, L. S. Hot Carrier Transport and Photocurrent Response in Graphene. *Nano Lett.* **11,** 4688–4692 (2011).
15. Tielrooij, K. J. *et al.* Photoexcitation cascade and multiple hot-carrier generation in graphene. *Nat Phys* **9,** 248–252 (2013).
16. Auston, D. H. *et al.* *Ultrashort Laser Pulses and Applications*. (Springer Berlin Heidelberg, 2013).
17. Chen, D., Feng, H. & Li, J. Graphene Oxide: Preparation, Functionalization, and Electrochemical Applications. *Chem. Rev.* **112,** 6027–6053 (2012).
18. Notley, S. M. Highly Concentrated Aqueous Suspensions of Graphene through Ultrasonic Exfoliation with Continuous Surfactant Addition. *Langmuir* **28,** 14110–14113 (2012).
19. Nan, H. Y. *et al.* The thermal stability of graphene in air investigated by Raman spectroscopy. *J.*

*Raman Spectrosc.* **44,** 1018–1021 (2013).

20. Ohno, Y., Maehashi, K., Yamashiro, Y. & Matsumoto, K. Electrolyte-Gated Graphene Field-Effect Transistors for Detecting pH and Protein Adsorption. *Nano Lett.* **9,** 3318–3322 (2009).

21. Novoselov, K. S. *et al.* Electric Field Effect in Atomically Thin Carbon Films. *Science.* **306,** 666–669 (2004).

22. Xia, F., Farmer, D. B., Lin, Y. & Avouris, P. Graphene Field-Effect Transistors with High On/Off Current Ratio and Large Transport Band Gap at Room Temperature. *Nano Lett.* **10,** 715–718 (2010).

23. INTERNATIONAL, ROADMAP, T., FOR & SEMICONDUCTORS. 2012 UPDATE OVERVIEW. (2012). Available at: http://www.itrs.net/links/2012itrs/home2012.htm.

24. Geim, A. K. Graphene: Status and Prospects. *Science.* **324,** 1530–1534 (2009).

25. Andrei, E. Y., Li, G. & Du, X. Electronic properties of graphene: a perspective from scanning tunneling microscopy and magnetotransport. *Reports Prog. Phys.* **75,** 56501 (2012).

26. Warner, J. H., Schaffel, F., Rummeli, M. H. & Bachmatiuk, A. *Graphene: Fundamentals and Emergent Applications*. (Elsevier Science & Technology Books, 2013).

27. Xu, M., Liang, T., Shi, M. & Chen, H. Graphene-Like Two-Dimensional Materials. *Chem. Rev.* **113,** 3766–3798 (2013).

28. Wolf, E. L. *Graphene: A New Paradigm in Condensed Matter and Device Physics*. (OUP Oxford, 2013).

29. Tapaszto, L., Dobrik, G., Lambin, P. & Biro, L. P. Tailoring the atomic structure of graphene nanoribbons by scanning tunnelling microscope lithography. *Nat Nano* **3,** 397–401 (2008).

30. Zhou, S. Y. *et al.* Substrate-induced bandgap opening in epitaxial graphene. *Nat Mater* **6,** 770–775 (2007).

31. Geim, A. K. & Grigorieva, I. V. Van der Waals heterostructures. *Nature* **499,** 419–425 (2013).

32. Benia, H. M., Lin, C., Kern, K. & Ast, C. R. Reactive Chemical Doping of the Bi2Se3 Topological Insulator. *Phys. Rev. Lett.* **107,** 177602 (2011).

33. Li, Y., Li, Y.-L., Araujo, C. M., Luo, W. & Ahuja, R. Single-layer MoS2 as an efficient photocatalyst. *Catal. Sci. Technol.* **3,** 2214–2220 (2013).

34. Tang, X. *et al.* Preparation and thermoelectric transport properties of high-performance p-type Bi2Te3 with layered nanostructure. *Appl. Phys. Lett.* **90,** (2007).

35. Sachs, B., Wehling, T. O., Novoselov, K. S., Lichtenstein, A. I. & Katsnelson, M. I. Ferromagnetic two-dimensional crystals: Single layers of K2CuF4. *Phys. Rev. B* **88,** 201402 (2013).

36. Bonaccorso, F., Sun, Z., Hasan, T. & Ferrari, A. C. Graphene photonics and optoelectronics. *Nat Phot.* **4,** 611–622 (2010).

37. Koppens, F. H. L. *et al.* Photodetectors based on graphene, other two-dimensional materials and hybrid systems. *Nat Nano* **9,** 780–793 (2014).

38. Echtermeyer, T. J. *et al.* Photothermoelectric and Photoelectric Contributions to Light Detection in Metal–Graphene–Metal Photodetectors. *Nano Lett.* **14,** 3733–3742 (2014).

39. Gabor, N. M. *et al.* Hot Carrier–Assisted Intrinsic Photoresponse in Graphene. *Science* **334,** 648–652 (2011).

40. H., L. J., Balasubramanian, K., Weitz, R. T., Burghard, M. & Kern, K. Contact and edge effects in graphene devices. *Nat Nano* **3,** 486–490 (2008).

41. J., T. *et al.* Generation of photovoltage in graphene on a femtosecond timescale through efficient carrier heating. *Nat Nano* **10,** 437–443 (2015).

42. Peters, E. C., Lee, E. J. H., Burghard, M. & Kern, K. Gate dependent photocurrents at a graphene p-n junction. *Appl. Phys. Lett.* **97,** (2010).

43. Lemme, M. C. *et al.* Gate-Activated Photoresponse in a Graphene p–n Junction. *Nano Lett.* **11,** 4134–4137 (2011).

44. Xia, F., Mueller, T., Lin, Y., Valdes-Garcia, A. & Avouris, P. Ultrafast graphene photodetector. *Nat Nano* **4,** 839–843 (2009).

45. Xia, F. *et al.* Photocurrent Imaging and Efficient Photon Detection in a Graphene Transistor. *Nano Lett.* **9,** 1039–1044 (2009).

46. Castro Neto, A. H., Guinea, F., Peres, N. M. R., Novoselov, K. S. & Geim, A. K. The electronic properties of graphene. *Rev. Mod. Phys.* **81,** 109–162 (2009).

47. Dutta, S. & Pati, S. K. Novel properties of graphene nanoribbons: a review. *J. Mater. Chem.* **20,** 8207–8223 (2010).

48. Warner, J. H., Schaffel, F., Rummeli, M. & Bachmatiuk, A. *Graphene: Fundamentals and emergent applications*. (Elsevier Science, 2012).

49. Pati, S. K., Enoki, T. & Rao, C. N. R. *Graphene and Its Fascinating Attributes*. (World Scientific, 2011).

50. Wakabayashi, K. Electronic transport properties of nanographite ribbon junctions. *Phys. Rev. B* **64,** 125428 (2001).

51. Geim, A. K. & Novoselov, K. S. The rise of graphene. *Nat Mater* **6,** 183–191 (2007).

52. Wallace, P. R. The Band Theory of Graphite. *Phys. Rev.* **71,** 622–634 (1947).

53. Du, X., Skachko, I., Barker, A. & Andrei, E. Y. Approaching ballistic transport in suspended graphene. *Nat Nano* **3,** 491–495 (2008).

54. Choi, H. *et al.* Broadband electromagnetic response and ultrafast dynamics of few-layer epitaxial graphene. *Appl. Phys. Lett.* **94,** (2009).

55. Xu, W. *et al.* Optoelectronic properties of graphene in the presence of optical phonon scattering. *Phys. Rev. B* **82,** 125304 (2010).

56. Kuzmenko, A. B., van Heumen, E., Carbone, F. & van der Marel, D. Universal Optical Conductance of Graphite. *Phys. Rev. Lett.* **100,** 117401 (2008).

57. Nair, R. R. *et al.* Fine Structure Constant Defines Visual Transparency of Graphene. *Science* **320,** 1308 (2008).

58. Nguyen, B. H. N. and V. H. Advances in graphene-based optoelectronics, plasmonics and photonics. *Adv. Nat. Sci. Nanosci. Nanotechnol.* **7,** 13002 (2016).

59. Kampfrath, T., Perfetti, L., Schapper, F., Frischkorn, C. & Wolf, M. Strongly Coupled Optical Phonons in the Ultrafast Dynamics of the Electronic Energy and Current Relaxation in Graphite. *Phys. Rev. Lett.* **95,** 187403 (2005).

60. Lazzeri, M., Piscanec, S., Mauri, F., Ferrari, A. C. & Robertson, J. Electron Transport and Hot Phonons in Carbon Nanotubes. *Phys. Rev. Lett.* **95,** 236802 (2005).

61. Cotrone, S. *et al.* Phospholipid film in electrolyte-gated organic field-effect transistors. *Org. Electron.* **13,** 638–644 (2012).

62. Terrones, H., Lv, R., Terrones, M. & Dresselhaus, M. S. The role of defects and doping in 2D graphene sheets and 1D nanoribbons. *Reports Prog. Phys.* **75,** 62501 (2012).

63. Murray, J., Shields, Z.-I., Lane, P., Macaveiu, L. & Bulat, F. The average local ionization energy as a tool for identifying reactive sites on defect-containing model graphene systems. *J. Mol. Model.* **19,** 2825–2833 (2013).

64. Zhou, C. *et al.* Graphene's cousin: the present and future of graphane. *Nanoscale Res. Lett.* **9,** 26 (2014).

65. Elias, D. C. *et al.* Control of Graphene's Properties by Reversible Hydrogenation: Evidence for Graphane. *Science* **323,** 610–613 (2009).

66. Jaiswal, M. *et al.* Controlled Hydrogenation of Graphene Sheets and Nanoribbons. *ACS Nano* **5,** 888–896 (2011).

67. Zhou, J. *et al.* Ferromagnetism in Semihydrogenated Graphene Sheet. *Nano Lett.* **9,** 3867–3870 (2009).

68. Nair, R. R. *et al.* Fluorographene: A Two-Dimensional Counterpart of Teflon. *Small* **6,** 2877–2884 (2010).

69. Unger, E. *et al.* Fluorination of carbon nanotubes with xenon difluoride. *Chem. Phys. Lett.* **399,** 280–283 (2004).

70. Jeon, K.-J. *et al.* Fluorographene: A Wide Bandgap Semiconductor with Ultraviolet Luminescence. *ACS Nano* **5,** 1042–1046 (2011).

71. Li, X. *et al.* Highly conducting graphene sheets and Langmuir-Blodgett films. *Nat Nano* **3,** 538–542 (2008).

72. Kim, F., Cote, L. J. & Huang, J. Graphene Oxide: Surface Activity and Two-Dimensional Assembly. *Adv. Mater.* **22,** 1954–1958 (2010).

73. Eda, G. & Chhowalla, M. Chemically Derived Graphene Oxide: Towards Large-Area Thin-Film Electronics and Optoelectronics. *Adv. Mater.* **22,** 2392–2415 (2010).

74. Quintana, M., Vazquez, E. & Prato, M. Organic Functionalization of Graphene in Dispersions. *Acc. Chem. Res.* **46,** 138–148 (2013).

75. Loh, K. P., Bao, Q., Eda, G. & Chhowalla, M. Graphene oxide as a chemically tunable platform for optical applications. *Nat Chem* **2,** 1015–1024 (2010).

76. Stankovich, S. *et al.* Synthesis of graphene-based nanosheets via chemical reduction of exfoliated graphite oxide. *Carbon N. Y.* **45,** 1558–1565 (2007).

77. Dreyer, D. R., Park, S., Bielawski, C. W. & Ruoff, R. S. The chemistry of graphene oxide. *Chem. Soc. Rev.* **39,** 228–240 (2010).

78. Liu, H. *et al.* Photochemical Reactivity of Graphene. *J. Am. Chem. Soc.* **131,** 17099–17101 (2009).

79. Sinitskii, A. *et al.* Kinetics of Diazonium Functionalization of Chemically Converted Graphene Nanoribbons. *ACS Nano* **4,** 1949–1954 (2010).

80. Strom, T. A., Dillon, E. P., Hamilton, C. E. & Barron, A. R. Nitrene addition to exfoliated graphene: a one-step route to highly functionalized graphene. *Chem. Commun.* **46,** 4097–4099 (2010).

81. Rao, C. N. R. & Sood, A. K. *Graphene: Synthesis, Properties, and Phenomena*. (Wiley, 2013).

82. Ferrari, A. C. & Basko, D. M. Raman spectroscopy as a versatile tool for studying the properties of graphene. *Nat Nano* **8,** 235–246 (2013).

83. Malard, L. M., Pimenta, M. A., Dresselhaus, G. & Dresselhaus, M. S. Raman spectroscopy in graphene. *Phys. Rep.* **473,** 51–87 (2009).

84. Eckmann, A., Felten, A., Verzhbitskiy, I., Davey, R. & Casiraghi, C. Raman study on defective graphene: Effect of the excitation energy, type, and amount of defects. *Phys. Rev. B* **88,** 35426 (2013).

85. DasA. *et al.* Monitoring dopants by Raman scattering in an electrochemically top-gated graphene transistor. *Nat Nano* **3,** 210–215 (2008).

86. Papadopoulos, C. *Solid-State Electronic Devices: An Introduction*. (Springer New York, 2013).

87. Di Bartolomeo, A. Graphene Schottky diodes: An experimental review of the rectifying graphene/semiconductor heterojunction. *Phys. Rep.* (2016) doi:http://dx.doi.org/10.1016/j.physrep.2015.10.003

88. Sah, C. T. *Fundamentals of Solid-state Electronics*. (World Scientific, 1991).

89. Tung, R. T. The physics and chemistry of the Schottky barrier height. *Appl. Phys. Rev.* **1,** (2014).

90. Tung, R. T. Recent advances in Schottky barrier concepts. *Mater. Sci. Eng. R Reports* **35,** 1–138 (2001).

91. Raza, H. *Graphene Nanoelectronics: Metrology, Synthesis, Properties and Applications*. (Springer Berlin Heidelberg, 2012).

92. Arora, N. *Mosfet Modeling for VLSI Simulation: Theory and Practice*. (Springer-Verlag, 1993).

93. Sze, S. M. & Ng, K. K. *Physics of Semiconductor Devices*. **1,** (John Wiley & Sons, Inc., 2006).

94. Williams, J. R., DiCarlo, L. & Marcus, C. M. Quantum Hall Effect in a Gate-Controlled p-n Junction of Graphene. *Science.* **317,** 638–641 (2007).

95. Özyilmaz, B. *et al.* Electronic Transport and Quantum Hall Effect in Bipolar Graphene p-n-p Junctions. *Phys. Rev. Lett.* **99,** 166804 (2007).

96. Cheng, H.-C., Shiue, R.-J., Tsai, C.-C., Wang, W.-H. & Chen, Y.-T. High-Quality Graphene p–n Junctions via Resist-free Fabrication and Solution-Based Noncovalent Functionalization. *ACS Nano* **5,** 2051–2059 (2011).

97. Liu, G., Velasco, J., Bao, W. & Lau, C. N. Fabrication of graphene p-n-p junctions with contactless top gates. *Appl. Phys. Lett.* **92,** (2008).

98. Jahani, M. R. S. and D. Electronic transmission through p–n and n–p–n junctions of graphene. *J. Phys. Condens. Matter* **22,** 245503 (2010).

99. Young, A. F. & Kim, P. Quantum interference and Klein tunnelling in graphene heterojunctions. *Nat Phys* **5,** 222–226 (2009).

100. Rickhaus, P. *et al.* Snake trajectories in ultraclean graphene p–n junctions. *Nat Commun* **6,** (2015).

101. Kim, H.-Y., Lee, K., McEvoy, N., Yim, C. & Duesberg, G. S. Chemically Modulated Graphene Diodes. *Nano Lett.* **13,** 2182–2188 (2013).

102. Chen, C.-C., Aykol, M., Chang, C.-C., Levi, A. F. J. & Cronin, S. B. Graphene-Silicon Schottky Diodes. *Nano Lett.* **11,** 1863–1867 (2011).

103. Novoselov, K. S. *et al.* Two-dimensional gas of massless Dirac fermions in graphene. *Nature* **438,** 197–200 (2005).

104. Heersche, H. B., Jarillo-Herrero, P., Oostinga, J. B., Vandersypen, L. M. K. & Morpurgo, A. F. Bipolar supercurrent in graphene. *Nature* **446,** 56–59 (2007).

105. Lu, C.-C., Lin, Y.-C., Yeh, C.-H., Huang, J.-C. & Chiu, P.-W. High Mobility Flexible Graphene Field-Effect Transistors with Self-Healing Gate Dielectrics. *ACS Nano* **6,** 4469–4474 (2012).

106. Lin, Y.-M. *et al.* 100-GHz Transistors from Wafer-Scale Epitaxial Graphene. *Science* **327,** 662 (2010).

107. Liao, L. *et al.* High-speed graphene transistors with a self-aligned nanowire gate. *Nature* **467,** 305–308 (2010).

108. Sharma, B. K. & Ahn, J.-H. Graphene based field effect transistors: Efforts made towards flexible electronics. *Solid. State. Electron.* **89,** 177–188 (2013).

109. Liao, L. *et al.* Scalable Fabrication of Self-Aligned Graphene Transistors and Circuits on Glass. *Nano Lett.* **12,** 2653–2657 (2012).

110. Sire, C. *et al.* Flexible Gigahertz Transistors Derived from Solution-Based Single-Layer Graphene. *Nano Lett.* **12,** 1184–1188 (2012).

111. Ponomarenko, L. A. *et al.* Chaotic Dirac Billiard in Graphene Quantum Dots. *Science* **320,** 356–358 (2008).

112. Tung, V. C. *et al.* Low-Temperature Solution Processing of Graphene−Carbon Nanotube Hybrid Materials for High-Performance Transparent Conductors. *Nano Lett.* **9,** 1949–1955 (2009).

113. Kim, K. S. *et al.* Large-scale pattern growth of graphene films for stretchable transparent electrodes. *Nature* **457,** 706–710 (2009).

114. Bae, S. *et al.* Roll-to-roll production of 30-inch graphene films for transparent electrodes. *Nat Nano* **5,** 574–578 (2010).

115. Wang, X. *et al.* Transparent Carbon Films as Electrodes in Organic Solar Cells. *Angew. Chemie Int. Ed.* **47,** 2990–2992 (2008).

116. Blake, P. *et al.* Graphene-Based Liquid Crystal Device. *Nano Lett.* **8,** 1704–1708 (2008).

117. Degiorgio, V. & Cristiani, I. *Photonics: A Short Course*. (Springer International Publishing, 2015).

118. Dawlaty, J. M. *et al.* Measurement of the optical absorption spectra of epitaxial graphene from terahertz to visible. *Appl. Phys. Lett.* **93,** (2008).

119. Mueller, T., Xia, F. & Avouris, P. Graphene photodetectors for high-speed optical communications. *Nat Phot.* **4,** 297–301 (2010).

120. Liu, C.-H., Chang, Y.-C., Norris, T. B. & Zhong, Z. Graphene photodetectors with ultra-broadband and high responsivity at room temperature. *Nat Nano* **9,** 273–278 (2014).

121. Konstantatos, G. *et al.* Hybrid graphene-quantum dot phototransistors with ultrahigh gain. *Nat Nano*

**7,** 363–368 (2012).

122. Amirmazlaghani, M., Raissi, F., Habibpour, O., Vukusic, J. & Stake, J. Graphene-Si Schottky IR Detector. *IEEE Journal of Quantum Electronics* **49,** 589–594 (2013).

123. Li, X. *et al.* Large-Area Synthesis of High-Quality and Uniform Graphene Films on Copper Foils. *Science* **324,** 1312–1314 (2009).

124. Mafra, D. L., Ming, T. & Kong, J. Facile graphene transfer directly to target substrates with a reusable metal catalyst. *Nanoscale* **7,** 14807–14812 (2015).

125. Bennig, G. K. Atomic force microscope and method for imaging surfaces with atomic resolution. (Patent US4724318, 1988).

126. van Apeldoorn, A. A. *et al.* Parallel high-resolution confocal Raman SEM analysis of inorganic and organic bone matrix constituents. *J. R. Soc. Interface* **2,** 39–45 (2005).

127. Gardiner, D. J. *et al. Practical Raman Spectroscopy*. (Springer Berlin Heidelberg, 2012).

128. Minsky, M. Memoir on inventing the confocal scanning microscope. *Scanning* **10,** 128–138 (1988).

129. Horcas, I. *et al.* WSXM: A software for scanning probe microscopy and a tool for nanotechnology. *Rev. Sci. Instrum.* **78,** (2007).

130. Ho, C. S. *et al.* Electrospray Ionisation Mass Spectrometry: Principles and Clinical Applications. *Clin. Biochem. Rev.* **24,** 3–12 (2003).

131. Loo, J. A. Electrospray ionization mass spectrometry: a technology for studying noncovalent macromolecular complexes. *Int. J. Mass Spectrom.* **200,** 175–186 (2000).

132. Abb, S., Harnau, L., Gutzler, R., Rauschenbach, S. & Kern, K. Two-dimensional honeycomb network through sequence-controlled self-assembly of oligopeptides. *Nat Commun* **7,** (2016).

133. Dubey, G. *et al.* Chemical Modification of Graphene via Hyperthermal Molecular Reaction. *J. Am. Chem. Soc.* **136,** 13482–13485 (2014).

134. Rauschenbach, S. *et al.* Electrospray Ion Beam Deposition of Clusters and Biomolecules. *Small* **2,** 540–547 (2006).

135. Rauschenbach, S. *et al.* Electrospray Ion Beam Deposition: Soft-Landing and Fragmentation of Functional Molecules at Solid Surfaces. *ACS Nano* **3,** 2901–2910 (2009).

136. Malard, L. M., Pimenta, M. A., Dresselhaus, G. & Dresselhaus, M. S. Raman spectroscopy in graphene. *Phys. Rep.* **473,** 51–87 (2009).

137. Koehler, F. M., Jacobsen, A., Ihn, T., Ensslin, K. & Stark, W. J. Chemical modification of graphene characterized by Raman and transport experiments. *Nanoscale* **4,** 3781–3785 (2012).

138. Casiraghi, C. Raman intensity of graphene. *Phys. status solidi* **248,** 2593–2597 (2011).

139. Cheng, H.-P. & Landman, U. Controlled Deposition, Soft Landing, and Glass Formation in Nanocluster-Surface Collisions. **260,** 1304–1307 (1993).

140. Bromann, K. *et al.* Controlled Deposition of Size-Selected Silver Nanoclusters. *Science* **274,** 956–958 (1996).

141. Ugeda, M. M., Brihuega, I., Guinea, F. & Gómez-Rodríguez, J. M. Missing Atom as a Source of Carbon Magnetism. *Phys. Rev. Lett.* **104,** 96804 (2010).

142. Luo, Z. *et al.* Electronic Structures and Structural Evolution of Hydrogenated Graphene Probed by Raman Spectroscopy. *J. Phys. Chem. C* **115,** 1422–1427 (2011).

143. Daniels, K. M. *et al.* Evidences of electrochemical graphene functionalization and substrate dependence by Raman and scanning tunneling spectroscopies. *J. Appl. Phys.* **111,** (2012).

144. Alvarez, J., Futrell, J. H. & Laskin, J. Soft-Landing of Peptides onto Self-Assembled Monolayer Surfaces. *J. Phys. Chem. A* **110,** 1678–1687 (2006).

145. Dongré, A. R., Somogyi, Á. & Wysocki, V. H. Surface-induced Dissociation: An Effective Tool to Probe Structure, Energetics and Fragmentation Mechanisms of Protonated Peptides. *J. Mass Spectrom.* **31,** 339–350 (1996).

146. Niyogi, S. *et al.* Covalent Chemistry for Graphene Electronics. *J. Phys. Chem. Lett.* **2,** 2487–2498 (2011).

147. Yang, D.-Q. & Sacher, E. Carbon 1s X-ray Photoemission Line Shape Analysis of Highly Oriented Pyrolytic Graphite: The Influence of Structural Damage on Peak Asymmetry. *Langmuir* **22,** 860–862 (2006).

148. Jansen, R. J. J. & van Bekkum, H. XPS of nitrogen-containing functional groups on activated carbon. *Carbon N. Y.* **33,** 1021–1027 (1995).

149. Camalli, M., Caruso, F., Mattogno, G. & Rivarola, E. Adducts of tin(IV) and organotin(IV) derivatives with 2,2′-azopyridine II. Crystal and molecular structure of SnMe2Br2AZP and further mössbauer and photoelectronic spectroscopic studies. *Inorganica Chim. Acta* **170,** 225–231 (1990).

150. Levesque, P. L. *et al.* Probing Charge Transfer at Surfaces Using Graphene Transistors. *Nano Lett.* **11,** 132–137 (2011).

151. Ryu, S. *et al.* Atmospheric Oxygen Binding and Hole Doping in Deformed Graphene on a SiO2 Substrate. *Nano Lett.* **10,** 4944–4951 (2010).

152. Moser, J. *et al.* Magnetotransport in disordered graphene exposed to ozone: From weak to strong localization. *Phys. Rev. B* **81,** 205445 (2010).

153. Fiori, G., Betti, A., Bruzzone, S. & Iannaccone, G. Lateral Graphene–hBCN Heterostructures as a Platform for Fully Two-Dimensional Transistors. *ACS Nano* **6,** 2642–2648 (2012).

154. Wysocki, V. H. & Kenttamaa, H. I. Collisional activation of distonic radical cations and their conventional isomers in quadrupole tandem mass spectrometry. *J. Am. Chem. Soc.* **112,** 5110–5116 (1990).

155. Laskin, J., Denisov, E. & Futrell, J. Comparative Study of Collision-Induced and Surface-Induced Dissociation. 2. Fragmentation of Small Alanine-Containing Peptides in FT-ICR MS. *J. Phys. Chem. B* **105,** 1895–1900 (2001).

156. McMurry, J. *Organic Chemistry*. (Brooks/Cole Cengage Learning, 2011).

157. Schroeder, M. Osmium tetraoxide cis hydroxylation of unsaturated substrates. *Chem. Rev.* **80,** 187–213 (1980).

158. Kolb, H. C., VanNieuwenhze, M. S. & Sharpless, K. B. Catalytic Asymmetric Dihydroxylation. *Chem. Rev.* **94,** 2483–2547 (1994).

159. Jacobsen, E. N., Marko, I., Mungall, W. S., Schroeder, G. & Sharpless, K. B. Asymmetric dihydroxylation via ligand-accelerated catalysis. *J. Am. Chem. Soc.* **110,** 1968–1970 (1988).

160. Cui, Burghard, M. & Kern, K. Reversible Sidewall Osmylation of Individual Carbon Nanotubes. *Nano Lett.* **3,** 613–615 (2003).

161. Robinson, J. T. *et al.* Properties of Fluorinated Graphene Films. *Nano Lett.* **10,** 3001–3005 (2010).

162. Li, W. *et al.* Ultraviolet/ozone treatment to reduce metal-graphene contact resistance. *Appl. Phys. Lett.* **102,** (2013).

163. Withers, F., Dubois, M. & Savchenko, A. K. Electron properties of fluorinated single-layer graphene transistors. *Phys. Rev. B* **82,** 73403 (2010).

164. Gómez-Navarro, C. *et al.* Electronic Transport Properties of Individual Chemically Reduced Graphene Oxide Sheets. *Nano Lett.* **7,** 3499–3503 (2007).

165. Liao, Z.-M., Han, B.-H., Zhou, Y.-B. & Yu, D.-P. Hysteresis reversion in graphene field-effect transistors. *J. Chem. Phys.* **133,** (2010).

166. Simmons, J. G. Theory of metallic contacts on high resistivity solids—I. Shallow traps. *J. Phys. Chem. Solids* **32,** 1987–1999 (1971).

167. Aydinoglu, F. *Austin Jorunal of Nanomedicine and Nanotech*. **1**, 1 (2014).

168. Grover, S. & Moddel, G. *Rectenna Solar Cells*. (Springer New York, 2013).

169. Donchev, E. The rectenna device: from theory to practice (a review). *MRS Energy Sustain.* **1,** 1–34 (2014).

170. Simmons, J. G. Generalized Formula for the Electric Tunnel Effect between Similar Electrodes Separated by a Thin Insulating Film. *J. Appl. Phys.* **34,** 1793 (1963).

171. Simmons, J. G. Potential Barriers and Emission-Limited Current Flow Between Closely Spaced Parallel Metal Electrodes. *J. Appl. Phys.* **35,** 2472 (1964).

172. Periasamy, P. *et al.* Fabrication and Characterization of MIM Diodes Based on Nb/Nb2O5 Via a Rapid Screening Technique. *Adv. Mater.* **23,** 3080–3085 (2011).

173. Periasamy, P. *et al.* Metal–Insulator–Metal Diodes: Role of the Insulator Layer on the Rectification Performance. *Adv. Mater.* **25,** 1301–1308 (2013).

174. Chin, M. L. *et al.* Planar metal–insulator–metal diodes based on the Nb/Nb[sub 2]O[sub 5]/X material system. *J. Vac. Sci. Technol. B Microelectron. Nanom. Struct.* **31,** 51204 (2013).

175. Nico, C., Monteiro, T. & Graça, M. P. F. Niobium Oxides and Niobates physical properties: review and prospects. *Prog. Mater. Sci.* **80,** 1–37 (2016).

176. Alimardani, N., McGlone, J. M., Wager, J. F. & Conley, J. F. Conduction processes in metal–insulator–metal diodes with Ta2O5 and Nb2O5 insulators deposited by atomic layer deposition. *J. Vac. Sci. Technol. A Vacuum, Surfaces, Film.* **32,** 01A122 (2014).

177. Yang, H. *et al.* Graphene Barristor, a Triode Device with a Gate-Controlled Schottky Barrier. *Science* **336,** 1140–1143 (2012).

178. Britnell, L. *et al.* Field-Effect Tunneling Transistor Based on Vertical Graphene Heterostructures. *Science.* **335,** 947–950 (2012).

179. Yang, H. *et al.* Graphene Barristor, a Triode Device with a Gate-Controlled Schottky Barrier. *Science* **336,** 1140–1143 (2012).

180. Georgiou, T. *et al.* Vertical field-effect transistor based on graphene-WS2 heterostructures for

flexible and transparent electronics. *Nat Nano* **8,** 100–103 (2013).

181. Heo, J. *et al.* Graphene and thin-film semiconductor heterojunction transistors integrated on wafer scale for low-power electronics. *Nano Lett.* **13,** 5967–5971 (2013).

182. Lu, H. & Seabaugh, A. Tunnel Field-Effect Transistors: State-of-the-Art. *IEEE J. Electron Devices Soc.* **2,** 44–49 (2014).

183. Yu, W. J. *et al.* Vertically stacked multi-heterostructures of layered materials for logic transistors and complementary inverters. *Nat. Mater.* **12,** 246–252 (2012).

184. Novoselov, K. S. *et al.* A roadmap for graphene. *Nature* **490,** 192–200 (2012).

185. Schwierz, F. Graphene transistors. *Nat. Nanotechnol.* **5,** 487–96 (2010).

186. Gaskell, J. *et al.* Graphene-hexagonal boron nitride resonant tunneling diodes as high-frequency oscillators. *Appl. Phys. Lett.* **107,** (2015).

187. Gadalla, M. N., Abdel-Rahman, M. & Shamim, A. Design, Optimization and Fabrication of a 28.3 THz Nano-Rectenna for Infrared Detection and Rectification. *Sci. Rep.* **4,** 4270 (2014).

188. Chalabi, H., Schoen, D. & Brongersma, M. L. Hot-electron photodetection with a plasmonic nanostripe antenna. *Nano Lett* **14,** 1374–1380 (2014).

189. Wang, F. & Melosh, N. A. Power-independent wavelength determination by hot carrier collection in metal-insulator-metal devices. *Nat Commun* **4,** 1711 (2013).

190. Thacker, Z. & Pinhero, P. J. Terahertz Spectroscopy of Candidate Oxides in MIM Diodes for Terahertz Detection. *IEEE Trans. Terahertz Sci. Technol.* **6,** 141–419 (2016).

191. Moretti, A., Maccioni, E. & Nannizzi, M. A W–InSb point contact diode for harmonic generation and mixing in the visible. *Rev. Sci. Instrum.* **71,** (2000).

192. Grover, S., Dmitriyeva, O., Estes, M. J. & Moddel, G. Traveling-Wave Metal/Insulator/Metal Diodes for Improved Infrared Bandwidth and Efficiency of Antenna-Coupled Rectifiers. *IEEE Transactions on Nanotechnology* **9,** 716–722 (2010).

193. Liu, Y., Kim, J. & Lee, J. Finite Thickness Metal-Insulator-Metal Structure for Waveguide Based Surface Plasmon Resonance Biosensing. in *Advances in Optical Sciences Congress* ITuE6 (Optical Society of America, 2009). doi:10.1364/IPNRA.2009.ITuE6

194. Wen, J., Wang, W. J., Li, N., Li, Z. F. & Lu, W. Light enhancement by metal-insulator-metal plasmonic focusing cavity. *Opt. Quantum Electron.* **48,** 1–8 (2016).

195. Wang, F. & Melosh, N. A. Plasmonic energy collection through hot carrier extraction. *Nano Lett* **11,** 5426–5430 (2011).

196. Yu, Y.-J. *et al.* Tuning the Graphene Work Function by Electric Field Effect. *Nano Lett.* **9,** 3430–3434 (2009).

197. Yin, X. *et al.* 19.2% Efficient InP Heterojunction Solar Cell with Electron-Selective TiO 2 Contact. *ACS Photonics* **1,** 1245–1250 (2014).

198. Hsu, W. *et al.* Electron-Selective TiO2 Contact for Cu(In,Ga)Se2 Solar Cells. *Sci. Rep.* **5,** 16028 (2015).

199. Sui, Y. & Appenzeller, J. Screening and Interlayer Coupling in Multilayer Graphene Field-Effect Transistors. *Nano Lett.* **9,** 2973–2977 (2009).

200. Corbet, C. M. *et al.* Oxidized Titanium as a Gate Dielectric for Graphene Field Effect Transistors and Its Tunneling Mechanisms. *ACS Nano* **8,** 10480–10485 (2014).

201. Brongersma, M. L., Halas, N. J. & Nordlander, P. Plasmon-induced hot carrier science and technology. *Nat Nano* **10,** 25–34 (2015).

202. Buntin, S. A., Richter, L. J., Cavanagh, R. R. & King, D. S. Optically Driven Surface Reactions: Evidence for the Role of Hot Electrons. *Phys. Rev. Lett.* **61,** 1321–1324 (1988).

203. Peters, D. W. An infrared detector utilizing internal photoemission. *Proceedings of the IEEE* **55,** 704–705 (1967).

204. Doyle, B. S. & Mistry, K. R. The characterization of hot carrier damage in p-channel transistors. *IEEE Transactions on Electron Devices* **40,** 152–156 (1993).

205. Conibeer, G. Third-generation photovoltaics. *Mater. Today* **10,** 42–50 (2007).

206. Shockley, W. & Queisser, H. J. Detailed Balance Limit of Efficiency of p-n Junction Solar Cells. *J. Appl. Phys.* **32,** (1961).

207. TimmermanD., ValentaJ., DohnalovaK., M., de B. D. A. & GregorkiewiczT. Step-like enhancement of luminescence quantum yield of silicon nanocrystals. *Nat Nano* **6,** 710–713 (2011).

208. Schaller, R. D. & Klimov, V. I. High Efficiency Carrier Multiplication in PbSe Nanocrystals: Implications for Solar Energy Conversion. *Phys. Rev. Lett.* **92,** 186601 (2004).

209. Semonin, O. E. *et al.* Peak External Photocurrent Quantum Efficiency Exceeding 100% via MEG in a Quantum Dot Solar Cell. *Science.* **334,** 1530–1533 (2011).

210. Zheng, B. Y. *et al.* Distinguishing between plasmon-induced and photoexcited carriers in a device geometry. *Nat Commun* **6,** (2015).

211. Clavero, C. Plasmon-induced hot-electron generation at nanoparticle/metal-oxide interfaces for photovoltaic and photocatalytic devices. *Nat Phot.* **8,** 95–103 (2014).

212. Würfel, P., Brown, A. S., Humphrey, T. E. & Green, M. A. Particle conservation in the hot-carrier solar cell. *Prog. Photovoltaics Res. Appl.* **13,** 277–285 (2005).

213. Ross, R. T. & Nozik, A. J. Efficiency of hot-carrier solar energy converters. *J. Appl. Phys.* **53,** (1982).

214. Jean, J., Brown, P. R., Jaffe, R. L., Buonassisi, T. & Bulovic, V. Pathways for solar photovoltaics. *Energy Environ. Sci.* **8,** 1200–1219 (2015).

215. Vaziri, S. *et al.* A Graphene-Based Hot Electron Transistor. *Nano Lett.* **13,** 1435–1439 (2013).

216. Vaziri, S. *et al.* Going ballistic: Graphene hot electron transistors. *Solid State Commun.* **224,** 64–75 (2015).

217. Torres, C. M. *et al.* High-Current Gain Two-Dimensional MoS2-Base Hot-Electron Transistors. *Nano Lett.* **15,** 7905–7912 (2015).

218. Wang, Y. Y., Ni, Z. H., Shen, Z. X., Wang, H. M. & Wu, Y. H. Interference enhancement of Raman signal of graphene. *Appl. Phys. Lett.* **92,** (2008).

219. Ho, P.-H. *et al.* Precisely Controlled Ultrastrong Photoinduced Doping at Graphene-Heterostructures Assisted by Trap-State-Mediated Charge Transfer. *Adv. Mater.* **27,** 7809–15 (2015).

220. Chen, H., Liu, G. & Wang, L. Switched photocurrent direction in Au/TiO2 bilayer thin films. *Sci. Rep.* **5,** 10852 (2015).

221. Katz, E. A. *et al.* Temperature dependence for the photovoltaic device parameters of polymer-fullerene solar cells under operating conditions. *J. Appl. Phys.* **90,** 5343 (2001).

222. Breusing, M., Ropers, C. & Elsaesser, T. Ultrafast Carrier Dynamics in Graphite. *Phys. Rev. Lett.* **102,** 86809 (2009).

223. Mubeen, S. *et al.* On the Plasmonic Photovoltaic. *ACS Nano* **8,** 6066–6073 (2014).

224. Zhang, B. Y. *et al.* Broadband high photoresponse from pure monolayer graphene photodetector. *Nat Commun* **4,** 1811 (2013).

225. Katz, E. A. *et al.* Temperature dependence for the photovoltaic device parameters of polymer-fullerene solar cells under operating conditions. *J. Appl. Phys.* **90,** (2001).

226. Urcuyo, R., Duong, D. L., Jeong, H. Y., Burghard, M. & Kern, K. High Performance Graphene–Oxide–Metal Diode through Bias-Induced Barrier Height Modulation. *Adv. Electron. Mater.* online version (2016). doi:10.1002/aelm.201600223

227. Chen, W., Chen, S., Qi, D. C., Gao, X. Y. & Wee, A. T. S. Surface Transfer p-Type Doping of Epitaxial Graphene. *J. Am. Chem. Soc.* **129,** 10418–10422 (2007).

228. Freitag, M., Low, T., Xia, F. & Avouris, P. Photoconductivity of biased graphene. *Nat Phot.* **7,** 53–59 (2013).

229. Gan, X. *et al.* Chip-integrated ultrafast graphene photodetector with high responsivity. *Nat Phot.* **7,** 883–887 (2013).

230. Buscema, M. *et al.* Fast and Broadband Photoresponse of Few-Layer Black Phosphorus Field-Effect Transistors. *Nano Lett.* **14,** 3347–3352 (2014).

231. Li, L. *et al.* Black phosphorus field-effect transistors. *Nat Nano* **9,** 372–377 (2014).

232. Das, S. *et al.* Tunable Transport Gap in Phosphorene. *Nano Lett.* **14,** 5733–5739 (2014).

233. Liu, H. *et al.* Phosphorene: An Unexplored 2D Semiconductor with a High Hole Mobility. *ACS Nano* **8,** 4033–4041 (2014).

234. Buscema, M., Groenendijk, D. J., Steele, G. A., van der Zant, H. S. J. & Castellanos-Gomez, A. Photovoltaic effect in few-layer black phosphorus PN junctions defined by local electrostatic gating. *Nat Commun* **5,** (2014).

235. Yu, X., Zhang, S., Zeng, H. & Wang, Q. J. Lateral black phosphorene P–N junctions formed via chemical doping for high performance near-infrared photodetector. *Nano Energy* **25,** 34–41 (2016).

236. Castellanos-Gomez, A. Black Phosphorus: Narrow Gap, Wide Applications. *J. Phys. Chem. Lett.* **6,** 4280–4291 (2015).

237. Yu, W. J. *et al.* Vertically stacked multi-heterostructures of layered materials for logic transistors and complementary inverters. *Nat Mater* **12,** 246–252 (2013).

238. Kang, J. *et al.* Probing Out-of-Plane Charge Transport in Black Phosphorus with Graphene-Contacted Vertical Field-Effect Transistors. *Nano Lett.* **16,** 2580–2585 (2016).

239. Sotor, J., Sobon, G., Macherzynski, W., Paletko, P. & Abramski, K. M. Black phosphorus saturable absorber for ultrashort pulse generation. *Appl. Phys. Lett.* **107,** (2015).

240. Roy, K. *et al.* Graphene-MoS2 hybrid structures for multifunctional photoresponsive memory devices. *Nat Nano* **8,** 826–830 (2013).

241. Deng, Y. *et al.* Black Phosphorus–Monolayer MoS2 van der Waals Heterojunction p–n Diode. *ACS Nano* **8,** 8292–8299 (2014).

242. Hong, T. *et al.* Anisotropic photocurrent response at black phosphorus-MoS2 p-n heterojunctions. *Nanoscale* **7,** 18537–18541 (2015).

243. Anderson, R. L. Germanium-Gallium Arsenide Heterojunctions. *IBM J. Res. Dev.* **4,** 283–287 (1960).

244. Tran, V., Soklaski, R., Liang, Y. & Yang, L. Layer-controlled band gap and anisotropic excitons in few-layer black phosphorus. *Phys. Rev. B* **89,** 235319 (2014).

245. Cai, Y., Zhang, G. & Zhang, Y.-W. Layer-dependent Band Alignment and Work Function of Few-Layer Phosphorene. *Sci. Rep.* **4,** (2014).

246. Periasamy, P. *et al.* Metal-insulator-metal diodes: role of the insulator layer on the rectification performance. *Adv Mater* **25,** 1301–1308 (2013).

247. Breitenstein, O. Understanding the current-voltage characteristics of industrial crystalline silicon solar cells by considering inhomogeneous current distributions. *Opto-Electronics Rev.* **21,** 259–282 (2013).

248. Andres, C.-G. *et al.* Isolation and characterization of few-layer black phosphorus. *2D Mater.* **1,** 25001 (2014).

249. S. M. Sze, K. K. N. *Physics of Semiconductor Devices*. (Wiley, 2007).

250. Breitenstein, O. *Advances in Photovoltaics: Part 2. Semiconductors and Semimetals* **89,** (Elsevier, 2013).

251. Deng, Y. *et al.* Black Phosphorus-Monolayer MoS2 van der Waals Heterojunction P-N Diode. *ACS Nano* 8292–8299 (2014).

252. Jariwala, D. *et al.* Gate-tunable carbon nanotube-MoS2 heterojunction p-n diode. *Proc. Natl. Acad. Sci. U. S. A.* **110,** 18076–80 (2013).

253. Li, Z. *et al.* High-power high-linearity flip-chip bonded modified uni-traveling carrier photodiode. *Opt. Express* **19,** B385-90 (2011).

254. Lee, C.-H. *et al.* Atomically thin p–n junctions with van der Waals heterointerfaces. *Nat. Nanotechnol.* **9,** 676–681 (2014).

255. Baugher, B. W. H., Churchill, H. O. H., Yang, Y. & Jarillo-Herrero, P. Optoelectronic devices based on electrically tunable p-n diodes in a monolayer dichalcogenide. *Nat. Nanotechnol.* **9,** 262–7 (2014).

256. Pospischil, A., Furchi, M. M. & Mueller, T. Solar-energy conversion and light emission in an atomic monolayer p-n diode. *Nat. Nanotechnol.* **9,** 257–61 (2014).

257. Yuan, H. *et al.* Broadband Linear-Dichroic Photodetector in a Black Phosphorus Vertical p-n Junction. (2014).

258. Qi, B. & Wang, J. Fill factor in organic solar cells. *Phys. Chem. Chem. Phys.* **15,** 8972–8982 (2013).

259. Breitenstein, O., Bauer, J., Altermatt, P. P. & Ramspeck, K. Influence of Defects on Solar Cell Characteristics. *Solid State Phenom.* **156–158,** 1–10 (2009).

260. Youngblood, N., Chen, C., Koester, S. J. & Li, M. Waveguide-integrated black phosphorus photodetector with high responsivity and low dark current. *Nat Phot.* **9,** 247–252 (2015).

261. Engel, M., Steiner, M. & Avouris, P. Black Phosphorus Photodetector for Multispectral, High-Resolution Imaging. *Nano Lett.* **14,** 6414–6417 (2014).

262. Zant, A. C.-G. and L. V. and E. P. and J. O. I. and K. L. N.-A. and S. I. B. and D. J. G. and M. B. and G. A. S. and J. V. A. and H. W. Z. and J. J. P. and H. Isolation and characterization of few-layer black phosphorus. *2D Mater.* **1,** 25001 (2014).

263. Low, T., Engel, M., Steiner, M. & Avouris, P. Origin of photoresponse in black phosphorus phototransistors. *Phys. Rev. B* **90,** 81408 (2014).

264. Gehring, P., Urcuyo, R., Duong, D. L., Burghard, M. & Kern, K. Thin-layer black phosphorus/GaAs heterojunction p-n diodes. *Appl. Phys. Lett.* **106,** (2015).

265. Island, J. O. & Castellanos-Gomez, A. *2D Materials* **95,** 279–303 (2016).

266. Low, T. *et al.* Plasmons and Screening in Monolayer and Multilayer Black Phosphorus. *Phys. Rev. Lett.* **113,** 106802 (2014).

267. Coates, M. & Nyokong, T. Electrode modification using iron metallophthalocyanine through click chemistry and axial ligation with pyridine. *J. Electroanal. Chem.* **687,** 111–116 (2012).

268. Wehling, T. O., Lichtenstein, A. I. & Katsnelson, M. I. First-principles studies of water adsorption on graphene: The role of the substrate. *Appl. Phys. Lett.* **93,** (2008).

269. Yang, B. *et al.* Te-Doped Black Phosphorus Field-Effect Transistors. *Adv. Mater.* (2016). doi:10.1002/adma.201603723

# Curriculum Vitae

## PERSONAL DATA

**Name:** Roberto Urcuyo Solórzano

**Status:** Married

**Nationality:** Costa Rican

**Birth date:** April 19th, 1986

**Email Address:** roberto.urcuyo@ucr.ac.cr - robertourcuyo@gmail.com

## WORK AND RESEARCH EXPERIENCE

**2011-2012 Researcher:**

Nanofem Laboratory in The Research Center of Electrochemistry and Energy (CELEQ) in San Pedro, San José. University of Costa Rica. Website: (www.nanofem.ucr.ac.cr)

**2007-2011 Research Assistant:**

Nanofem Laboratory in The Research Center of Electrochemistry and Energy (CELEQ) at San Pedro, San José. University of Costa Rica. Website: (www.nanofem.ucr.ac.cr) Collaborators: Dr. Mavis Montero, Dr. Leslie Pineda and Dr. Dionisio Gutiérrez. Research in synthesis and functionalization of silicon surfaces.

**2009-January 2010 Research Assistant:**

Internship at INIFTA. The Research Institute of Theoretical and Applied Physical Chemistry at La Plata, Buenos Aires, Argentina. Website: http//nano.quimica.unlp.edu Collaborators: Dr. Roberto Salvarezza, Dr. M. Elena Vela. Research in functionalization of gold surfaces and measurement of their electrochemical properties.

**2007-2009 Research Assistant:**

INTEL /CENAT/UCR (The National Center of High Technology) Costa Rica. Website: http://www.cenat.ac.cr/ Collaborators: Dr. Mavis Montero, Dr. Dionisio Gutiérrez, Dr. Jose Vega Baudrit, Dr. Lía Castro. Research in Electrochemical properties of modified Silicon Surfaces.

**2005-2007 Research Assistant:**

Center for Research on Environmental Pollution (CICA) at san Pedro, San José, University of Costa Rica. Costa Rica. Website: http://cica.ucr.ac.cr/ Collaborators: Msc. Wilson Beita. Sodium, potassium, phosphorus, SST, Fats and Oils Determinations in Water.

## TEACHING EXPERIENCE

**2012 Lecturer for Inorganic Chemistry:**

Chemistry Department University of Costa Rica. Costa Rica.

**2011 Lecturer for General Chemistry:**
Colegio Cientifico Costarricense, San Pedro, San José, Costa Rica.

## EDUCATION

**2003-Secondary school**
Colegio Santa María de Guadalupe.
**2009-Bachelor in Chemistry**
University of Costa Rica, San José, Costa Rica.
**Top Student in Chemistry in 2008**
**2011-Master in Chemical Sciences.**
University of Costa Rica, San José, Costa Rica.
**Ph.D. Student Currently**
EDMX-Materials Science Program. Ecole Polytechnique Fédérale de Lausanne.

## PUBLICATION

Urcuyo, R., Gehring, P., Sailer, P., Burghard, M. & Kern dual gate black phoshphorus/graphene photodetectors with high responsivity in preparation.

Urcuyo, R., Duong, D. L., Sailer, P., Burghard, M. & Kern, K. Hot-carrier extraction from multilayer graphene accepted in *Nano Letters.*

Urcuyo, R., Duong, D. L., Jeong, H. Y., Burghard, M. & Kern, K. High Performance Graphene–Oxide–Metal Diode through Bias-Induced Barrier Height Modulation. *Adv. Electron. Mater.* online version (2016). doi:10.1002/aelm.201600223.

Gehring, P., Urcuyo, R., Duong, D. L., Burghard, M. & Kern, K. Thin-layer black phosphorus/GaAs heterojunction p-n diodes. *Appl. Phys. Lett.* **106,** 233110 (2015).

Dubey, G., Urcuyo, R., Abb, S., Rinke, G., Burghard, M., Kern, K. Chemical Modification of Graphene via Hyperthermal Molecular Reaction. *J. Am. Chem. Soc*. **136**, 13482–13485 (2014).

Saiz-Poseu, J., Martínez-Otero, A., Roussel, T.; Hui, J., Montero, M., Urcuyo, R., MacLachlan, M., Faraudo, J.;Ruiz-Molina, D. Self-assembly of a catechol-based macrocycle at the liquid–solid interface: experiments and molecular dynamics simulations. *Phys. Chem. Chem. Phys.* **14***,* 11937–11943 (2012).

Sánchez, A.; Urcuyo, R.; González-Flores, D.; Montalberth-Smith, R.; León, C.; Pineda, L. W.; Montero, M. Electroactive Copper (II) Bimetallic Self-Assembled Multilayers on Si(100). *Surface Science* **206,** 527–535 (2012).

Urcuyo, R., Cortés, E., Rubert, A., Benitez, G., Montero, M. L., Tognalli, N. G., Fainstein, A., Vela, M. E., Salvarezza, R. C. Aromatic and Aliphatic Thiol SAMs on Au: Anchoring and Delivering Cu Species *J. Phys. Chem. C* **115***,* 24707–24717 (2011).

## SKILLS

Knowledge in Atomic Force Microscopy (AFM), Scanning tunneling microscopy (STM), X/Ray photoelectron Spectroscopy (XPS), Electrochemistry (Cyclic Voltametry and Impedance Spectroscopy). Ultraviolet–visible spectroscopy, ATR-IR, contact angle and different types of lithography. I also possess knowledge in Shlenck synthetic techniques and glove Box handling.

## LANGUAGES

Spanish, English and Intermediate Level in Italian.